

A THEORY FOR ION GYROFREQUENCY
PHENOMENA OBSERVED ON VLF HISS

by

ARTHUR WING YEE CHAN

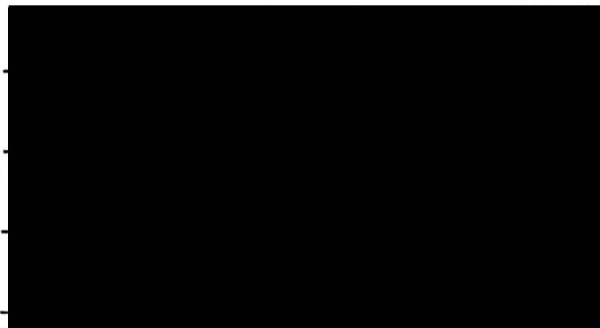
B.Sc., University of Victoria, 1974

A THESIS SUBMITTED IN PARTIAL FULFILLMENT
OF THE REQUIREMENTS FOR THE DEGREE OF
MASTER OF SCIENCE

in the Department
of
Physics

ACCEPTED
FACULTY OF GRADUATE STUDIES
DEAN
DATE July 5/76

We accept this thesis as conforming
to the required standard



© ARTHUR WING YEE CHAN, 1976

UNIVERSITY OF VICTORIA

June, 1976

All rights reserved. This thesis may not be reproduced in whole or in part, by mimeograph or other means, without the permission of the author.

Supervisor: Dr. Robert E. Horita

ABSTRACT

The Landau instability theory proposed by Horita and Watanabe (1969) and Horita (1972) is extended to allow computer calculations of warm plasma effects. An investigation is first made to consider the influence on the growth rate of the ionospheric parameters, especially the wave frequency ω_r around the lower hybrid resonance (LHR) frequency, the temperatures for plasma electrons and ions (T_e^P and T_i^P) and streaming electrons (T_e^S and T_i^S), the strength of the Earth's magnetic field B_0 and the ion concentration N_k .

Then a search was made for absorption bands at harmonics of the proton, helium and oxygen gyrofrequencies. It was found that the absorption bands occur when the parallel to perpendicular temperature ratios for the plasma particles and the streaming particles satisfy $T_e^P/T_i^P < 1$ and $T_e^S/T_i^S < 1$. Using a particular set of ionospheric parameters from the ISIS 2 satellite, absorption band harmonics of the proton and helium gyrofrequencies were found at a particular value of $T_e^P/T_i^P < 1$. Absorption bands near harmonics of the oxygen gyrofrequency were found from another set of ionospheric parameters. Absorption bands exactly at harmonics of the helium and oxygen gyrofrequencies were also found.

The results presented are then compared with satellite observations. It is found that many features are in good agreement. The Landau instability process appears to be a possible generation mechanism for auroral hiss, electrostatic noise seen on the Javelin 8.46 rocket, V-shaped VLF noise, saucers and ELF hiss.



ACKNOWLEDGEMENTS

I would like to thank Dr. R.E. Horita for his patient supervision and guidance throughout this study. I am also indebted to him for many valuable suggestions and comments and for carefully reviewing the final manuscript. I also wish to thank Drs. G.W. Bushnell, H.W. Dosso and R.M. Pearce for their valuable suggestions and comments.

For their encouragement, moral support and patience over the years of this study, I would like to thank my parents, sisters and brother.

I wish to express my gratitude to Mr. L. Friesen for help in developing the computer program which is a modification of an existing program developed by Dr. R.E. Horita and Mr. L. Friesen of this laboratory. I also wish to thank my colleagues for many helpful suggestions and discussions.

I would like to thank Drs. R.E. Barrington and F.H. Palmer of the Communications Research Center, Ottawa, for making available the micro-filmed ISIS 2 VLF spectrograms. I also thank Dr. J.G. Hoffman, University of Texas at Dallas, for the ISIS 2 ion composition data.

For the speedy and accurate typing of this thesis, I thank Mrs. J.R. Hunt.

I am grateful for financial support provided by the University of Victoria (Graduate Scholarship) and the National Research Council of Canada through my supervisor.

TABLE OF CONTENTS

	Page
ABSTRACT	ii
ACKNOWLEDGEMENTS	iv
LIST OF FIGURES	vii
LIST OF TABLES	xi
CHAPTER 1 INTRODUCTION	
1.1 Historical review	1
1.2 Some theories of VLF hiss	8
1.3 Recent satellite observations	12
1.4 Purpose and summary of work covered in this thesis	17
CHAPTER 2 LANDAU INSTABILITY THEORY	
2.1 Plasma parameters and Maxwell's equations	19
2.2 Power absorption by charged particles in collisionless plasma	21
2.3 The mobility tensor	25
2.4 The dispersion relation	
2.4.1 Cold plasma approximation	31
2.4.2 Warm plasma	35
2.5 The dielectric tensor	37
2.6 Wave energy and growth rate	39

	Page
CHAPTER 3 COMPUTER ANALYSIS	
3.1 Detailed computer calculation procedure	42
3.2 Computer results	48
3.2.1 Growth rate for wave frequencies around the LHR frequency	51
3.2.2 Effect of T_{ii}^P/T_{ii}^S and T_{ii}^S/T_{ii}^S on the growth rate	55
3.2.3 Effect of the strength of the Earth's magnetic field B_0 on the growth rate	62
3.2.4 Effect of ion concentration N_k on the growth rate	68
3.3 Absorption bands near harmonics of the proton, helium and oxygen gyrofrequencies	
3.3.1 Absorption bands near proton gyrofrequency harmonics	71
3.3.2 Absorption bands near helium gyrofrequency harmonics	82
3.3.3 Absorption bands near oxygen gyrofrequency harmonics	85
CHAPTER 4 DISCUSSION OF RESULTS	
4.1 Comparison of theory with satellite observations	90
4.2 Discussion of the influence of temperature	92
CHAPTER 5 CONCLUSION	94
APPENDIX A: FLOWCHARTS AND COMPUTER PROGRAM	97
REFERENCES	131

LIST OF FIGURES

Figure	Page
1.1	Examples of LHR noise bands from the Alouette 1 satellite. The first example is polar LHR noise band; the last three examples are midlatitude LHR noise bands (after McEwen and Barrington, 1967) 5
1.2	VLF spectrogram received by the ISIS 2 satellite on December 4, 1971 at 064957 UT. The auroral hiss exhibits fine structure related to the proton gyrofrequency, f_p . The absorption bands coincide well with the proton gyrofrequency harmonics (after Horita <i>et al.</i> , 1976) 14
1.3	VLF spectrogram received by the ISIS 2 satellite on May 6, 1972 at 064315 UT. The auroral hiss exhibits fine structure related to the proton gyrofrequency, f_p . The absorption bands coincide well with the proton gyrofrequency harmonics 15
2.1	Diagram shows physical situation in which the Landau instability is presumed to occur 22
2.2	Relationship between the mean streaming velocity of the streaming particles and the wave vector for the E.M. wave 22
3.1	Growth rate of whistler-mode waves as a function of the propagation angle θ for 3 frequencies: $\omega_f^1 = 1.20, 1.63$ and 2.50 54
3.2	The effect of the ratio T_w^S/T_e^S of the streaming electrons on the growth rate with $T_w^P/T_e^P = 1$ for the plasma particles. The three ratios are $T_w^S/T_e^S = 0.5, 1$ and 5 56
3.3	The effect of the ratio T_w^P/T_e^P of the plasma particles on the growth rate with $T_w^S/T_e^S = 1$ for the streaming electrons. The propagation angles considered are from 0° to 82° . The ratios are $T_w^P/T_e^P = 0.5, 1$ and 5 57
3.4	The effect of the ratio T_w^P/T_e^P of the plasma particles on the growth rate with $T_w^S/T_e^S = 1$ for the streaming electrons. The propagation angles considered are from 76° to 90° . The three ratios are $T_w^P/T_e^P = 0.5, 1$ and 5 58

Figure	Page
3.5 The effect of the strength of the Earth's magnetic field B_0 on the growth rate. The propagation angles considered are from 0° to 85° with (1) $B_0 = 0.16$ gauss, (2) $B_0 = 0.22$ gauss, (3) $B_0 = 0.28$ gauss and (4) $B_0 = 0.33$ gauss	63
3.6 The effect of the strength of the Earth's magnetic field B_0 on the growth rate. The propagation angles considered are from 85° to 90° with (1) $B_0 = 0.16$ gauss, (2) $B_0 = 0.22$ gauss, (3) $B_0 = 0.28$ gauss and (4) $B_0 = 0.33$ gauss	64
3.7 The effect of ion concentration on the growth rate. The three sets of ion concentration used are listed in Table 3.6 with (1) $N = 0.422 \times 10^{14} \text{ cm}^{-3}$, (2) $N = 0.822 \times 10^{14} \text{ cm}^{-3}$ and (3) $N = 1.2624 \times 10^{14} \text{ cm}^{-3}$	69
3.8 Normalized wave frequency versus power absorption per unit volume by charged particles for $\theta = 88.65^\circ$. Absorption bands appear near harmonics of the proton gyrofrequency	75
3.9 Normalized wave frequency versus power absorption per unit volume by charged particles for $\theta = 88.85^\circ$. Absorption bands appear near harmonics of the proton gyrofrequency	76
3.10 Normalized wave frequency versus power absorption per unit volume by charged particles for $\theta = 88.90^\circ$. Absorption bands near harmonics of the helium gyrofrequency have appeared	77
3.11 Normalized wave frequency versus power absorption per unit volume by charged particles for $\theta = 89.00^\circ$. Absorption bands near harmonics of the helium gyrofrequency are observed	78
3.12 Normalized wave frequency versus power absorption per unit volume by charged particles for $\theta = 89.10^\circ$. Absorption bands near harmonics of the helium gyrofrequency are observed	79

Figure	Page
3.13	Normalized wave frequency versus power absorption per unit volume by charged particles for $\theta = 89.15^\circ$. Absorption bands near harmonics of the helium gyrofrequency are observed 80
3.14	Normalized transition frequency ω_T^1 versus the propagation angle θ within the 'electrostatic' region 81
3.15	Normalized wave frequency versus power absorption per unit volume by charged particles. Absorption bands near harmonics of the helium gyrofrequency are shown 84
3.16	Normalized wave frequency versus power absorption per unit volume by charged particles for $\omega_r^1 = 0.97$ to $\omega_r^1 = 1.23$. Absorption bands near harmonics of the oxygen gyrofrequency are shown 87
3.17	Normalized wave frequency versus power absorption per unit volume by charged particles for $\omega_r^1 = 1.24$ to $\omega_r^1 = 1.50$. Absorption bands near harmonics of the oxygen gyrofrequency are shown 88
3.18	Normalized wave frequency versus power absorption per unit volume by charged particles for $\omega_r^1 = 1.51$ to $\omega_r^1 = 1.73$. Absorption bands near harmonics of the oxygen gyrofrequency are shown 89
A.1	Flowchart for the main program which is used to calculate the gyrofrequencies and plasma frequencies for thermal electrons, nonthermal electrons and ions. The main program also serves as the control of the program to print out the required information 98
A.2	Flowchart for the subprogram BLOCK DATA which contains the built-in data for the program 102
A.3	Flowchart for subprogram P which is used to calculate the power absorption by the charged particles and also to calculate the wave energy 103

Figure		Page
A.4	Flowchart for subprogram B which is used to calculate the modified Bessel function of the first kind and its derivative	107
A.5	Flowchart for subprogram KITER which is used to compute the value of the wave vector \underline{k} for a warm plasma	110
A.6	Flowchart for subprogram KINIT which is used to compute the value of the wave vector \underline{k} for a cold plasma	111
A.7	Flowchart for subprogram MATRIX which is used to compute the components of the mobility tensor M and the components of the dielectric tensor KK	113
A.8	Flowchart for subprogram Q which is used to check the real and imaginary parts of the wave frequency	117
A.9	Flowchart for subprogram ANGLE which is used to compute $\langle \underline{H} \rangle_n$, $\langle \underline{\phi} \rangle_n$, $\langle \underline{\psi} \rangle_n$, $\langle V_{z\phi} \rangle_n$ and $\langle V_{z\psi} \rangle_n$. Those quantities are the arguments of the mobility tensor	118
A.10	Flowchart for subprogram U which is used to evaluate the imaginary part of the constant F_0	119
A.11	Flowchart for subprogram F which is used to compute the LHR frequency ($S = 0$)	120

LIST OF TABLES

Table		Page
3.1	Numerical values of ionospheric parameters at an altitude of 1431 km and 82.06° geomagnetic latitude	49
3.2	Numerical values of the cyclotron and plasma frequencies at an altitude of 1431 km and 82.06° geomagnetic latitude	50
3.3	Numerical values of ionospheric parameters at an altitude of 1408 km and 70.47° geomagnetic latitude	60
3.4	LHR frequencies and cyclotron frequencies using values from Table 3.3 and various values of B_0	61
3.5	Numerical values of ionospheric parameters for the graph of ω_i vs θ for the effect of ion concentration	66
3.6	Numerical values of ion concentrations, plasma frequencies and corresponding LHR frequencies for the graph of ω_i vs θ for the effect of ion concentration	67

CHAPTER 1

INTRODUCTION

1.1 Historical review

Whistlers and very-low-frequency (VLF) emissions are the two types of radio signals studied widely by many physicists since 1894. Whistlers are bursts of very-low-frequency electromagnetic (E.M.) energy produced by ordinary lightning discharges. These bursts of E.M. energy travel into the ionosphere and are dispersed as they propagate along the lines of force of the Earth's magnetic field. In general, a whistler starts at a high frequency and then drops in frequency to a lower limit of about 1 kHz after 1 second. The basic requirement for the detection of whistlers is that a voltage be induced in an electrical circuit by the very-low-frequency electromagnetic waves of the whistler. The voltage is then amplified and converted to a form suitable for detection. These whistlers are detected by simple antennae; a typical whistler antenna consists of a single-turn loop of copper wire in the shape of a delta with an elevation of about 30 feet. The loop is connected through a transformer to a high-gain, low-noise, wide-band audio amplifier.

The first known report on whistlers was a paper by Preece (1894). This was followed by papers by Barkhausen (1919), Eckersley (1925, 1926, 1928) and Størmer (1928). In the early stage, investigators

detected these signals from "audio-recorder" systems, and no explanation had been given for the origin of the whistlers. In 1930, Barkhausen proposed two possible explanations of the source of the whistlers. One involved multiple reflections between earth and ionosphere and the other was based on the propagation of waves through a dispersive medium. After the Second World War, new techniques of analysis and new methods of detection of the whistlers were introduced by other investigators (e.g. Helliwell, 1956; Storey, 1957B, etc.). With the development of whistler spectrology and theory, there has arisen new nomenclature that reflects the spectrographic appearance of whistlers and the mechanism of whistler propagation. Characteristics of whistlers and variations in their occurrence are discussed in detail by Helliwell (1965).

Other types of electromagnetic noise similar to whistlers are called very-low-frequency (VLF) emissions which have frequencies ranging from 200 Hz to 30 kHz. Very-low-frequency emissions can also be detected and recorded with the same equipment employed in the study of whistlers. Observations show that some of these emissions are in close association with whistlers. They may appear in continuous form lasting for several minutes, or they may occur in discrete bursts as short as a fraction of a second. Emission spectra are characterized by a tendency for both the steady and the discrete forms to appear in well-defined and sometimes relatively narrow frequency bands. The width of individual bands may range from about 30 Hz to 20 kHz or more.

Classification of VLF emissions are also presented in detail by Helliwell (1965). Though the mechanism of VLF emissions is not yet understood, evidence shows that these emissions propagate to the earth from a region of generation within the earth's magnetosphere.

On September 29, 1962, the Canadian Alouette 1 satellite was launched into a nearly circular orbit (with perigee 996.38 km and apogee 1031.05 km) at a height of 1000 km and with an inclination of 80.463 degrees to the equator. Included in its payload was a broad-band very-low-frequency (VLF) receiver which covered the frequency band from 400 Hz to 10 kHz. The VLF receiver was connected to the 150-ft long electric dipole antenna.

Within the VLF measurements, there was an unusual band of noise characterized by a sharp lower-frequency cutoff which usually increased with decreasing latitude of the satellite (Barrington and Belrose, 1963). Comparison of satellite and ground-based recordings showed that this new type of noise was not observed on the ground (Brice and Smith, 1964). Many characteristics of this noise band led to the conclusion that the lower-frequency cutoff is at the lower hybrid resonance (LHR) frequency of the ambient plasma (Brice and Smith, 1965). Hence this noise band has been termed the LHR noise band. The noise is observed in the frequency range from about 5 to 10 kHz with a bandwidth varying from one to several kHz. LHR noise is frequently observed both in midlatitude and polar regions.

Accordingly these two types of noise have been called midlatitude and polar LHR noise (McEwen and Barrington, 1967). At mid-latitudes, the lower-frequency cutoff varies systematically with latitude while the bands show a wide variation in appearance. A large number of the observed midlatitude LHR noise appears as a continuous emission of unknown origin, but sometimes it also appears as short bursts evidently triggered by whistlers. Such signals are termed whistler-triggered LHR noise. They have a maximum in occurrence at 50° - 60° invariant latitude. The lower-frequency cutoff of the polar LHR noise band is erratic and shows rapid fluctuations; the noise recorded is mostly a continuous emission lasting for several minutes. Polar LHR noise is mainly observed in the region 70° - 85° invariant latitude.

Examples of LHR noise bands from the Alouette 1 satellite are given in Figure 1.1 (after McEwen and Barrington, 1967). The first example shows a noise band with a wide bandwidth and a cutoff frequency at about 5 kHz. This noise band is recorded while the satellite is at an invariant latitude of 80° N, so it is called polar LHR noise. The fluctuations in the lower frequency cutoff are believed to be due to variations in the electron density of the medium. The next three examples show midlatitude LHR noise bands. Example 2 shows that the noise between 8 and 10 kHz has been triggered by both short and long fractional-hop whistlers. Example 3 shows three triggered LHR noise bursts which persist for about five seconds. Example 4 shows a fairly steady noise band with a lower cutoff of about 5 kHz

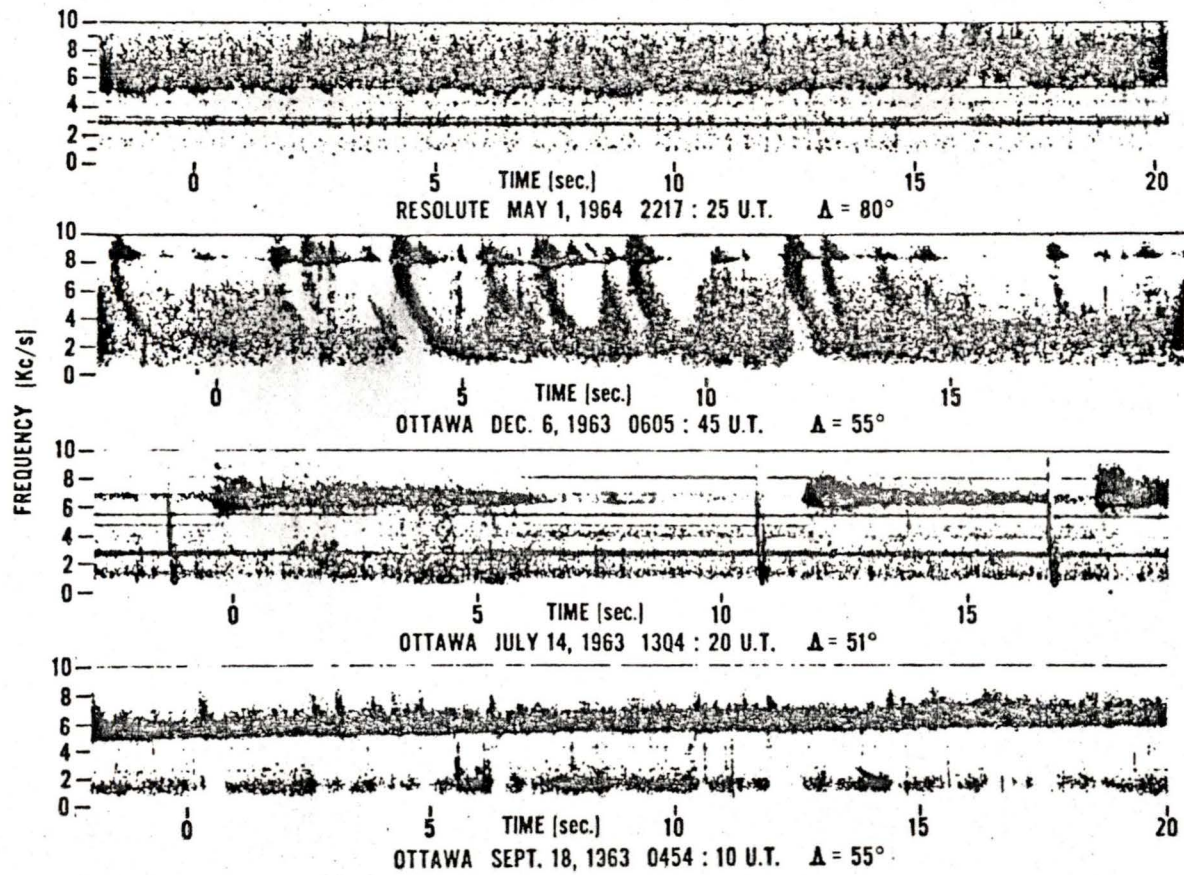


Figure 1.1 Examples of LHR noise bands from the Alouette 1 satellite. The first example is polar LHR noise band; the last three examples are midlatitude LHR noise bands (after McEwen and Barrington, 1967).

at the beginning to about 6 kHz at the end of the record. The origin and cause of these midlatitude LHR noise bands are not clear.

Recently, Gross and Larocca (1972) also studied the 1963 and 1964 Alouette 1 records from the Ottawa station in order to determine the characteristics of VLF hiss showing a sharp lower-cutoff frequency associated with the LHR frequency. They classified the LHR hiss into two types according to its bandwidth. For the wide-bandwidth hiss, the noise band extended up to the highest frequency in the spectrum and also appeared quite intense there. This type of hiss corresponds to polar hiss as observed by McEwen and Barrington (1967). For the narrow bandwidth hiss, both upper and lower frequency limits were observed on the record for the entire event. Further they also classified the narrow band hiss into smooth cutoff hiss (S-type), whistler-associated hiss and erratic cutoff hiss (E-type) according to the duration of the noise, variation of lower frequency cutoff and association with other VLF events. They pointed out that midlatitude hiss might not be caused by one type of source. They also pointed out the possible sources for S-type hiss were resonant-particle instability or whistlers.

LHR noise bands are also found in Injun 3 VLF recordings, though not so frequently as in Alouette 1 recordings. The LHR noise bands observed on OGO 2 records and triggered by fractional-hop whistlers are found to be among the most intense signals observed on these records (Laaspere *et al.*, 1969). One important feature is that both

the Alouette 1 and OGO 2 satellites use electric dipole antennae whereas the Injun 3 satellite uses a magnetic loop antenna. LHR noise bands are also observed by many other satellites such as Injun 5 (Gurnett *et al.*, 1969), OGO 4 (Laaspere and Taylor, 1970), ISIS 1 (Muldrew, 1970), OGO 6 (Laaspere and Johnson, 1971), Alouette 2 (Barrington *et al.*, 1971), OGO 5 (Scarf *et al.*, 1972A, 1972B), OGO 3 (Burtis, 1973), and ISIS 2 (Palmer and Barrington, 1973; James, 1976). From these measurements LHR noise is known to occur at an altitude from several hundred km to several earth radii. The two types of LHR noise, namely midlatitude and polar LHR noise, are usually found in latitude ranges between 40° to 65° and 70° to 85°. The differences in appearance and occurrence of these types of LHR noise suggest different excitation mechanisms. The midlatitude LHR noise seems to be electrostatic (Gurnett *et al.*, 1968) while the polar LHR noise is electromagnetic (Barrington *et al.*, 1971).

Jørgensen (1968) has suggested that the emission named polar LHR by some workers is equivalent to the emission called auroral hiss by others. Laaspere *et al.* (1971) state that polar LHR noise, impulsive auroral-zone VLF hiss studies by Gurnett (1966), high-latitude hiss observed with the VLF experiment of Ariel 3 by Bullough *et al.* (1969), and the broad-band VLF-LF electromagnetic noise termed auroral hiss by Jørgensen (1968), Helliwell (1969) and themselves all represent the same phenomenon.

1.2 Some theories of VLF hiss

A number of different mechanisms have been considered to explain VLF hiss. Ellis (1959) first suggested that auroral-zone VLF hiss emission may be produced by incoherent Cerenkov radiation from the same charged particles that produce aurorae. Later, McKenzie (1963, 1967), Mansfield (1967), Jørgensen (1968), Muldrew (1970), Lim and Laaspere (1972) and others also suggested VLF hiss generation based on incoherent Cerenkov radiation. Another mechanism suggested for VLF hiss is cyclotron emission (Ellis, 1959; McArthur, 1959; Murcray and Pope, 1960; Trulsen and Fejer, 1970).

Ellis (1959) indicated that the theoretical power intensities of the noise using the incoherent radiation process was several orders of magnitude too low to explain the observed power intensities. Lie-mohn (1965) compared the calculated power from the incoherent process with the observed power and found that the observed power exceeded the calculated power by seven orders of magnitude. Hence he considered the incoherent theory inapplicable. Later, Jørgensen (1968) concluded that based on a "realistic" model and more recent data VLF hiss could be generated by incoherent Cerenkov radiation from large, but plausible, fluxes of electrons with energies of the order of 1 keV. However, Jørgensen's (1968) conclusion has been questioned seriously by Gurnett and Frank (1972). Based on their studies of auroral-zone VLF hiss and low energy charged-particle observations with Injun 5 satellite, Gurnett and Frank (1972) concluded that the

observed VLF hiss intensities could not be accounted for by incoherent Cerenkov radiation from the observed electron fluxes, thus indicating that a coherent plasma instability mechanism was involved. Taylor and Shawhan (1974) in their paper also calculated hiss intensities using the incoherent Cerenkov theory and found the calculated values to be small. Hence, they also concluded that it was unlikely that VLF hiss was generated by incoherent Cerenkov radiation from electrons. However they suggested a cooperative mechanism such as partially coherent or amplified Cerenkov emission or an instability mechanism.

The idea of an instability mechanism for the source of VLF hiss is not new. The Landau instability, worked out in detail by Horita and Watanabe (1969) and Horita (1972) may provide an explanation for the origin of VLF emissions associated with the precipitation of electrons. Further, Rao *et al.* (1973) use the theory developed by Horita and Watanabe (1969) and Horita (1972) to calculate the growth rate involving particles with an energy of 1 keV. They conclude that the growth rates predicted by the theory of Horita and Watanabe (1969) and Horita (1972) seem adequate in explaining the disparity between the VLF hiss intensities predicted by the incoherent Cerenkov mechanism theory and those observed by space probes. More recently, James (1973) and Swift and Kan (1975) have also supported the coherent plasma instability theory.

Other mechanisms for VLF hiss than the incoherent Cerenkov radiation, cyclotron emission and Landau instability are also suggested

by other investigators. A special type of Cerenkov mechanism to explain the VLF hiss is the travelling wave tube instability as suggested by Gallet and Helliwell (1959) and Dowden (1962). Instabilities of electromagnetic waves due to anisotropic temperature have been discussed by Harris (1961). Further references for VLF theories can be found in review papers by Kimura (1967), Rycroft (1972) and Gendrin (1975).

After the discovery of LHR noise from the Alouette 1 satellite, Smith *et al.* (1966) suggested that midlatitude LHR noise results from a horizontal ionospheric duct or cavity trap for electromagnetic waves which propagate nearly transverse to the Earth's magnetic field. In order to observe the LHR trapping, the existence of an LHR frequency minimum with height is first required. Then the satellite location in the proper height range between two LHR maxima must be considered. Thus this mechanism only permits generation of LHR noise bands over a well-defined height region. From the Alouette 2 VLF data, it is observed that the LHR noise bands are found up to 3000 km. These observations led to the abandonment of the duct theory by McEwen and Barrington (1967). Later, Gross (1970, 1972) also investigated the duct theory more closely. He concluded that the duct theory may still explain LHR noise from 1000 km to 3000 km, but beyond this range another mechanism is required. Due to the motion of a satellite with respect to the ionosphere, Budko (1969) proposed that a whistler in the vicinity may be the source which excites LHR noise. His mechanism suggested that whenever a whistler reaches the satellite, LHR noise

should be observed. Unfortunately, LHR noise is usually observed much less often than whistlers (Laaspere *et al.*, 1969). Recently, Michkofsky (1974) investigated the mechanism suggested for whistler-triggered LHR noise by considering an irregularity in number density.

In 1975, Eigil Ungstrup reported narrow-band VLF electromagnetic signals observed on a rocket payload launched from ESRANGE (European Space Range) near Kiruna, Sweden. He proposed that the generation mechanism for these observed signals is the high-frequency two-stream instability developed by K. Lee *et al.* (1971). Recently, James (1976) examined data from the VLF receivers aboard the Alouette and ISIS satellites which contained a number of examples of the "saucer" radio phenomenon, so named because of its hyperbolic shape in the amplitude-frequency-time displays. After careful analysis of these "saucers", he thought the "saucer" source may be predicted by the beam-plasma theory.

1.3 Recent satellite observations

Many proton and helium gyrofrequency phenomena have been observed in the ionosphere with both satellites and rockets. Guthart *et al.* (1968) observed proton gyrofrequency band emissions on OGO 2 data. Mosier and Gurnett (1969) and Gurnett and Mosier (1969) reported VLF electrostatic noise bands related to harmonics of the proton gyrofrequency on the Javelin 8.46 sounding rocket. After comparing the observed fine-structure cutoff frequencies with the harmonics of the proton gyrofrequency, Gurnett and Mosier (1969) concluded that these harmonics were generally within the attenuation bands. They suggested that Bernstein mode theory might explain this phenomenon since the Bernstein mode theory for a Maxwellian plasma predicts that the upper-frequency limit of a stop band is at a harmonic of the gyrofrequency. Unfortunately, the results were not in agreement with the frequency limits of the attenuation bands. About a month later, Gurnett *et al.* (1969) also reported the observation of V-shaped VLF hiss events related to harmonics of the proton gyrofrequency on the Injun 5 satellite. They noted that the centre frequencies of the attenuation bands were within about ± 50 Hz of the proton gyrofrequency harmonics. Since these attenuation bands were observed both in the electric and magnetic field frequency spectra, these waves are electromagnetic. Stéfant (1970) pointed out phenomena associated with harmonics of a positive ion (particularly O^+) gyrofrequency. Other phenomena related to the proton gyrofrequency were observed on the Alouette 2,

ISIS 1 and ISIS 2 satellites and reported by Harvey, 1969; Palmer and Barrington, 1973; Horita, 1974; and Ondoh *et al.*, 1975.

Klumpar (1975) has recently reported observing a phenomenon which is similar to the V-shaped VLF hiss event described by Gurnett *et al.* (1969) on data from the ISIS 2 satellite. He noted VLF saucers exhibiting absorption bands in frequency-time spectrograms at integer multiples of the proton gyrofrequency. Since the isolated regions of enhanced positive ion fluxes (proposed to be protons) are often seen to accompany these saucers, he suggested the absorption bands are evidence for energy transfer from the waves to the particles. Horita and Friesen (1975) have observed the amplitude modulation of short fractional hop whistlers at harmonics of the proton and helium gyrofrequency on VLF spectrograms from the ISIS 2 satellite. Most recently, Horita *et al.* (1976) reported modulation at harmonics of the proton gyrofrequency seen on auroral hiss. Their observations show that the proton gyrofrequency from the attenuation bands is smaller than the local proton gyrofrequency, suggesting the generation region is at some height above the satellite.

Examples of VLF spectrograms from the ISIS 2 satellite are given by Figure 1.2 (after Horita *et al.*, 1976) and Figure 1.3. Figure 1.2 shows a spectrogram received by the satellite on December 4, 1971 at 064957 UT when the satellite location was 54.2° N, 103.7° W geographic coordinates and at a height of 1418 km. The noise band appears as a

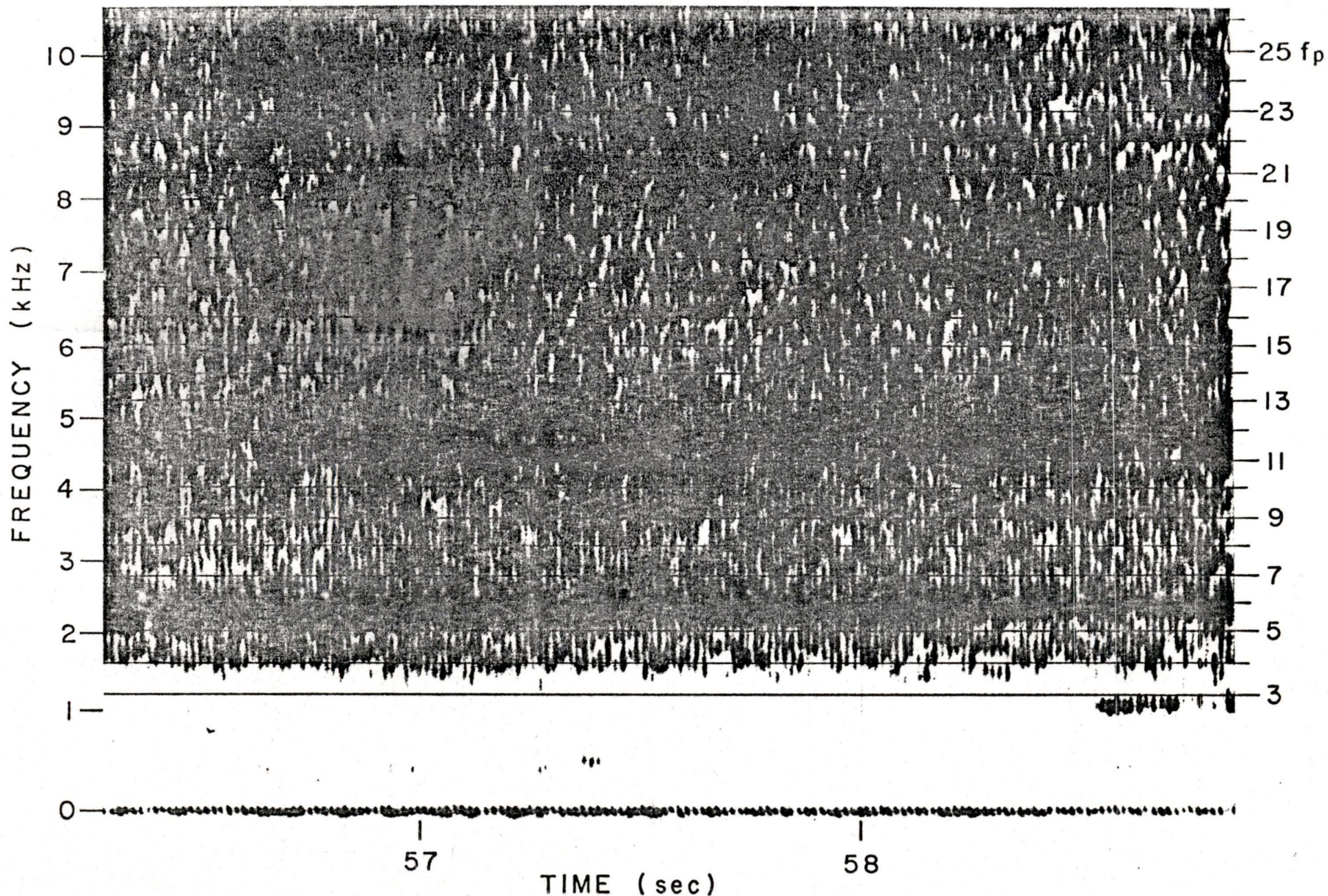


Figure 1.2 ISIS II , OTT , 4 DEC 1971 0649/57 UT (54.2°N, 103.7°W)
SATELLITE HEIGHT 1418 km (after Horita *et al.*)

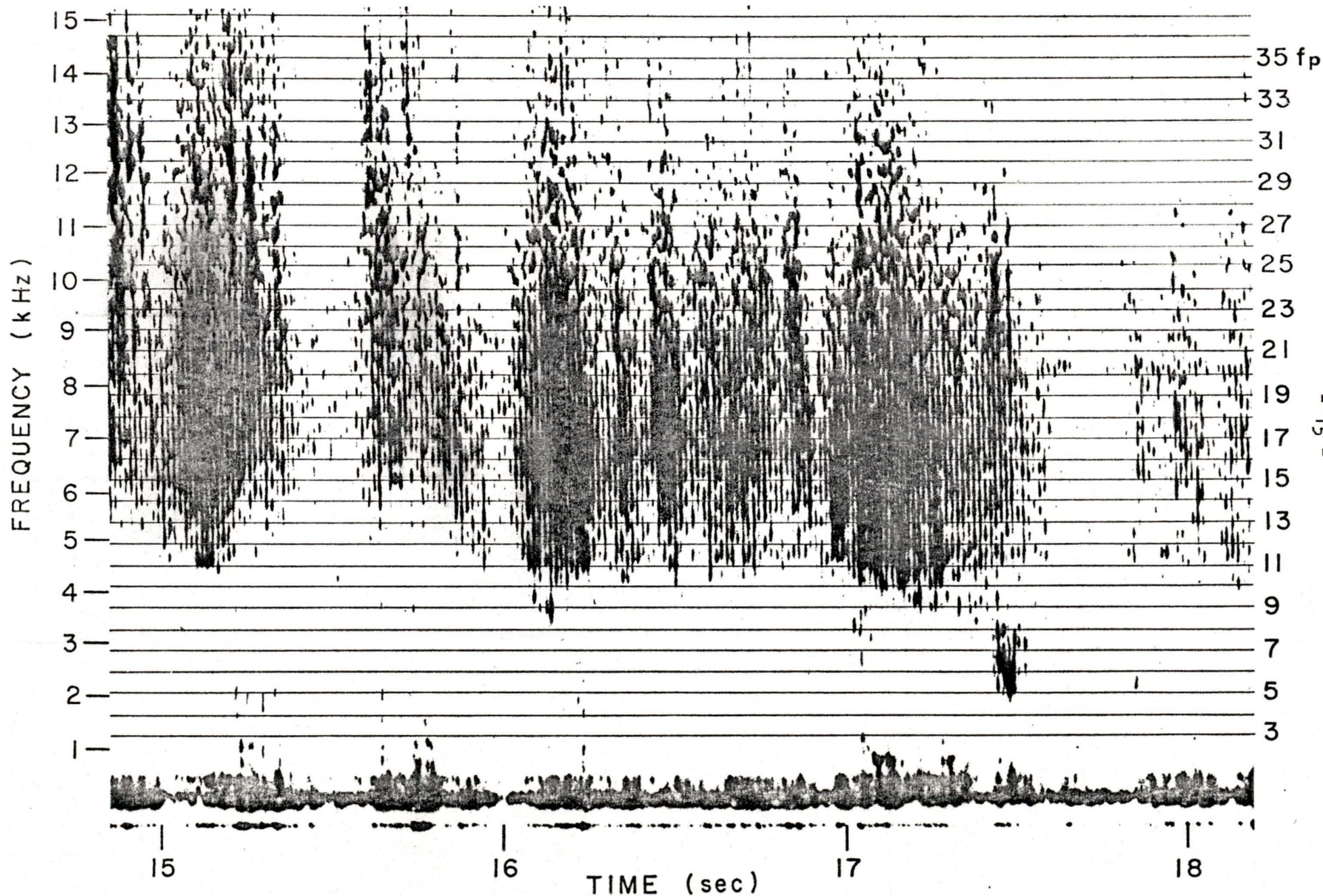


Figure 1.3 6 MAY 1972 0643 UT (55.5°N, 93.3°W)
SATELLITE HEIGHT 1434 km

continuous emission. The frequency range is from about 1.6 kHz to 18 kHz. The local proton gyrofrequency is 490 Hz, while the observed proton gyrofrequency from the spacings of the figure is 403 Hz. Figure 1.3 shows another spectrogram received by the satellite on May 6, 1972 at 064315 UT when the satellite location was 55.5° N, 93.3° W geographic coordinates and at a height of 1434 km. The noise band appears as short bursts lasting for about two seconds. The local proton gyrofrequency is 487 Hz, while the observed proton gyrofrequency from the spacings of the figure is 400 Hz. Both figures show that the absorption bands coincide well with the proton gyrofrequency harmonics, suggesting attenuation at these harmonics.

1.4 Purpose and summary of work covered in this thesis

As intimated in the previous sections the problem to be pursued was stimulated from the prediction that absorption bands at harmonics of the proton gyrofrequency may appear in LHR noise (Horita and Watanabe, 1969, page 72). Such bands were discovered in LHR noise by Horita *et al.* (1976) very recently. In addition, phenomena related to harmonics of the proton, helium and oxygen gyrofrequencies were also reported by other investigators. Many of these observations suggest that the Landau instability theory for the excitation of electrostatic waves proposed by Horita and Watanabe (1969) may be relevant to these various types of VLF signals. The theory may also explain the origin of other VLF emissions associated with the precipitation of electrons. The theory was extended by Horita (1972) employing the full-wave dispersion equation. The extension allows an investigation of the Landau instability process with electromagnetic waves which reduces to the electrostatic case for large values of refractive index.

The purpose of this thesis is to apply the Landau instability theory to find the conditions for which the absorption bands at harmonics of the proton, helium or oxygen gyrofrequencies may appear. The paper by Horita and Watanabe (1969) showed that the absorption bands exist only when a warm plasma is considered. Thus the expansions given in the paper by Horita (1972) must be extended to include finite temperatures. The growth rate expression is obtained by cal-

culating the wave energy and the power transfer between the streaming particles and the propagating wave. The refractive index is calculated by employing the dispersion equations for both a cold and warm plasma. Other parameters such as the mobility tensor, the dielectric tensor and the ratios of the electric field components are also calculated from both the cold and warm plasma expressions.

In chapter 2, we obtain the expression for the power absorption by charged particles in a collisionless warm plasma. Thus the growth rate is computed by considering the rate of increase in energy for the particles to the rate of decrease in energy in the plasma wave. Since the analysis is complicated, it is expedient to use a computer to perform the numerical calculations based on the complex expressions.

In chapter 3, details of the computer calculation are given first. Then calculations for the growth rate are made for different parameters. Calculations of growth rate for wave frequencies around the LHR frequency are emphasized. Also presented are the effects on the growth rate of temperatures of plasma electrons and ions and streaming electrons, the strength of the Earth's magnetic field, and the ion concentration. Then calculations are made to find the absorption bands at harmonics of the proton, helium and oxygen gyrofrequencies.

Comparison of theory with satellite observations and a discussion of the influence of temperature are given in chapter 4. In chapter 5 conclusions and topics for future investigation are given.

CHAPTER 2

LANDAU INSTABILITY THEORY

2.1 Plasma parameters and Maxwell's equations

We first introduce the parameters, in c.g.s. units, which appear frequently in the equations describing a plasma. They are:

$$\Omega_k \text{ (cyclotron or gyro-frequency)} = \frac{q_k B_0}{m_k c} \quad (2.1.1)$$

$$\pi_k \text{ (plasma frequency)} = \sqrt{\frac{4\pi q_k^2 N_k}{m_k}} \quad (2.1.2)$$

where B_0 is the strength of the Earth's magnetic field, q_k , m_k and N_k are the charge with magnitude $Z_k e$, mass and number density of particles of the k^{th} type (designated by subscript k) and c is the velocity of light. In particular, the numerical values of the cyclotron and plasma frequencies for electrons and protons are:

$$\Omega_e \text{ (electron cyclotron frequency)} = 1.7588 \times 10^7 B_0 \text{ rad-sec}^{-1} \quad (2.1.3)$$

$$\Omega_p \text{ (proton cyclotron frequency)} = 9.5789 \times 10^3 B_0 \text{ rad-sec}^{-1} \quad (2.1.4)$$

and

$$\pi_e \text{ (electron plasma frequency)} = 5.7418 \times 10^4 N_e \text{ rad-sec}^{-1} \quad (2.1.5)$$

$$\pi_p \text{ (proton plasma frequency)} = 1.3165 \times 10^3 N_p \text{ rad-sec}^{-1} \quad (2.1.6)$$

It is clear that the cyclotron frequency is proportional to the magnetic field B_0 , while the plasma frequency is proportional to the square root of the number density.

Maxwell's equations, in c.g.s. gaussian units, which govern the plasma, are:

$$\nabla \cdot \vec{B} = 0 \quad (2.1.7)$$

$$\nabla \cdot \vec{E} = 4\pi \sum_k q_k N_k \quad (2.1.8)$$

$$\nabla \times \vec{B} = \frac{4\pi}{c} \vec{j} + \frac{1}{c} \frac{\partial \vec{E}}{\partial t} = \frac{1}{c} \frac{\partial \vec{D}}{\partial t} \quad (2.1.9)$$

$$\nabla \times \vec{E} = - \frac{1}{c} \frac{\partial \vec{B}}{\partial t} \quad (2.1.10)$$

with the current density \vec{j} defined as

$$\vec{j} = \sum_k \epsilon_k q_k N_k \langle \vec{v}_k \rangle \quad (2.1.11)$$

The equation of motion for a single particle of type k is

$$m_k \frac{d\vec{v}_k}{dt} = q_k \left(\vec{E} + \frac{\vec{v}_k}{c} \times \vec{B} \right) \quad (2.1.12)$$

In the above expressions, \vec{B} , \vec{E} and \vec{D} are the magnetic field, the electric field and the electric displacement vectors; ϵ_k is the sign of charge ± 1 ; \vec{v}_k is the velocity of the type k particle. The summation sign \sum_k stands for the sum over each plasma component.

2.2 Power absorption by charged particles in collisionless plasma

Figure 2.1 shows the physical situation in which the Landau instability mechanism is presumed to occur. A tenuous stream of particles (assumed to be electrons), which has a parallel drift velocity \vec{V}_s , traverses the background plasma and interacts with an E.M. (plasma) wave. The instability region is assumed to be small compared to the size of the Earth so that Cartesian coordinates may be used in the analysis. Figure 2.2 shows the relationship in Cartesian coordinates between the direction of motion of the streaming particles and the direction of the wave number vector for the E.M. wave. In this figure, θ is the angle of propagation. The background magnetic field B_0 is assumed to be uniform in space and is along the z-direction, the wave vector \vec{k} is taken in the x-z direction. The background plasma consists of electrons and three positive ions. Although all species of particles have a Maxwellian velocity distribution, they have different perpendicular and parallel temperatures, T_\perp and T_\parallel . The number density of the background particles and the streaming particles are assumed to be uniform in space in the unperturbed state. Collisions between particles are ignored.

From Stix (1962) (henceforth referred to as Reference A), the power absorption per unit volume by all charged particles P_a is given by

$$P_a = \sum_k P_k = \sum_k \left[\frac{Nq\epsilon c}{4B_0} (\vec{E} \cdot \vec{M}^* \cdot \vec{E}^* + \vec{E}^* \cdot \vec{M} \cdot \vec{E}) \right]_k \quad (2.2.1)$$

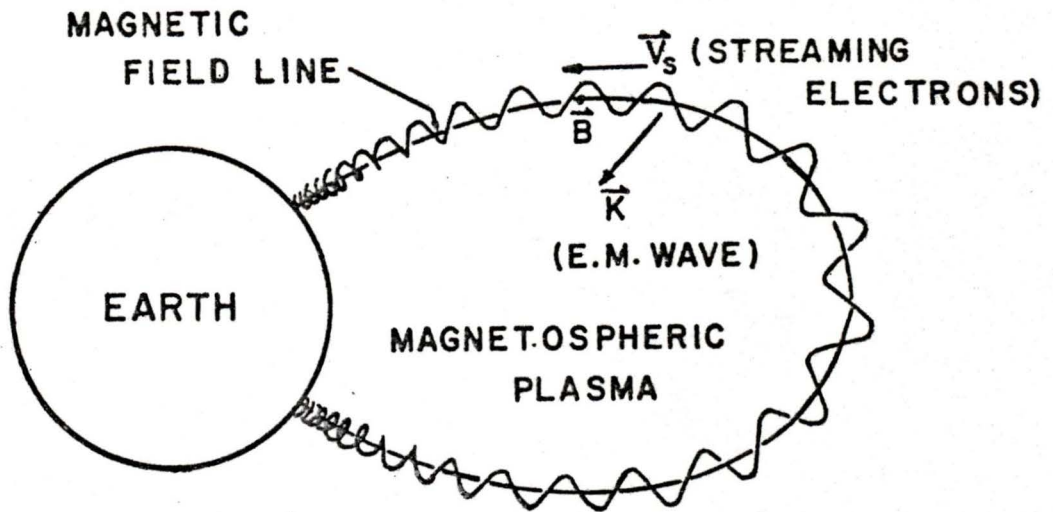


Figure 2.1 Diagram shows physical situation in which the Landau instability is presumed to occur.

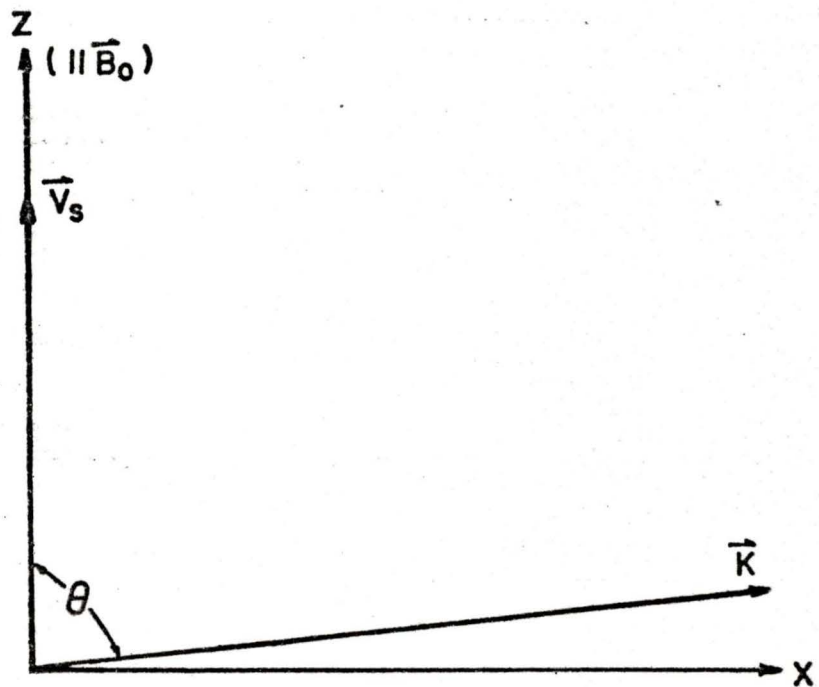


Figure 2.2 Relationship between the mean streaming velocity of the streaming particles and the wave vector for the E.M. wave.

where parameters appropriate to particles of the k^{th} type are to be used in evaluating \vec{M} , the mobility tensor. The other parameters were already introduced. The asterisk denotes the complex conjugate. The summation is over the streaming particles and all plasma components. Using the parameters from section 2.1, we can write Eq. (2.2.1) as

$$P_k = \sum_{n=-\infty}^{\infty} P_{kn} = \frac{\epsilon_k \pi_k^2}{16\pi \Omega_k} \sum_{n=-\infty}^{\infty} \left[\vec{E} \cdot \vec{M}^* \cdot \vec{E}^* + \vec{E}^* \cdot \vec{M} \cdot \vec{E} \right]_n \quad (2.2.2)$$

Equation (2.2.2) may be expanded and expressed in terms of components of the mobility tensor and the x-component of the wave electric field as

$$P_{kn} = \frac{\epsilon_k \pi_k^2}{16\pi \Omega_k} |E_x|^2 \left\{ {}^1T_n + \frac{|E_y|^2}{|E_x|^2} {}^2T_n + \frac{|E_z|^2}{|E_x|^2} {}^3T_n + \frac{(E_x^* E_y - E_y^* E_x)}{|E_x|^2} {}^4T_n + \frac{(E_x^* E_z + E_x E_z^*)}{|E_x|^2} {}^5T_n + \frac{(E_y^* E_z - E_z^* E_y)}{|E_x|^2} {}^6T_n \right\} \quad (2.2.3)$$

We have defined ${}^1T_n = M_{xx} + M_{xx}^*$

$${}^2T_n = M_{yy} + M_{yy}^*$$

$${}^3T_n = M_{zz} + M_{zz}^*$$

$${}^4T_n = M_{xy} - M_{xy}^*$$

$${}^5T_n = M_{xz} + M_{xz}^*$$

$${}^6T_n = M_{yz} - M_{yz}^* \quad (2.2.4)$$

These are the equations which are used to compute the power absorption per unit volume by charged particles. If P_k is positive, the energy is transferred from the wave to the particles, resulting in wave damping. On the other hand, if P_k is negative, the energy is transferred from the particles to the wave, leading to wave amplification. The evaluation of the components of the mobility tensor \vec{M} and the wave electric field will be discussed in the following sections.

2.3 The mobility tensor

From the previous section, we introduce the mobility tensor \hat{M} in computing the power absorption by charged particles in collisionless plasma. The elements of the mobility tensor \hat{M} have the form

$$\hat{M} = \begin{bmatrix} M_{xx} & M_{xy} & M_{xz} \\ M_{yx} & M_{yy} & M_{yz} \\ M_{zx} & M_{zy} & M_{zz} \end{bmatrix} \quad (2.3.1)$$

where (from Equation (9.8), page 188, Ref. A)

$$M_{xx} = \epsilon_k G_k \sum_{n=-\infty}^{\infty} \frac{n^2}{\lambda_k} I_n(\lambda_k) \langle \Theta \rangle_n \quad (2.3.2)$$

$$M_{xy} = i G_k \sum_{n=-\infty}^{\infty} n \left[I_n(\lambda_k) - I'_n(\lambda_k) \right] \langle \Theta \rangle_n \quad (2.3.3)$$

$$M_{xz} = \epsilon_k \frac{G_k}{\Omega_k} \sum_{n=-\infty}^{\infty} n \frac{k_x}{\lambda_k} I_n(\lambda_k) \left[n \langle \bar{\Phi} \rangle_n - \langle \bar{\Psi} \rangle_n \right] \quad (2.3.4)$$

$$M_{yy} = \epsilon_k G_k \sum_{n=-\infty}^{\infty} \left[I_n(\lambda_k) \left(\frac{n^2}{\lambda_k} + 2\lambda_k \right) - 2\lambda_k I'_n(\lambda_k) \right] \langle \Theta \rangle_n \quad (2.3.5)$$

$$M_{yz} = -i \frac{G_k}{\Omega_k} \sum_{n=-\infty}^{\infty} k_x \left[I_n(\lambda_k) - I'_n(\lambda_k) \right] \left[n \langle \bar{\Phi} \rangle_n - \langle \bar{\Psi} \rangle_n \right] \quad (2.3.6)$$

$$M_{zz} = \frac{\epsilon_k \Omega_k e^{-\lambda_k}}{k_z} \sum_{n=-\infty}^{\infty} I_n(\lambda_k) \left[n \langle V_z \bar{\Phi} \rangle_n - \langle V_z \bar{\Psi} \rangle_n \right] \quad (2.3.7)$$

$$M_{yx} = -M_{xy}$$

$$M_{zx} = M_{xz}$$

$$M_{zy} = -M_{yz} \quad (2.3.8)$$

with

$$G_k = - \frac{\Omega_k e^{-\lambda_k} \kappa_0 T_{\perp}^k}{m_k k_z} \quad (2.3.9)$$

In the above expressions, κ_0 is the Boltzmann's constant, T_{\perp}^k is the perpendicular temperature of the k^{th} type particles, V_z is the z-component of the particle velocity, n is an integer, k_x and k_z are the x- and z-components of the wave vector \vec{k} . The function $I_n(\lambda_k)$ and $I'_n(\lambda_k)$ are the modified Bessel function of the first kind and its derivative, respectively. They have the form

$$I_n(\lambda_k) = \sum_{\gamma=0}^{\infty} \frac{1}{\gamma!(n+\gamma)!} \left(\frac{\lambda_k}{2} \right)^{n+2\gamma} \quad (2.3.10)$$

and

$$I'_n(\lambda_k) = \frac{1}{2} \sum_{\gamma=0}^{\infty} \frac{(n+2\gamma)}{\gamma!(n+\gamma)!} \left(\frac{\lambda_k}{2} \right)^{n+2\gamma-1} \quad (2.3.11)$$

with an argument

$$\lambda_k = \frac{k_x^2 \kappa_0 T_{\perp}^k}{\Omega_k^2 m_k} \quad (2.3.12)$$

While the quantities $\langle \mathbb{H} \rangle_n$, $\langle \bar{\phi} \rangle_n$, $\langle \bar{\psi} \rangle_n$, $\langle V_z \bar{\phi} \rangle_n$ and $\langle V_z \bar{\psi} \rangle_n$ are functions with arguments T_{\parallel} , T_{\perp} , ω , k_x and k_z . T_{\parallel} is the parallel temperature for the particle motion parallel to the magnetic field.

$\omega = \omega_r + i\omega_i$ is the wave frequency. They are given by (from Equation (9.13), page 191, Ref. A)

$$\langle \bar{H} \rangle_n = 2 \frac{Q_k^3}{\omega} \left\{ T_k - X_k F_0(\alpha_n) \right\} \quad (2.3.13)$$

$$\langle \bar{\phi} \rangle_n = 2 \frac{\Omega_k Q_k^3}{k_z \omega} \left\{ -T_k + (Y_k - k_z V_z) F_0(\alpha_n) \right\} \quad (2.3.14)$$

$$\langle \bar{\psi} \rangle_n = 2 \frac{Q_k^3}{k_z} \left\{ i \frac{k_z}{Q_k} - Z_k F_0(\alpha_n) \right\} \quad (2.3.15)$$

$$\langle V_z \bar{\phi} \rangle_n = 2 \frac{\Omega_k Q_k^3}{k_z^2 \omega} \left\{ i \frac{k_z}{Q_k} (-Y_k + k_z V_z \frac{T_{ii}^k}{T_{kk}^k}) + (\omega + n\Omega_k) (Y_k - k_z V_z) F_0(\alpha_n) \right\} \quad (2.3.16)$$

$$\langle V_z \bar{\psi} \rangle_n = 2 \frac{Q_k^3}{k_z^2} (\omega + n\Omega_k) \left\{ i \frac{k_z}{Q_k} - Z_k F_0(\alpha_n) \right\} \quad (2.3.17)$$

We have defined

$$Q_k^2 = \frac{m_k}{2 \kappa_0 T_{ii}^k} \quad (2.3.18)$$

$$\alpha_n = Q_k \frac{\omega - k_z V_z + n\Omega_k}{k_z} \quad (2.3.19)$$

$$T_k = i \frac{k_z}{Q_k} \left(1 - \frac{T_{ii}^k}{T_{kk}^k} \right) \quad (2.3.20)$$

$$X_k = (\omega - k_z V_z) + n\Omega_k \left(1 - \frac{T_{ii}^k}{T_{kk}^k} \right) \quad (2.3.21)$$

$$Y_k = (\omega + n\Omega_k) \left(1 - \frac{T_{ii}^k}{T_{kk}^k} \right) \quad (2.3.22)$$

$$Z_k = (\omega - k_z V_z + n\Omega_k) \quad (2.3.23)$$

where $V_z = 0$ except for the streaming particles where $V_z = V_s$. Hence, this shows that the power absorption as mentioned in the previous section is dependent on temperature, wave frequency, components of the wave vector, and other plasma parameters. In particular, if $T_{ii}^k = T_{\perp}^k$ for both plasma electrons and ions and streaming electrons, Equations (2.3.20) to (2.3.22) will become

$$\begin{aligned} T_k &= 0 \\ X_k &= \omega - k_z V_z \\ Y_k &= 0 \end{aligned} \tag{2.3.24}$$

Thus Equations (2.3.12) to (2.3.17) reduce to

$$\langle \bar{H} \rangle_n = -2 \frac{Q_k^3}{\omega} (\omega - k_z V_z) F_0(\alpha_n) \tag{2.3.25}$$

$$\langle \bar{\phi} \rangle_n = -2 \frac{\Omega_k Q_k^3}{\omega} V_z F_0(\alpha_n) \tag{2.3.26}$$

$$\langle \bar{\psi} \rangle_n = 2 \frac{Q_k^3}{k_z} \left\{ i \frac{k_z}{Q_k} - Z_k F_0(\alpha_n) \right\} \tag{2.3.27}$$

$$\langle V_z \bar{\phi} \rangle_n = 2 \frac{\Omega_k Q_k^3}{k_z \omega} V_z \left\{ i \frac{k_z}{Q_k} - (\omega + n\Omega_k) F_0(\alpha_n) \right\} \tag{2.3.28}$$

$$\langle V_z \bar{\psi} \rangle_n = 2 \frac{Q_k^3}{k_z^2} (\omega + n\Omega_k) \left\{ i \frac{k_z}{Q_k} - Z_k F_0(\alpha_n) \right\} \tag{2.3.29}$$

In the above expressions, we also introduce the function $F_0(\alpha_n)$ which is defined in terms of the function $S(\alpha_n)$.

$$F_0(\alpha_n) = \sqrt{\pi} \frac{k_z}{|k_z|} \exp(-\alpha_n^2) + 2i S(\alpha_n) \quad (2.3.30)$$

where

$$S(z) = \exp(-z^2) \int_0^z \exp(t^2) dt \quad (2.3.31)$$

and the argument α_n is defined in Equation (2.3.19). The integral in $S(z)$ is just the complex error function. $F_0(\alpha_n)$ is similar to the function

$$H(z) = \exp(-z^2) \left\{ 2 \int_0^z \exp(p^2) dp + i\sqrt{\pi} \right\} \quad (2.3.32)$$

which can be expressed in series form for small and large values of z on expansion. Expanding for small z , we obtain the series

$$H(z) = i\sqrt{\pi} \exp(-z^2) + 2z \left(1 - \frac{2}{3} z^2 + \frac{4}{15} z^4 + \dots \right) \quad (2.3.33)$$

but expanding for large Z , we get

$$H(z) = i\sqrt{\pi} \exp(-z^2) + \left(\frac{1}{z} + \frac{1}{2z^3} + \frac{3}{4} \frac{1}{z^5} + \dots \right) \quad (2.3.34)$$

We can expand $S(\alpha_n)$ in a similar way. For $|\alpha_n| \ll 1$, we expand $S(\alpha_n)$ in the following series

$$S(\alpha_n) = \alpha_n \left(1 - \frac{2}{3 \cdot 1} \alpha_n^2 + \frac{2 \cdot 2}{5 \cdot 3 \cdot 1} \alpha_n^4 - \frac{2 \cdot 2 \cdot 2}{7 \cdot 5 \cdot 3 \cdot 1} \alpha_n^6 + \dots \right) \quad (2.3.35)$$

while for $|\alpha_n| \gg 1$, we expand $S(\alpha_n)$ in a different series which is

$$S(\alpha_n) = \frac{1}{2\alpha_n} \left(1 + \frac{1}{2\alpha_n^2} + \frac{3}{4} \frac{1}{\alpha_n^4} + \dots \right) \quad (2.3.36)$$

Thus, $F_0(\alpha_n)$ can be written into two forms according to

$$F_0(\alpha_n) = \begin{cases} \sqrt{\pi} \frac{k_z}{|k_z|} + 2i \alpha_n & |\alpha_n| \ll 1 \\ \sqrt{\pi} \frac{k_z}{|k_z|} \exp(-\alpha_n^2) + \frac{i}{\alpha_n} \left(1 + \frac{1}{2\alpha_n^2} + \frac{3}{4} \frac{1}{\alpha_n^4} + \dots\right) & |\alpha_n| \gg 1 \end{cases} \quad (2.3.37)$$

In the computer program, we allow these two cases, but also allow the most general case as stated by Equation (2.3.31).

2.4 The dispersion relation

2.4.1 Cold plasma approximation

In the previous section, we notice that k_x and k_z are introduced in the components of the mobility tensor. The y-component of \vec{k} is chosen to be zero. We can obtain these two components, k_x and k_z , from the dispersion relation.

We first assume a zero temperature plasma immersed in a uniform static magnetic field B_0 which is in the z-direction. The fields considered have the space-time factor

$$\exp [i (\vec{k} \cdot \vec{r} - \omega t)] \quad (2.4.1.1)$$

After Fourier analysis in time and space, Equation (2.1.10) becomes

$$\vec{k} \times \vec{E} - \frac{\omega}{c} \vec{B} = 0 \quad (2.4.1.2)$$

and Equation (2.1.9) becomes

$$\vec{k} \times \vec{B} + \frac{\omega}{c} (\vec{k} \cdot \vec{E}) = 0 \quad (2.4.1.3)$$

Combining Equations (2.4.1.2) and (2.4.1.3) and with the relation of the refractive index \vec{n} and the wave vector \vec{k}

$$\vec{k} = \frac{\omega}{c} \vec{n} \quad (2.4.1.4)$$

we have

$$\vec{n} \times (\vec{n} \times \vec{E}) + \vec{k} \cdot \vec{E} = 0 \quad (2.4.1.5)$$

By solving $\langle \vec{V}_k \rangle$ from the equation of motion and using the relation

$$\hat{K} \cdot \vec{E} = \vec{E} + i \frac{4\pi}{\omega} \vec{j} \quad (2.4.1.6)$$

we obtain

$$\hat{K} \cdot \vec{E} = \begin{bmatrix} S & -iD & 0 \\ iD & S & 0 \\ 0 & 0 & P \end{bmatrix} \begin{bmatrix} E_x \\ E_y \\ E_z \end{bmatrix} \quad (2.4.1.7)$$

where

$$\begin{aligned} S &= 1 - \sum_k \frac{\pi_k^2}{\omega} \frac{\omega}{(\omega^2 - \Omega_k^2)} \\ D &= \sum_k \frac{\pi_k^2}{\omega} \frac{\epsilon_k \Omega_k}{(\omega^2 - \Omega_k^2)} \\ P &= 1 - \sum_k \frac{\pi_k^2}{\omega^2} \end{aligned} \quad (2.4.1.8)$$

Let θ be the angle between \vec{B}_0 and \vec{k} , then we can write Equation (2.4.1.5) only in variable \vec{E}

$$\hat{T} \cdot \vec{E} = 0 \quad (2.4.1.9)$$

where

$$\hat{T} = \begin{bmatrix} S - n^2 \cos^2 \theta & -iD & n^2 \sin \theta \cos \theta \\ iD & S - n^2 & 0 \\ n^2 \sin \theta \cos \theta & 0 & P - n^2 \sin^2 \theta \end{bmatrix} \quad (2.4.10)$$

To have non-trivial values for \vec{E} , the determinant of \hat{T} must vanish. This yields a dispersion relation: a constraint on the values of \vec{k} ,

the wave number, allowed for a given ω , the wave frequency. The determinant of (2.4.1.10) gives

$$A_1 n^4 - A_2 n^2 + A_3 = 0 \quad (2.4.11)$$

where

$$A_1 = S \sin^2 \theta + P \cos^2 \theta$$

$$A_2 = RL \sin^2 \theta + SP(1 + \cos^2 \theta)$$

$$A_3 = P(S^2 - D^2) \quad (2.4.12)$$

In the above, R and L are defined as

$$R = 1 - \sum_k \frac{\pi_k^2}{\omega^2} \left(\frac{\omega}{\omega + \epsilon_k \Omega_k} \right)$$

$$L = 1 - \sum_k \frac{\pi_k^2}{\omega^2} \left(\frac{\omega}{\omega - \epsilon_k \Omega_k} \right) \quad (2.4.13)$$

Thus it can be seen that

$$2S = R + L$$

$$2D = R - L \quad (2.4.1.14)$$

The solution for the dispersion equation (2.4.11) for the wave propagating through the background cold plasma is given in Ref. A (Eq. (1.26), page 12). We are interested in the whistler-mode solution whose wave-normal surface is a dumb-bell lemniscoid. This solution is

$$n^2 = \frac{A_2 - |A_4|}{2A_1} \quad (2.4.1.15)$$

where

$$A_4^2 = [(S^2 - D^2) - PS]^2 \sin^4\theta + 4P^2 D^2 \cos^2\theta \quad (2.4.1.16)$$

Thus the x- and z-components of the wave vector \vec{k} can be obtained from Equations (2.4.1.4) and (2.4.1.15).

2.4.2 Warm plasma

In the case of a warm plasma, Equation (2.4.1.5) is still valid. Since we allow the variation of temperatures for plasma electrons and ions and streaming electrons, we use the components of the dielectric tensor \vec{K} . Writing Equation (2.4.1.5) only in terms of \vec{E} , we have

$$\vec{R} \cdot \vec{E} = 0 \quad (2.4.2.1)$$

where

$$\vec{R} = \begin{bmatrix} K_{xx} - n^2 \cos^2 \theta & K_{xy} & K_{xz} + n^2 \sin \theta \cos \theta \\ K_{yx} & K_{yy} - n^2 & K_{yz} \\ K_{zx} + n^2 \sin \theta \cos \theta & K_{zy} & K_{zz} - n^2 \sin^2 \theta \end{bmatrix} \quad (2.4.2.2)$$

To have non-trivial solutions for \vec{E} , the determinant of \vec{R} must vanish. This yields an equation

$$B_1 n^4 - B_2 n^2 + B_3 = 0 \quad (2.4.2.3)$$

where

$$B_1 = (K_{xx} \sin^4 \theta + K_{zz} \cos^4 \theta) + 2K_{xz} (\sin^3 \theta \cos \theta + \sin \theta \cos^3 \theta) + (K_{xx} + K_{zz}) \sin^2 \theta \cos^2 \theta \quad (2.4.2.4)$$

$$B_2 = [K_{xx} (K_{yy} + K_{zz}) + K_{xy}^2 - K_{xz}^2] \sin^2 \theta + [K_{zz} (K_{xx} + K_{yy}) + K_{yz}^2 - K_{xz}^2] \cos^2 \theta + 2[K_{xz} K_{yy} - K_{xy} K_{yz}] \sin \theta \cos \theta \quad (2.4.2.5)$$

$$B_3 = K_{xx} (K_{yy} K_{zz} + K_{yz}^2) + 2K_{yx} K_{xz} K_{yz} + K_{xy}^2 K_{zx} - K_{xz}^2 K_{yy} \quad (2.4.2.6)$$

Thus the solution for the whistler-mode is

$$n^2 = \frac{B_2 - |B_4|}{2B_1} \quad (2.4.2.7)$$

with

$$B_4^2 = B_2^2 - 4B_1B_3$$

Then values of k_x and k_z can be obtained in terms of the refractive index and the components of the dielectric tensor. Indeed we also can obtain a ratio for the electric field components in terms of the refractive index and dielectric tensor from Equation (2.4.2.2).

These give

$$\frac{E_y}{E_x} = \frac{(n^2 \sin\theta \cos\theta + K_{xz}) K_{yx} - K_{yz}(k_{xx} - n^2 \cos^2\theta)}{K_{yz} K_{xy} - (n^2 \sin\theta \cos\theta + K_{xz})(K_{yy} - n^2)} \quad (2.4.2.9)$$

$$\frac{E_z}{E_x} = \frac{K_{xy} K_{yz} - (K_{yy} - n^2)(K_{xx} - n^2 \cos^2\theta)}{(K_{yy} - n^2)(n^2 \sin\theta \cos\theta + K_{xz}) - K_{xy} K_{yz}} \quad (2.4.2.10)$$

These ratios are used to express the power absorption in terms of $|E_x|^2$. Thus once we know the x-component of the electric field, we can compute the power absorption.

2.5 The dielectric tensor

The elements of the dielectric tensor, as introduced in the previous section, have the form

$$\vec{\vec{K}} = \begin{bmatrix} K_{xx} & K_{xy} & K_{xz} \\ K_{yx} & K_{yy} & K_{yz} \\ K_{zx} & K_{zy} & K_{zz} \end{bmatrix} \quad (2.5.1)$$

From Equation (2.4.1.6), we obtain an equation for $\vec{\vec{K}}$ with other parameters. Using the relationship between $\langle \vec{V}_k \rangle$ and the mobility tensor by

$$\langle \vec{V}_k \rangle = \frac{c}{B_0} \vec{M}_k \cdot \vec{E} \quad (2.5.2)$$

Now the current density becomes

$$\vec{j} = \frac{c}{B_0} \sum_k \epsilon_k q_k N_k \vec{M}_k \cdot \vec{E} \quad (2.5.3)$$

Combining Equations (2.5.3) and (2.4.1.6), we have

$$\vec{\vec{K}} = \vec{\vec{I}} + i \sum_k F_k \vec{\vec{M}}_k \quad (2.5.4)$$

with

$$F_k = \frac{\epsilon_k \pi_k^2}{\omega \Omega_k} \quad (2.5.5)$$

and $\vec{\vec{I}}$ is the unit dyad. Thus the components of the dielectric tensor are

$$K_{xx} = 1 + i \sum_k \sum_{n=-\infty}^{\infty} \epsilon_k G_k F_k \frac{n^2}{\lambda_k} I_n(\lambda_k) \langle \mathbb{H} \rangle_n \quad (2.5.6)$$

$$K_{xy} = - \sum_k \sum_{n=-\infty}^{\infty} G_k F_k n [I_n(\lambda_k) - I'_n(\lambda_k)] \langle \mathbb{H} \rangle_n \quad (2.5.7)$$

$$K_{xz} = i \sum_k \sum_{n=-\infty}^{\infty} n F_k \frac{\epsilon_k G_k k_x}{\Omega_k \lambda_k} I_n(\lambda_k) [n \langle \bar{\phi} \rangle_n - \langle \bar{\psi} \rangle_n] \quad (2.5.8)$$

$$K_{yy} = 1 + i \sum_k \sum_{n=-\infty}^{\infty} \epsilon_k G_k F_k [I_n(\lambda_k) \left(\frac{n^2}{\lambda_k} + 2\lambda_k \right) - 2\lambda_k I'_n(\lambda_k)] \langle \mathbb{H} \rangle_n \quad (2.5.9)$$

$$K_{yz} = \sum_k \sum_{n=-\infty}^{\infty} k_x \frac{G_k F_k}{\Omega_k} [I_n(\lambda_k) - I'_n(\lambda_k)] [n \langle \bar{\phi} \rangle_n - \langle \bar{\psi} \rangle_n] \quad (2.5.10)$$

$$K_{zz} = 1 + i \sum_k \sum_{n=-\infty}^{\infty} \epsilon_k \frac{F_k \Omega_k e^{-\lambda_k}}{k_z} I_n(\lambda_k) [n \langle V_{z\bar{\phi}} \rangle_n - \langle V_{z\bar{\psi}} \rangle_n] \quad (2.5.11)$$

and

$$K_{yx} = -K_{xy}$$

$$K_{zx} = K_{xz}$$

$$K_{zy} = -K_{yz} \quad (2.5.12)$$

Where the values for G_n , $I_n(\lambda_k)$, $\langle \mathbb{H} \rangle_n$, $\langle \bar{\phi} \rangle_n$, $\langle \bar{\psi} \rangle_n$, $\langle V_{z\bar{\phi}} \rangle_n$, $I'_n(\lambda_k)$ and $\langle V_{z\bar{\psi}} \rangle_n$ have already been introduced. In general we use Equations (2.3.13) to (2.3.17) for $\langle \mathbb{H} \rangle_n$, $\langle \bar{\phi} \rangle_n$, $\langle \bar{\psi} \rangle_n$, $\langle V_{z\bar{\phi}} \rangle_n$ and $\langle V_{z\bar{\psi}} \rangle_n$ which reduce to Equations (2.3.25) to (2.3.29) if $T_n^k = T_e^k$ for plasma electrons and ions and streaming electrons.

2.6 Wave energy and growth rate

The wave energy is given by

$$W = \frac{1}{16\pi} [\vec{B}^* \cdot \vec{B} + \vec{E}^* \cdot (\frac{\partial}{\partial \omega} (\omega \vec{K}_h)) \cdot \vec{E}] \quad (2.6.1)$$

The magnetic and electric fields are related by Equation (2.4.1.2).

\vec{K}_h is the Hermitian part of the dielectric tensor which is defined

as

$$\vec{K}_h(\omega_r) = \frac{1}{2} [\vec{K}(\omega_r) + \vec{K}^{\dagger}(\omega_r)] \quad (2.6.2)$$

where \vec{K}^{\dagger} denotes the Hermitian conjugate of \vec{K} ,

$$\vec{K}^{\dagger} = \begin{bmatrix} K_{xx}^* & K_{xy}^* & K_{xz}^* \\ K_{yx}^* & K_{yy}^* & K_{yz}^* \\ K_{zx}^* & K_{zy}^* & K_{zz}^* \end{bmatrix} \quad (2.6.3)$$

which is the complex conjugate of the transposed matrix. Since the expression for \vec{K}_h is very complicated for a warm plasma, we define the term $\frac{\partial}{\partial \omega} [\omega \vec{K}_h]$ as

$$\frac{\partial}{\partial \omega} (\omega \vec{K}_h) = \begin{bmatrix} C_{xx} & C_{xy} & C_{xz} \\ C_{yx} & C_{yy} & C_{yz} \\ C_{zx} & C_{zy} & C_{zz} \end{bmatrix} \quad (2.6.4)$$

where the elements C_{ij} are obtained numerically and have the form

$$C_{ij} = \frac{(\omega + \Delta\omega) [\vec{K}_h(\omega + \Delta\omega)]_{ij} - (\omega - \Delta\omega) [\vec{K}_h(\omega - \Delta\omega)]_{ij}}{2\Delta\omega}$$

$$i = x, y, z$$

$$j = x, y, z$$

(2.6.5)

where $\Delta\omega$ is very small when compared with ω . Thus substituting Equations (2.4.1.2) and (2.6.4) into Equation (2.6.1), we have

$$W = \frac{1}{16\pi} |E_x|^2 [L_1 + L_2] \quad (2.6.6)$$

with

$$L_1 = \left(\frac{c^2}{\omega^2} k_x^2 + C_{xx}\right) + \frac{|E_y|^2}{|E_x|^2} \left[\frac{c^2}{\omega^2} (k_x^2 + k_z^2) + C_{yy}\right] + \frac{|E_z|^2}{|E_x|^2} \left(\frac{c^2}{\omega^2} k_x^2 + C_{zz}\right) \quad (2.6.7)$$

$$L_2 = \frac{E_x^* E_y}{|E_x|^2} C_{xy} + \frac{E_x E_y^*}{|E_x|^2} C_{yx} + \frac{E_y^* E_z}{|E_x|^2} C_{yz} + \frac{E_z E_y^*}{|E_x|^2} C_{zy} \\ + \frac{E_x^* E_z}{|E_x|^2} \left[C_{xz} - \frac{c^2}{\omega^2} k_x k_z\right] + \frac{E_z E_x^*}{|E_x|^2} \left[C_{zx} - \frac{c^2}{\omega^2} k_x k_z\right] \quad (2.6.8)$$

In the case of a cold plasma, W reduces to a simple form and this has been given by Horita (1972). Equation (2.6.6) allows the variation of temperatures for plasma electrons and ions and streaming electrons. The ratios of $\frac{E_y}{E_x}$ and $\frac{E_z}{E_x}$ have already been discussed

From the result of sections 2.2 and 2.6, the wave growth rate can be obtained by computing the energy balance. This is done by equating the rate of increase in energy for the particles to the rate of decrease in energy in the plasma wave, so that the growth rate is given by

$$\omega_i = -\frac{1}{2} \frac{P_a}{W} \quad (2.6.9)$$

Hence we have the equations for the computer program (see Appendix A). The complete analysis will be presented in chapter 3 with the relevant ionospheric parameters from ISIS 2 satellite data.

CHAPTER 3

COMPUTER ANALYSIS

3.1 Detailed computer calculation procedure

The cyclotron and plasma frequencies for electrons and ions are first calculated by using Equations (2.1.1) and (2.1.2) in the program which was developed to calculate the power absorption P_a by charged particles, the wave energy W and the growth rate ω_i . This is because cyclotron frequencies are dependent on the strength of the magnetic field B_0 , while the plasma frequencies are functions of the number densities N_k . Both B_0 and K_k are constants for a particular set of ionospheric parameters. Then the lower hybrid resonance (LHR) frequency is calculated. For a cold plasma, under the assumption of charge neutrality and $S = 0$, the LHR frequency can be computed from the form

$$\frac{1}{\omega_{LH}^2} = \frac{1}{\sum_k \pi_k^2} + \frac{1}{\Omega_e \sum_k \Omega_k} \quad (3.1.1)$$

where ω_{LH} is the LHR angular frequency. π_k and Ω_k are the plasma and cyclotron frequencies for particles of the k^{th} type. Ω_e is the electron cyclotron frequency.

The background plasma considered consists of electrons and three species of positive ions. The data from the ISIS 2 satellite are used for the analysis. According to Hoffman *et al.* (1974), the positive

ions observed most of the time by the ISIS 2 satellite are H^+ , He^+ and O^+ . Though they also report that N_2^+ , NO^+ and O_2^+ were also present during the August, 1972 magnetic storm, we do not consider these ions but only H^+ , He^+ and O^+ ions. For each particular data set used for the program, a table of number densities and other ionospheric parameters are listed.

The number density of the nonthermal electrons is assumed to be very small in comparison with the number densities of other species. We also assume that the streaming particles are electrons with a kinetic energy of 10 keV. Evidence for the existence of streaming electrons associated with auroral phenomena is presented by Cloutier *et al.* (1970). Moreover, the existence of the inverted-V events (Gurnett and Frank, 1972) is consistent with a downward stream of electrons with a streaming energy comparable to the thermal energy of the beam. Monoenergetic electrons with peak energy between 10 - 14 keV observed during a visible aurora have been reported already by Albert (1967A, 1967B). The value of 10 keV is chosen simply because electrons with energy of that order are known to be related to various geophysical phenomena; it is not implied that the 10 keV energy is optimum for triggering the instability process under consideration. This energy gives the streaming electrons a streaming velocity of 6×10^9 cm/sec and a parallel temperature of 7.92×10^7 ° K. The perpendicular and parallel temperatures of the plasma ions and electrons are chosen to be 4000° K. This number is considered reasonable since temperatures determined from cylindrical electro-

static probe (CEP) data have values of $5000^\circ \pm 2000^\circ \text{ K}$ (James, 1976). The relativistic correction for the streaming particles has also been considered. The relativistic result can be obtained by making changes in the effective mass of the streaming electrons. Thus we are dealing with the factor $[1 - (v_s/c)^2]^{1/2} = 98$ percent. This relativistic correction provides our analysis with a more accurate result.

Next is calculated the power absorption P_a given by Equation (2.2.3) which is expressed in terms of components of the mobility tensor and the x-component of the wave electric field. Thus to calculate P_a , we first evaluate the components of the mobility tensor. We only need to know six of the components since the other three components can be found by symmetry. These components are listed in Equations (2.3.2) to (2.3.8). They are functions of G_k , λ_k , $I_n(\lambda_k)$, $I'_n(\lambda_k)$, $\langle \mathbb{H} \rangle_n$, $\langle \bar{\phi} \rangle_n$, $\langle \bar{\psi} \rangle_n$, $\langle v_{z\bar{\phi}} \rangle_n$ and $\langle v_{z\bar{\psi}} \rangle_n$. A subprogram is written to evaluate the modified Bessel function of the first kind $I_n(\lambda_k)$ and its first derivative $I'_n(\lambda_k)$. The formulae for $I_n(\lambda_k)$ and $I'_n(\lambda_k)$ are given by Equations (2.3.10) and (2.3.11) with argument λ_k . To evaluate $\langle \mathbb{H} \rangle_n$, $\langle \bar{\phi} \rangle_n$, $\langle \bar{\psi} \rangle_n$, $\langle v_{z\bar{\phi}} \rangle_n$ and $\langle v_{z\bar{\psi}} \rangle_n$ by using Equations (2.3.13) to (2.3.17), another subprogram is written. Attention should be given to the function $F_0(\alpha_n)$ which is defined in terms of $S(\alpha_n)$. The term $S(\alpha_n)$ involves the complex error function. It can be expressed in different forms according to the size of α_n . Taking the first two terms of the series from Equations (2.3.35) and (2.3.36) we have

$$S(\alpha_n) = \begin{cases} \alpha_n - \frac{2}{3} \alpha_n^2 & |\alpha_n| \ll 1 \\ \frac{1}{2\alpha_n} + \frac{1}{4\alpha_n^2} & |\alpha_n| \gg 1 \end{cases} \quad (3.1.2)$$

The program is very general and allows the integration form

$$S(\alpha_n) = \exp(-\alpha_n^2) \int_0^{\alpha_n} \exp(t^2) dt \quad (3.1.3)$$

Thus the whole program can handle all values of α_n . A special case for Equations (2.3.13) to (2.3.17) is when T_u^k is equal to T_L^k for plasma electrons and ions and streaming electrons.

The x- and z-components of the wave vector \vec{k} are functions of the refractive index which is related to the wave vector by Equation (2.4.1.4). To find the refractive index, we solve the dispersion equation. n^2 is first calculated by solving the dispersion equation for a cold plasma, then it is calculated for a warm plasma. The two components n_x and n_z have the form

$$\begin{aligned} n_x &= n \sin\theta \\ n_z &= n \cos\theta \end{aligned} \quad (3.1.4)$$

thus

$$\begin{aligned} k_x &= n_x \sin\theta \\ k_z &= n_z \cos\theta \end{aligned} \quad (3.1.5)$$

where k_x and k_z are real numbers. We also obtain the ratios of the electric field components, E_y/E_x and E_z/E_x , in terms of the refractive index and the dielectric tensor from the dispersion equation for a warm plasma. Their expressions have been shown in Equations

(2.4.2.9) and (2.4.2.10). Once E_y/E_x and E_z/E_x are evaluated, the other terms of the electric field in the expression of P_a can be computed; i.e.

$$\frac{E_x^* E_y - E_y^* E_x}{|E_x|^2} = \left[\frac{E_y}{E_x} \right] - \left[\frac{E_y}{E_x} \right]^* \quad (3.1.6)$$

$$\frac{E_x^* E_z + E_x E_z^*}{|E_x|^2} = \left[\frac{E_z}{E_x} \right] + \left[\frac{E_z}{E_x} \right]^* \quad (3.1.7)$$

and

$$\frac{E_y^* E_z - E_z^* E_y}{|E_x|^2} = \left[\frac{E_y}{E_x} \right]^* \left[\frac{E_z}{E_x} \right] - \left[\frac{E_z}{E_x} \right]^* \left[\frac{E_y}{E_x} \right] \quad (3.1.8)$$

where the asterisk denotes the complex conjugate. The dielectric tensor $\hat{\vec{K}}$ is related to the mobility tensor $\hat{\vec{M}}$ by Equation (2.5.4). Thus once the components of the mobility tensor are evaluated, the components of the dielectric tensor can be calculated. Hence the required P_a is calculated.

The program then calculates the wave energy W . The tensor $\frac{\partial}{\partial \omega} [\omega \hat{\vec{K}}_n]$ is evaluated numerically because for a warm plasma the components of the Hermitian part of the dielectric tensor $\hat{\vec{K}}_h$ is, in general, quite complicated. Then W is computed from Equations (2.6.6) to (2.6.8). In the case of a cold plasma, the tensor $\frac{\partial}{\partial \omega} [\omega \hat{\vec{K}}_n]$ reduces to a simple form which is in terms of the parameters S , D and P as defined in the last chapter. These have been done by Horita (1972) and also by Swift and Kan (1975) when they derived the expression for W . Once P_a and W are evaluated, the

growth rate ω_i is calculated by considering the balance of energy, applying Eq. (2.6.9). Thus these results allow us to investigate the theory developed in the last chapter.

The program is run on the University of Victoria IBM 370-145 computer. The storage needed for the whole program is 76 K. The computing time for each run is about 5 to 10 minutes depending on the nature of the job. The results for the analysis are shown in the following sections. A list of flowcharts and the original program can be found in Appendix A.

3.2 Computer results

To illustrate the theory developed in chapter 2, we first investigated the growth rate for some particular ionospheric parameters. As the power absorption P_a is dependent on parameters such as the strength of the Earth's magnetic field B_0 , the angle of propagation θ , the wave frequency ω_r , the ion concentrations N_k and the temperatures for plasma electrons and ions (T_e^P and T_i^P) and streaming electrons (T_e^S and T_i^S), it is interesting to study the effects of these parameters on the growth rate. Hence the theoretical results allow us to study the influence of these parameters on the phenomena related to harmonics of the ion gyrofrequencies appearing on the VLF spectrograms. In the whole analysis, the number density of the non-thermal electrons is assumed to be 1 cm^{-3} . The streaming electrons are assumed to have a streaming velocity of $6 \times 10^9 \text{ cm/sec}$ corresponding to a thermal energy of 10 keV as stated previously. The number densities of H^+ , He^+ and O^+ are obtained from the ISIS 2 satellite data kindly supplied by Dr. J.H. Hoffman. The wave frequency ω_r and the growth rate ω_i are normalized by the LHR frequency ω_{LH} : $\omega_r^! = \omega_r / \omega_{LH}$ and $\omega_i^! = \omega_i / \omega_{LH}$.

TABLE 3.1

Numerical values of ionospheric parameters at an altitude of
1431 km and 82.06° geomagnetic latitude

Strength of the Earth's magnetic field $B_0 = 0.32$ gauss

Number density of thermal electrons $N_e = 1.555 \times 10^4 \text{ cm}^{-3}$

Number density of nonthermal electrons $N_s = 1 \text{ cm}^{-3}$

Number density of protons (H^+) $N_{\text{H}^+} = 4.0 \times 10^2 \text{ cm}^{-3}$

Number density of helium ions (He^+) $N_{\text{He}^+} = 1.5 \times 10^1 \text{ cm}^{-3}$

Number density of oxygen ions (O^+) $N_{\text{O}^+} = 1.5 \times 10^4 \text{ cm}^{-3}$

Mean streaming velocity of nonthermal electrons $V_s = 6 \times 10^9 \text{ cm/sec}$

Calculated LHR frequency $\omega_{\text{LH}} = 30580 \text{ rad/sec}$

TABLE 3.2

Numerical values of the cyclotron and plasma frequencies at an altitude of
1431 km and 82.06° geomagnetic latitude

Ion type	Gyrofrequency (rad/sec)	Plasma frequency (rad/sec)
Electron	5.628×10^6	7.035×10^6
Proton (H^+)	3.065×10^3	2.633×10^4
Helium (He^+)	7.715×10^2	8.089×10^3
Oxygen (O^+)	1.930×10^2	4.046×10^4

3.2.1 Growth rate for wave frequencies around the LHR frequency

Equation (2.6.9) is programmed so that the growth rate can be calculated using the ionospheric parameters given in Table 3.1. The data are taken when the satellite was at an altitude of 1431 km and 82.06° geomagnetic latitude. The fractional abundance of H^+ , He^+ and O^+ are 2.75%, 0.93% and 96.5% respectively. Because of charge neutrality and from $S = 0$, the LHR frequency has a value of 30580 rad/sec (about 4.87 kHz). The strength of the Earth's magnetic field at this altitude is found to be 0.32 gauss. With the values of number densities N_k and magnetic field strength B_0 , the gyrofrequencies and the plasma frequencies of the electrons and positive ions are computed. Their values are listed in Table 3.2. The perpendicular and parallel temperatures of plasma electrons and ions are assumed to be equal and have a value of 4000° K. This number is considered reasonable since temperatures determined from CEP data have values of $5000^\circ \pm 2000^\circ$ K (James, 1976). We assume the streaming electrons have more thermal energy in the parallel direction than in the perpendicular direction. Thus a value of $T_{\parallel}^S/T_{\perp}^S = 1.98 \times 10^4$ is chosen.

Figure 3.1 shows the normalized growth rate $\omega_i^!$ versus θ with $\omega_r^! = 1.20, 1.63$ and 2.50 and with parameter $T_{\parallel}^P/T_{\perp}^P = 1$. Note that the scales are different for positive and negative values of $\omega_i^!$. With increasing θ , $\omega_i^!$ increases from a small positive value about zero to a maximum, decreases through zero to exhibit a minimum

before becoming positive again, reaches a positive maximum, and drops to zero at $\theta = \theta_{res}$, where θ_{res} is given by

$$\tan^2 \theta_{res} = -\frac{P}{S} \quad (3.2.1.1)$$

Then it passes through θ_{res} to a negative minimum and goes back to zero again. Curves are not plotted for this part in order to avoid a tangle of lines.

According to Horita (1972), the two regions in the θ space in which positive growth rates occur are designated the "electromagnetic" and "electrostatic" regions. The "electromagnetic" region occurs for smaller values of θ while the "electrostatic" region occurs near the "resonance" angle for which the refractive index tends to infinity. Hence we adopt these two designations for our description too.

Note that the "electrostatic" region for $\omega_r^i = 1.20$ does not exist due to the influence of T_e^P/T_i^P and T_e^S/T_i^S (the effect of the temperatures of plasma electrons and ions and streaming electrons will be clear in the next section). Both $\omega_r^i = 1.63$ and $\omega_r^i = 2.50$ exhibit "electrostatic" regions which are over an extremely small interval in θ . Thus the curves plotted in these regions on the figure appear as straight lines. The "electromagnetic" and "electrostatic" regions are separated by a region where damping occurs. It has been found that the maximum growth rate for the "electromagnetic" region occurs when $\omega_r^i = 5.5$ (where $\omega_i^i = 3.55 \times 10^{-6}$), then the growth rate decreases with increasing ω_r^i . In general, the

growth rate in the "electrostatic" region is larger than in the "electromagnetic" region. The resonance angle θ_{res} also decreases with increasing ω_r' , becoming zero when $P = 0$. Thus from Equation (2.4.1.10) the wave frequency is given by

$$\omega_r^2 = \pi_e^2 + \sum_{ions} \pi_i^2 \quad (3.2.1.2)$$

It is also found that when the frequency decreases below the LHR frequency, no "electrostatic" region appears and only the "electromagnetic" region exists.

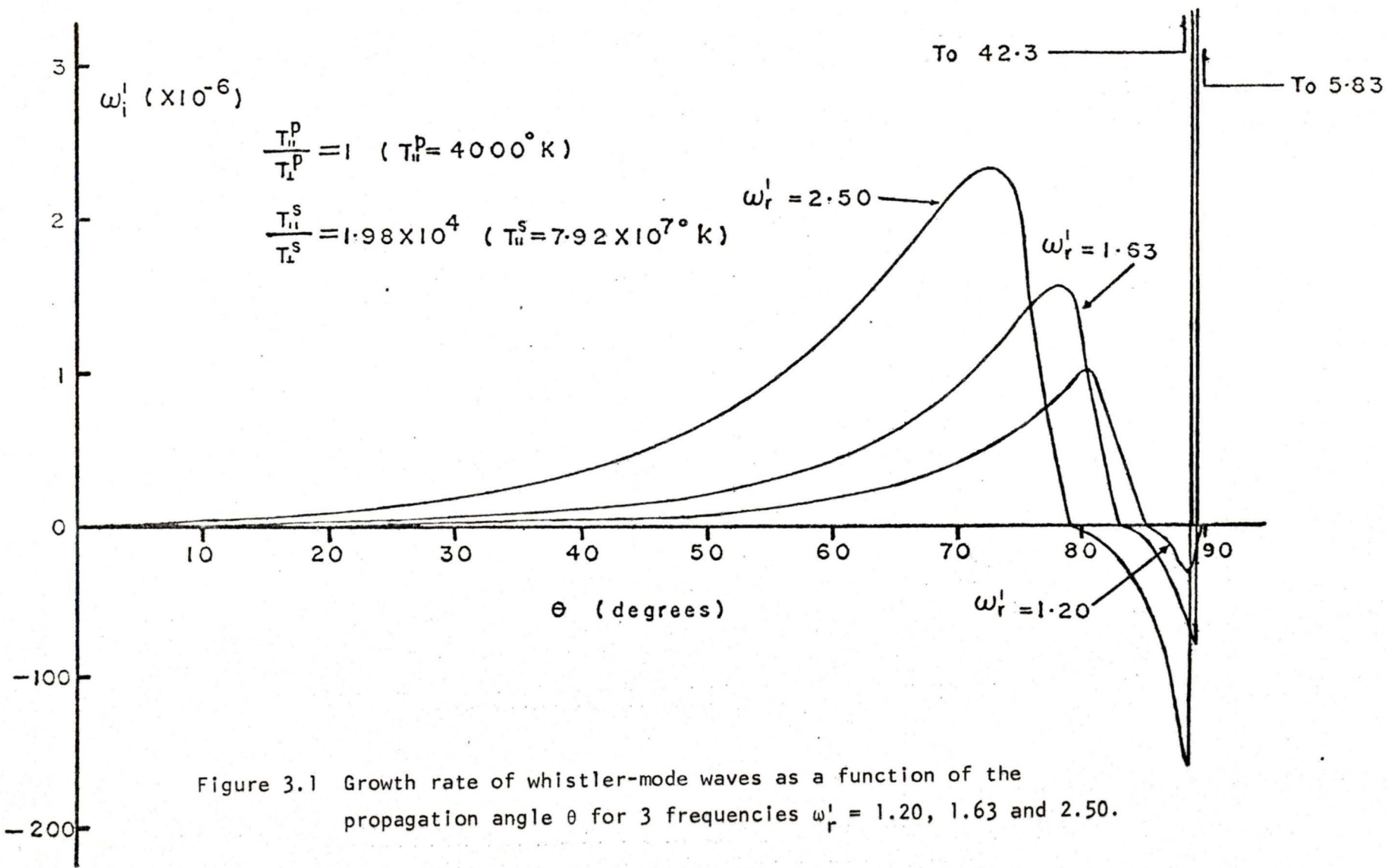


Figure 3.1 Growth rate of whistler-mode waves as a function of the propagation angle θ for 3 frequencies $\omega_r' = 1.20, 1.63$ and 2.50 .

3.2.2 Effect of T_{ii}^P/T_{ii}^D and T_{ii}^S/T_{ii}^S on the growth rate

The dependence on temperature anisotropy is discussed in this section. The ionospheric parameters as listed in Table 3.1 are used again. With $T_{ii}^P/T_{ii}^D = 1$ and $\omega_i^1 = 1.8$, the normalized growth rate versus θ for the three values 0.5, 1 and 5 of T_{ii}^S/T_{ii}^S are plotted. Figure 3.2 shows these three curves. Again the scales are different for positive and negative values of ω_i^1 . The growth rate increases very rapidly in the "electromagnetic" region for $T_{ii}^S/T_{ii}^S = 0.5$ with increasing θ . On the other hand, ω_i^1 increases very slowly for $T_{ii}^S/T_{ii}^S = 5$. The figure shows that in the "electromagnetic" region, $T_{ii}^S/T_{ii}^S = 0.5$ has the largest value, while in the "electrostatic" region $T_{ii}^S/T_{ii}^S = 1$ has the largest value, followed by $T_{ii}^S/T_{ii}^S = 0.5$. Again the curves pass through θ_{res} to a negative minimum and go back to zero at values close to 90° . To avoid a tangle of lines, the curves are not plotted for this part.

The situation reverses for the plasma temperature ratios. With $T_{ii}^S/T_{ii}^S = 1$ and $\omega_i^1 = 1.8$, growth rate versus θ for the three values 0.5, 1 and 5 of T_{ii}^P/T_{ii}^D are plotted. Figure 3.3 shows these three curves for $\theta = 0^\circ$ to $\theta = 82^\circ$. This figure shows the "electromagnetic" regions for the three values of T_{ii}^P/T_{ii}^D only. Indeed the values of the growth rates for the three curves are very close; it is shown that the growth rate is the largest for $T_{ii}^P/T_{ii}^D = 5$ and the smallest for $T_{ii}^P/T_{ii}^D = 0.5$. Figure 3.4 shows the three curves between $\theta = 76^\circ$ and $\theta = 90^\circ$. It is clear that a large range of the "electrostatic" region occurs for $T_{ii}^P/T_{ii}^D = 5$; the maximum growth rate occurs at $\theta = 88^\circ$ (with $\omega_i^1 =$

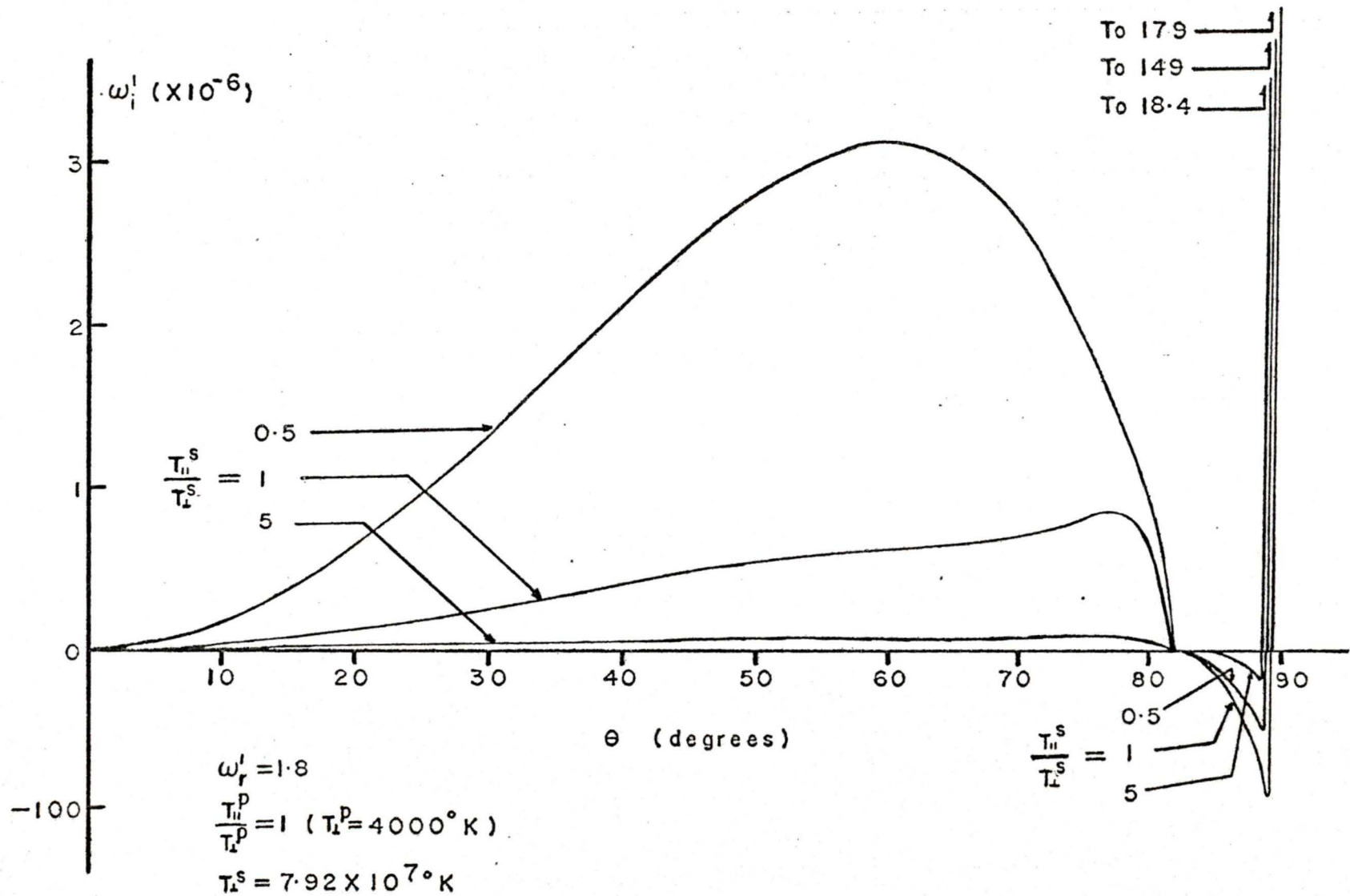


Figure 3.2 The effect of the ratio T_{ii}^s/T_e^s of the streaming electrons on the growth rate with $T_{ii}^p/T_e^p = 1$ for the plasma particles. The three ratios are $T_{ii}^s/T_e^s = 0.5, 1$ and 5 .

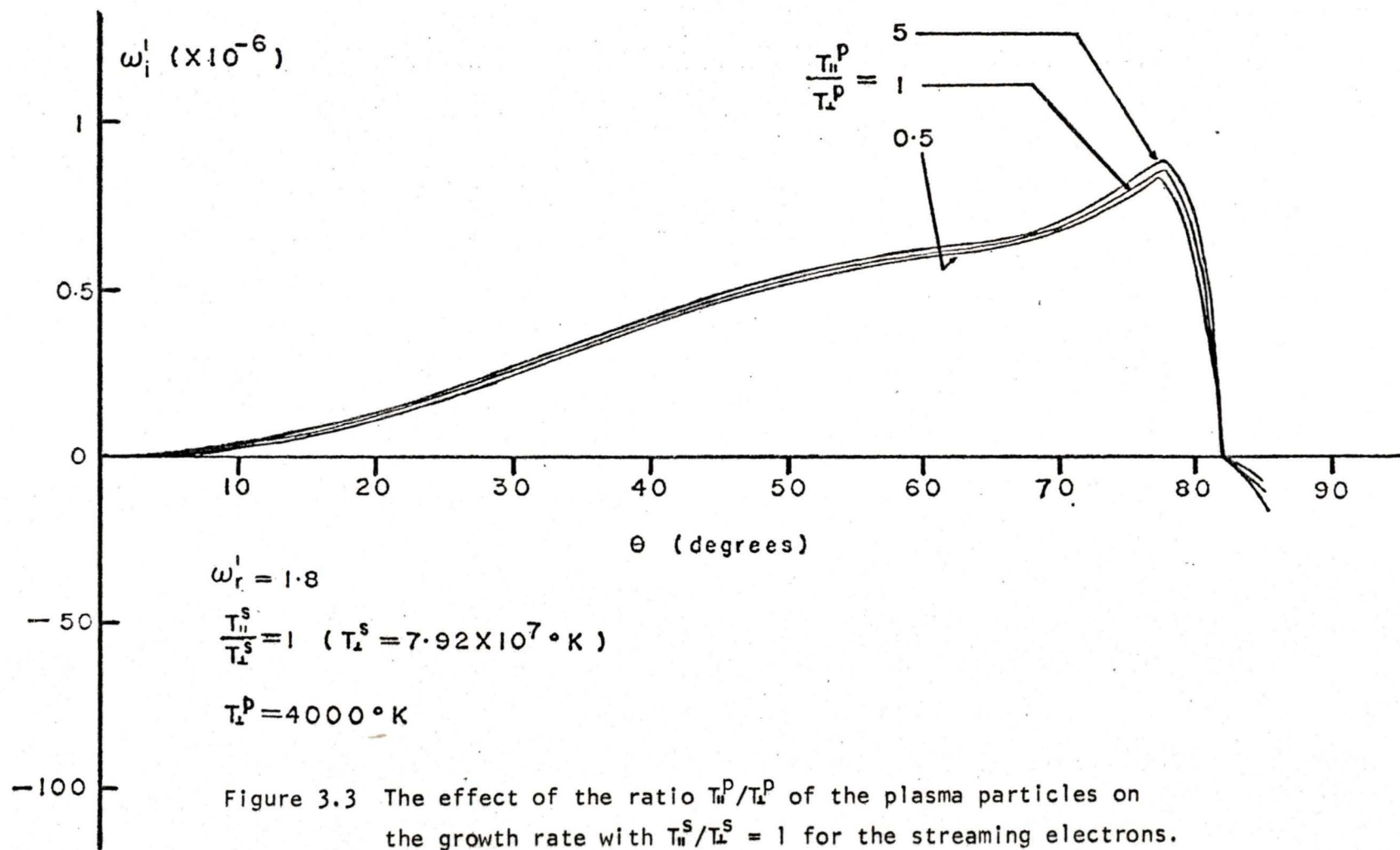


Figure 3.3 The effect of the ratio T_h^p/T_l^p of the plasma particles on the growth rate with $T_h^s/T_l^s = 1$ for the streaming electrons. The propagation angles considered are from 0° to 82° . The ratios are $T_h^p/T_l^p = 0.5, 1$ and 5 .

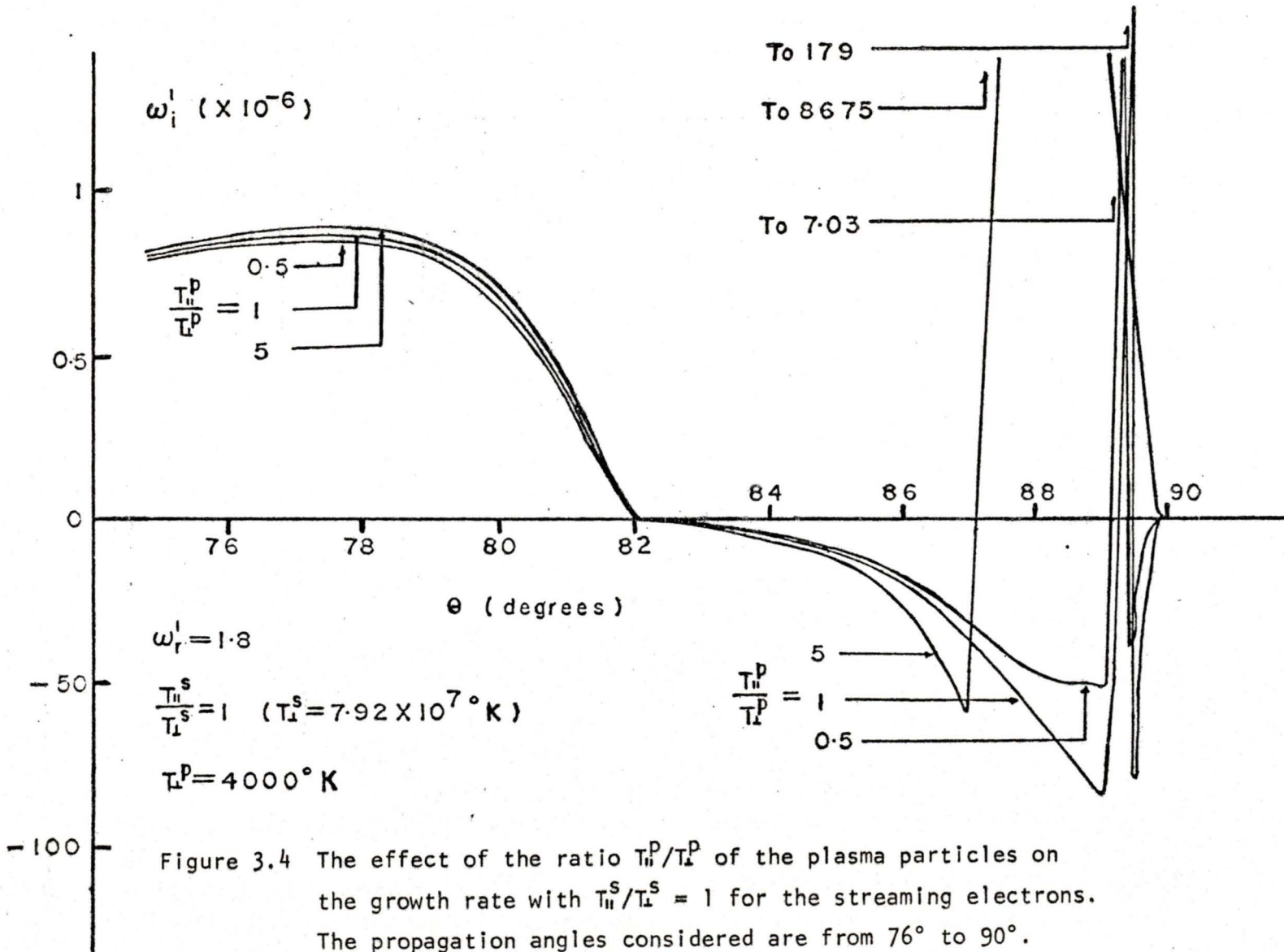


Figure 3.4 The effect of the ratio T_{ii}^p/T_L^p of the plasma particles on the growth rate with $T_{ii}^s/T_L^s = 1$ for the streaming electrons. The propagation angles considered are from 76° to 90° . The three ratios are $T_{ii}^p/T_L^p = 0.5, 1$ and 5 .

8675×10^{-6}), then $\omega_i^!$ drops to zero at 89.8° . For the cases of $T_{\parallel}^P/T_{\perp}^P = 1$ and $T_{\parallel}^P/T_{\perp}^P = 0.5$, $\omega_i^!$ reaches a maximum, drops through zero, reaching another minimum before going back to zero. Thus we can conclude from Figures 3.3 and 3.4 that both "electromagnetic" and "electrostatic" positive growth rates are greater for greater values of $T_{\parallel}^P/T_{\perp}^P$; i.e., for plasma particles with more energy in the parallel direction than in the perpendicular direction.

TABLE 3.3

Numerical values of ionospheric parameters at an altitude of
1408 km and 70.47° geomagnetic latitude

Strength of the Earth's magnetic field $B_0 = 0.33$ gauss

Number density of thermal electrons $N_e = 1.1432 \times 10^4 \text{ cm}^{-3}$

Number density of nonthermal electrons $N_s = 1 \text{ cm}^{-3}$

Number density of protons (H^+) $N_{\text{H}^+} = 4.10 \times 10^2 \text{ cm}^{-3}$

Number density of helium ions (He^+) $N_{\text{He}^+} = 2.2 \times 10^1 \text{ cm}^{-3}$

Number density of oxygen ions (O^+) $N_{\text{O}^+} = 1.1 \times 10^4 \text{ cm}^{-3}$

Mean streaming velocity of nonthermal electrons $V_s = 6 \times 10^9 \text{ cm/sec}$

Plasma frequency of electrons $\pi_e = 6.032 \times 10^6 \text{ rad/sec}$

Plasma frequency of protons (H^+) $\pi_{\text{H}^+} = 2.666 \times 10^4 \text{ rad/sec}$

Plasma frequency of helium ions (He^+) $\pi_{\text{He}^+} = 3.098 \times 10^3 \text{ rad/sec}$

Plasma frequency of oxygen ions (O^+) $\pi_{\text{O}^+} = 3.456 \times 10^4 \text{ rad/sec}$

TABLE 3.4

LHR frequencies and cyclotron frequencies using valuesfrom Table 3.3 and various values of B_0

<u>Magnetic field</u> (gauss)	<u>Gyrofrequency</u> (rad/sec)				<u>LHR frequency</u> (rad/sec)
	e	H ⁺	He ⁺	O ⁺	
0.16	2.814×10^6	1.533×10^3	3.857×10^2	9.652×10^1	18531
0.22	3.869×10^6	2.107×10^3	5.304×10^2	1.327×10^2	23665
0.28	4.925×10^6	2.682×10^3	6.751×10^2	1.689×10^2	27719
0.33	5.804×10^6	3.804×10^3	9.956×10^2	1.991×10^2	30390

3.2.3 Effect of the strength of the Earth's magnetic field B_0 on the growth rate

To investigate the influence of B_0 on the growth rate, the ionospheric parameters given in Table 3.3 are used. The number densities of H^+ , He^+ and O^+ were obtained when the satellite was at an altitude of 1408 km and 70.47° geomagnetic latitude. The fractional abundance for H^+ , He^+ and O^+ are 3.59%, 0.21% and 96.2% respectively. The wave frequency for this analysis is taken to be 6500 rad/sec. It has been observed from the ISIS 2 data that the values of B_0 range from 0.16 gauss to 0.33 gauss. Thus the four values of 0.16, 0.22, 0.28 and 0.33 gauss for B_0 were taken. The calculated values of the electron and ion gyrofrequencies are listed in Table 3.4.

Figure 3.5 is a plot of the normalized growth rate ω_i' as a function of the propagation angle θ for the four values of B_0 . The other parameters have values $T_{ii}^D/T_{ii}^D = 1$ and $T_{ii}^S/T_{ii}^S = 1.98 \times 10^4$. This figure gives the "electromagnetic" region only (with $\theta = 0^\circ$ to $\theta = 85^\circ$). It shows that the growth rate decreases when B_0 increases; $B_0 = 0.16$ gauss gives the largest value of the growth rate here. Note that the growth rate for $B_0 = 0.16$ gauss increases rapidly at the angles between $\theta = 60^\circ$ and $\theta = 80^\circ$. It reaches a maximum at $\theta = 80^\circ$. The growth rate increases quite smoothly for the other three curves of B_0 . Thus in the "electromagnetic" region, the lowest value of B_0 gives the highest value of the growth rate.

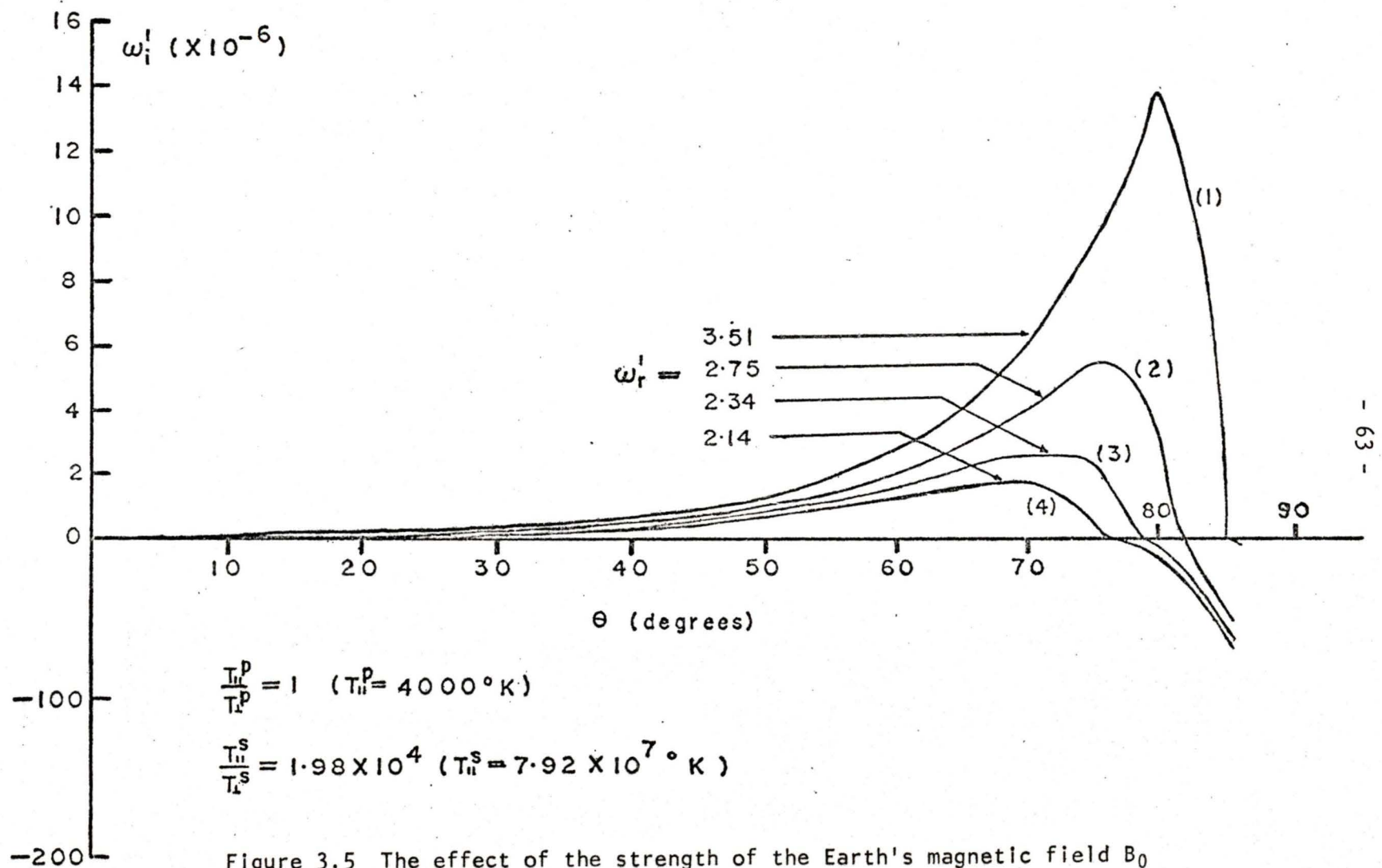


Figure 3.5 The effect of the strength of the Earth's magnetic field B_0 on the growth rate. The propagation angles considered are from 0° to 85° with (1) $B_0 = 0.16$ gauss, (2) $B_0 = 0.22$ gauss, (3) $B_0 = 0.28$ gauss and (4) $B_0 = 0.33$ gauss.

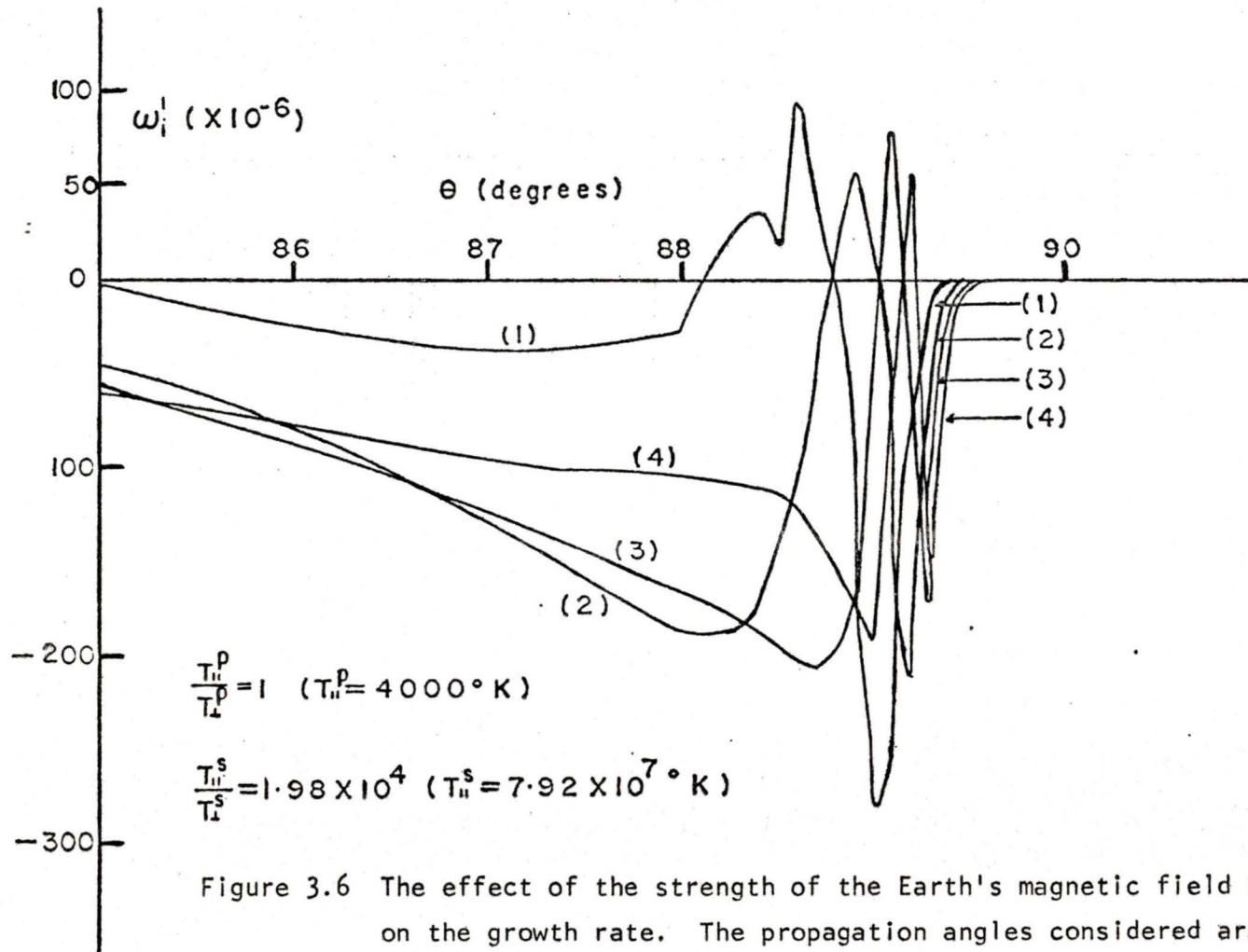


Figure 3.6 The effect of the strength of the Earth's magnetic field B_0 on the growth rate. The propagation angles considered are from 85° to 90° with (1) $B_0 = 0.16$ gauss, (2) $B_0 = 0.22$ gauss, (3) $B_0 = 0.28$ gauss and (4) $B_0 = 0.33$ gauss.

The "electrostatic" region for these four values of B_0 is shown in Figure 3.6. Two maximum positive ω_i occur in the "electrostatic" region when B_0 is 0.16 gauss. The other curves reach a maximum, decrease through zero to exhibit a negative minimum before becoming zero again. We cannot conclude from Figure 3.6 that the lowest value of B_0 gives the highest value of the growth rate in the "electrostatic" region.

TABLE 3.5

Numerical values of ionospheric parameters for the graph of
 ω_i' versus θ for the effect of ion concentration

Strength of the Earth's magnetic field $B_0 = 0.28$ gauss

Wave frequency $\omega_r = 70000$ rad/sec

Number density of nonthermal electrons $N_s = 1 \text{ cm}^{-3}$

Mean streaming velocity of nonthermal electrons $V_s = 6 \times 10^9$ cm/sec

Gyrofrequency of electrons $\Omega_e = 4.925 \times 10^6$ rad/sec

Gyrofrequency of proton (H^+) $\Omega_{\text{H}^+} = 2.682 \times 10^3$ rad/sec

Gyrofrequency of helium ions (He^+) $\Omega_{\text{He}^+} = 6.751 \times 10^2$ rad/sec

Gyrofrequency of oxygen ions (O^+) $\Omega_{\text{O}^+} = 1.689 \times 10^2$ rad/sec

TABLE 3.6

Numerical values of ion concentrations, plasma frequencies and corresponding LHR frequencies for the graph of ω_i' vs θ for the effect of ion concentration

Number Density (cm^{-3})				Plasma frequency (rad/sec)				LHR frequency (rad/sec)
e	H ⁺	He ⁺	O ⁺	e	H ⁺	He ⁺	O ⁺	
1.2624×10^4	5.7×10^2	5.4×10^1	1.2×10^4	6.339×10^6	3.143×10^4	4.854×10^3	3.619×10^4	29561
0.822×10^4	2.0×10^3	3.2×10^2	5.9×10^3	5.115×10^6	5.888×10^4	1.181×10^4	2.538×10^4	45218
0.422×10^4	2.9×10^3	7.7×10^2	5.5×10^2	3.665×10^6	7.090×10^4	1.833×10^4	7.748×10^3	59076

3.2.4 Effect of ion concentration N_k on the growth rate

Another parameter that we consider which affects the growth rate is the ion concentration. The ionospheric parameters listed in Table 3.5 are used for this investigation. Three sets of number densities from the ISIS 2 data are chosen. Their values are given in Table 3.6. The corresponding plasma frequencies of the ions and LHR frequencies are also listed in Table 3.6. Breig and Hoffman (1975) reported that the major species in the summer and winter hemispheres were O^+ and H^+ respectively. Thus our choice of the number densities will admit these two cases. In the first set of number densities, the fractional abundance of H^+ , He^+ and O^+ are 4.51%, 0.31% and 95.2% respectively. Hence O^+ is the dominant species. The fractional abundance of H^+ , He^+ and O^+ for the second set of number densities are 24.3%, 3.9% and 71.8%. In the third set of number densities, we choose H^+ to be the dominant species. The fractional abundance of H^+ , He^+ and O^+ are 68.7%, 18.2% and 13.0%. Again the other parameters have values of $T_{II}^P/T_I^P = 1$ and $T_{II}^S/T_I^S = 1.98 \times 10^4$.

The effect of ion concentration on the growth rate is shown in Figure 3.7. Note the scales are different for negative and positive values of ω_i . This figure shows that ω_i increases with increasing θ . The growth rate has the largest value when O^+ is the dominant species. The situation is reversed when H^+ is the dominant species. Note the "electrostatic" region in curve (1) disappears due to the choice of

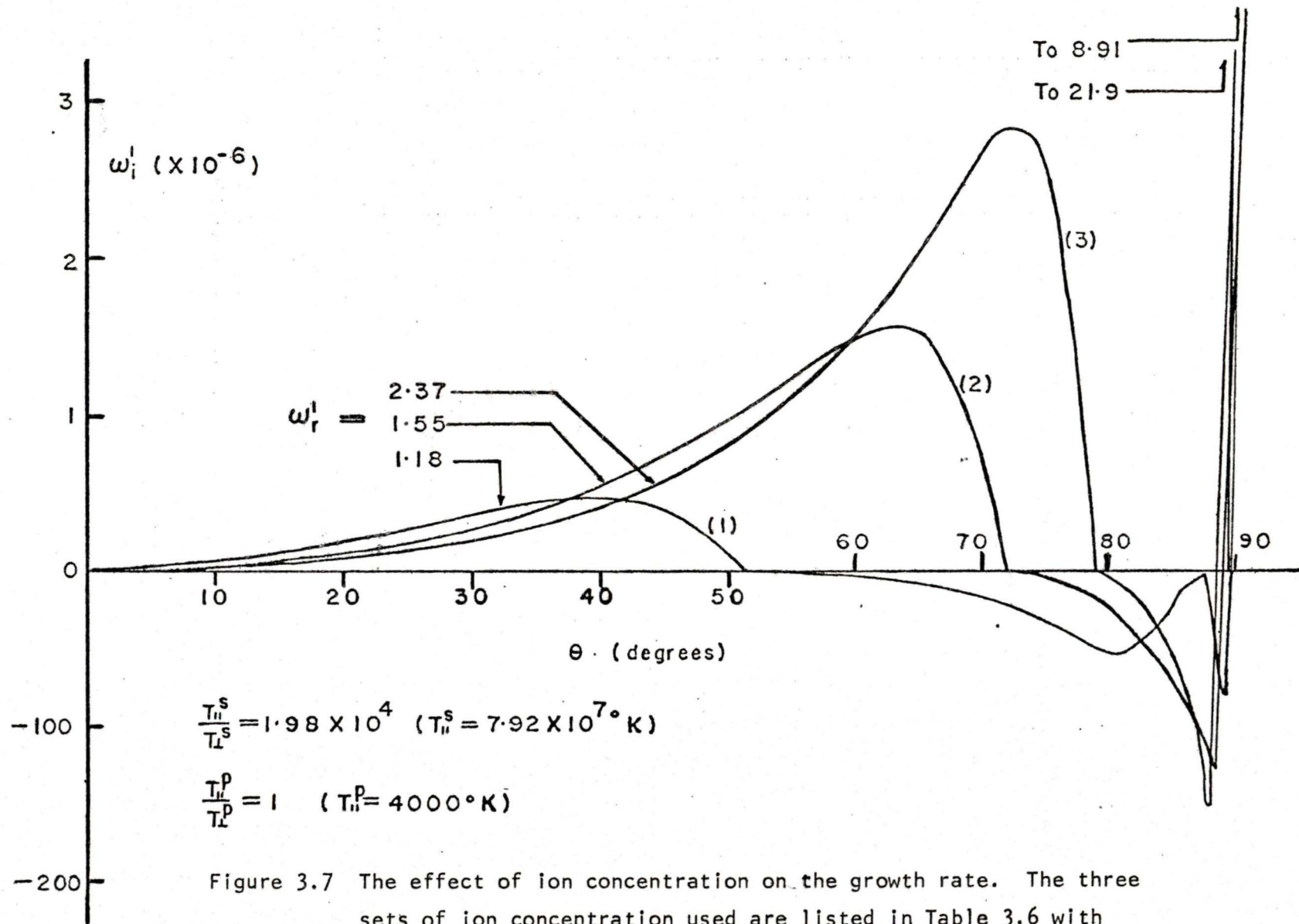


Figure 3.7 The effect of ion concentration on the growth rate. The three sets of ion concentration used are listed in Table 3.6 with (1) $N_e = 0.422 \times 10^4 \text{ cm}^{-3}$, (2) $N_e = 0.822 \times 10^4 \text{ cm}^{-3}$ and (3) $N_e = 1.2624 \times 10^4 \text{ cm}^{-3}$.

temperatures. For the other two curves, the positive ω_i in the "electrostatic" region near θ_{res} occurs over a very small interval in θ . It is shown that the maximum growth rate in the "electromagnetic" region is smaller than in the "electrostatic" region. From Figure 3.6, we conclude that the growth rate for both "electromagnetic" and "electrostatic" regions has a large value when O^+ is the dominant species, while it is small when H^+ is the dominant species.

3.3 Absorption bands near harmonics of the proton, helium and oxygen gyrofrequencies

3.3.1 Absorption bands near harmonics of the proton gyrofrequency

After the investigation of the effects of some parameters on the growth rate, a search was made to find the absorption bands at harmonics of the proton gyrofrequency. The number densities of H^+ , He^+ , O^+ and the streaming electrons listed in Table 3.3 were used. The strength of the Earth's magnetic field at an altitude of 1408 km is 0.33 gauss. The corresponding gyrofrequencies of electrons and ions are listed in Table 3.4. The calculated value for the LHR frequency is 30390 rad/sec (about 4.84 kHz). The velocity of the streaming electrons is taken to be 6×10^9 cm/sec, which corresponds to a kinetic energy of 10 keV. From chapter 2, we note that the prediction of absorption bands was made for a warm plasma. Thus an attempt is first made to find out for which temperature values for the plasma electrons and ions and streaming electrons the absorption bands at harmonics of the proton gyrofrequency may appear. Isotropic temperatures of both plasma electrons and ions and streaming electrons ($T_{ii}^D/T_e^D = 1$ and $T_{ii}^S/T_e^S = 1$) were first considered but no absorption bands could be seen. Then anisotropic temperatures were considered. It has been found that with $T_{ii}^D/T_e^D > 1$ and $T_{ii}^S/T_e^S > 1$, no absorption bands were seen. Thus another possibility is $T_{ii}^D/T_e^D < 1$ and $T_{ii}^S/T_e^S < 1$. As indicated by Oya (1971) more energy is absorbed by the electrons in the perpendicular direction than in the parallel direction, so the consideration

of $T_{ii}^P/T_{ii}^D < 1$ and $T_{ii}^S/T_{ii}^D < 1$ is reasonable. A search has been made and it is found that when $T_{ii}^P/T_{ii}^D = 0.610$ and $T_{ii}^S/T_{ii}^D = 7.98 \times 10^{-3}$, the absorption bands near harmonics of the proton gyrofrequency appear in the "electrostatic" region. The wave frequency we considered is from $\omega_r' = 0.90$ (ω_r' is the normalized wave frequency, i.e. $\omega_r' = \omega_r/\omega_{LH}$) to $\omega_r' = 2.50$. The resonance angle for this case is about 89.30° . Thus the "electrostatic" region we consider ($\theta = 88.65^\circ$ to $\theta = 89.15^\circ$) is for angles near the resonance cone. Six graphs of ω_r' as a function of power absorption per unit volume by charged particles in the "electrostatic" region are plotted. For all graphs, the scale on the left-hand side is for the normalized wave frequency ω_r' , while the one on the right-hand side is for the proton gyrofrequency. Note the power absorption P_a is plotted on a log scale.

Figure 3.8 shows ω_r' versus power absorption P_a with $\theta = 88.65^\circ$. The first absorption band occurs at $16.1 \Omega_H^+$. Then the other absorption bands in the figure appear at intervals spaced at integer multiples of the proton gyrofrequency. The absorption bands disappear at some values of wave frequencies. Note that below the first absorption band, the peaks go to the left-hand side, indicating less absorption occurs in this region. Figure 3.9 is another plot of ω_r' versus P_a with $\theta = 88.85^\circ$. Note that the first absorption band occurs at $13.1 \Omega_H^+$ and the subsequent absorption bands at intervals spaced at integer multiples of the proton gyrofrequency. It is observed that the top peak pointing to the left shifts from $\omega_r' = 1.60$ to $\omega_r' = 1.29$.

Figure 3.10 shows that absorption bands near harmonics of the helium gyrofrequency also appear. They occur at frequencies below the absorption bands near the harmonics of the proton gyrofrequency. Here the propagation angle is 88.90° and the first absorption band near harmonics of the proton gyrofrequency is at $12.1 \Omega_H^+$. Figure 3.11 is a plot with $\theta = 89.00^\circ$. It is observed that more absorption bands near harmonics of the helium gyrofrequency appear. Note that between $11 \Omega_H^+$ and $12 \Omega_H^+$ there are four absorption bands near harmonics of the helium gyrofrequency. Figure 3.12 is another plot of ω_r' versus P_a . Note that the top peak pointing to the left shifts below $\omega_r' = 1.00$. More absorption bands near harmonics of the helium gyrofrequency are observed. Figure 3.13 shows ω_r' versus P_a with $\theta = 89.15^\circ$. It has been observed from these figures that with increasing θ , the number of absorption bands near harmonics of the helium gyrofrequency also increase. They occur below $12 \Omega_H^+$ and the top peak pointing to the left. The power absorption goes negative (i.e. the plasma wave absorbs energy) at some values of wave frequencies.

A graph of the normalized transition frequency ω_T' versus the propagation angle is plotted. The term "transition frequency" (designated as ω_T) represents the wave frequency above which the absorption bands appear. Figure 3.14 shows ω_T' versus propagation angle θ . It shows that with increasing θ , ω_T' decreases.

It has also been found that with decreasing V_s , P_a decreases. It is clear that other parameters such as B_0 and N_k may also affect the absorption bands at harmonics of the proton gyrofrequency. The important conditions for the appearance of the absorption bands are temperature of the ions and the propagation angle.

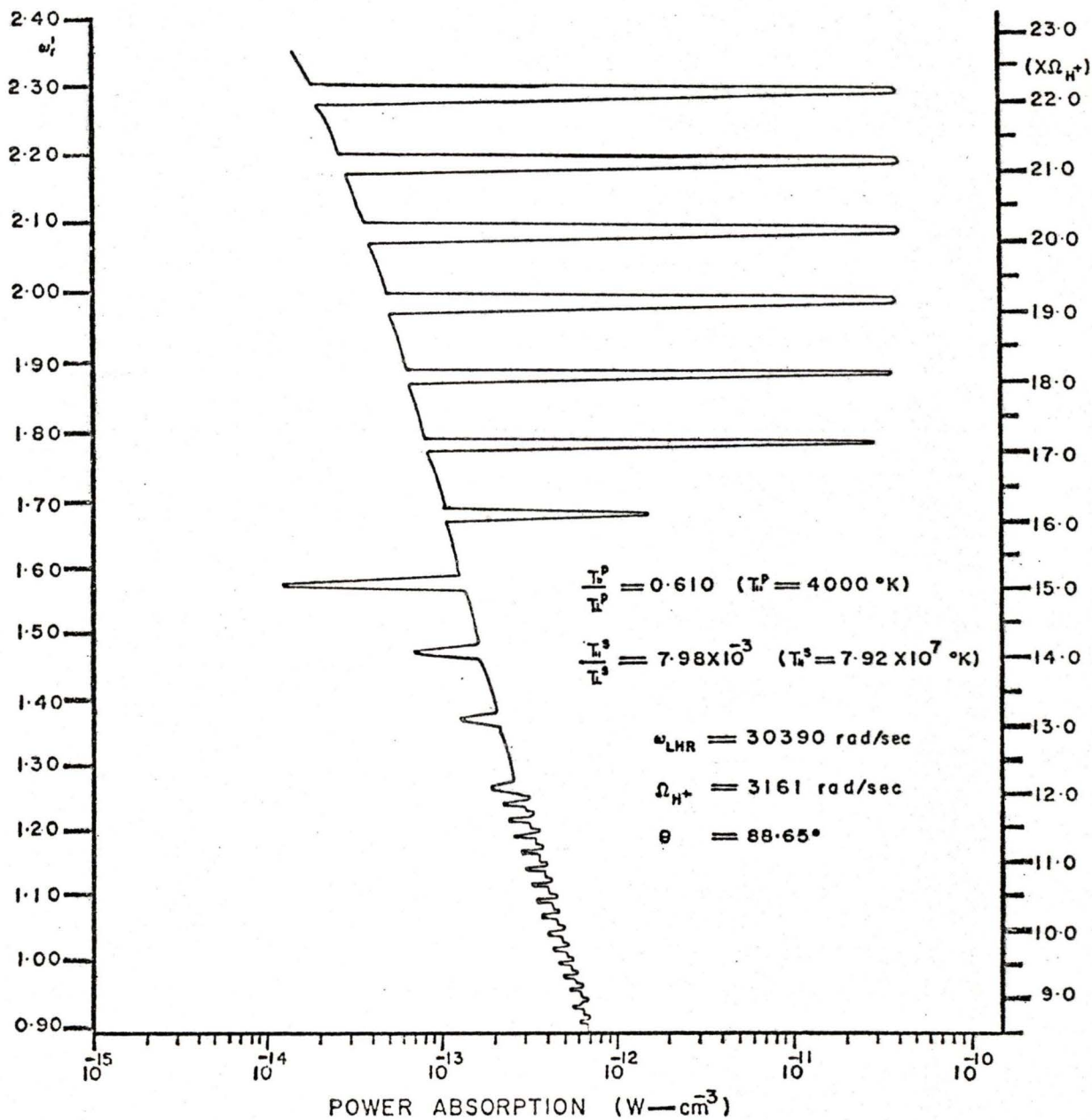


Figure 3.8 Normalized wave frequency versus power absorption per unit volume by charged particles for $\theta = 88.65^\circ$. Absorption bands appear near harmonics of the proton gyrofrequency.

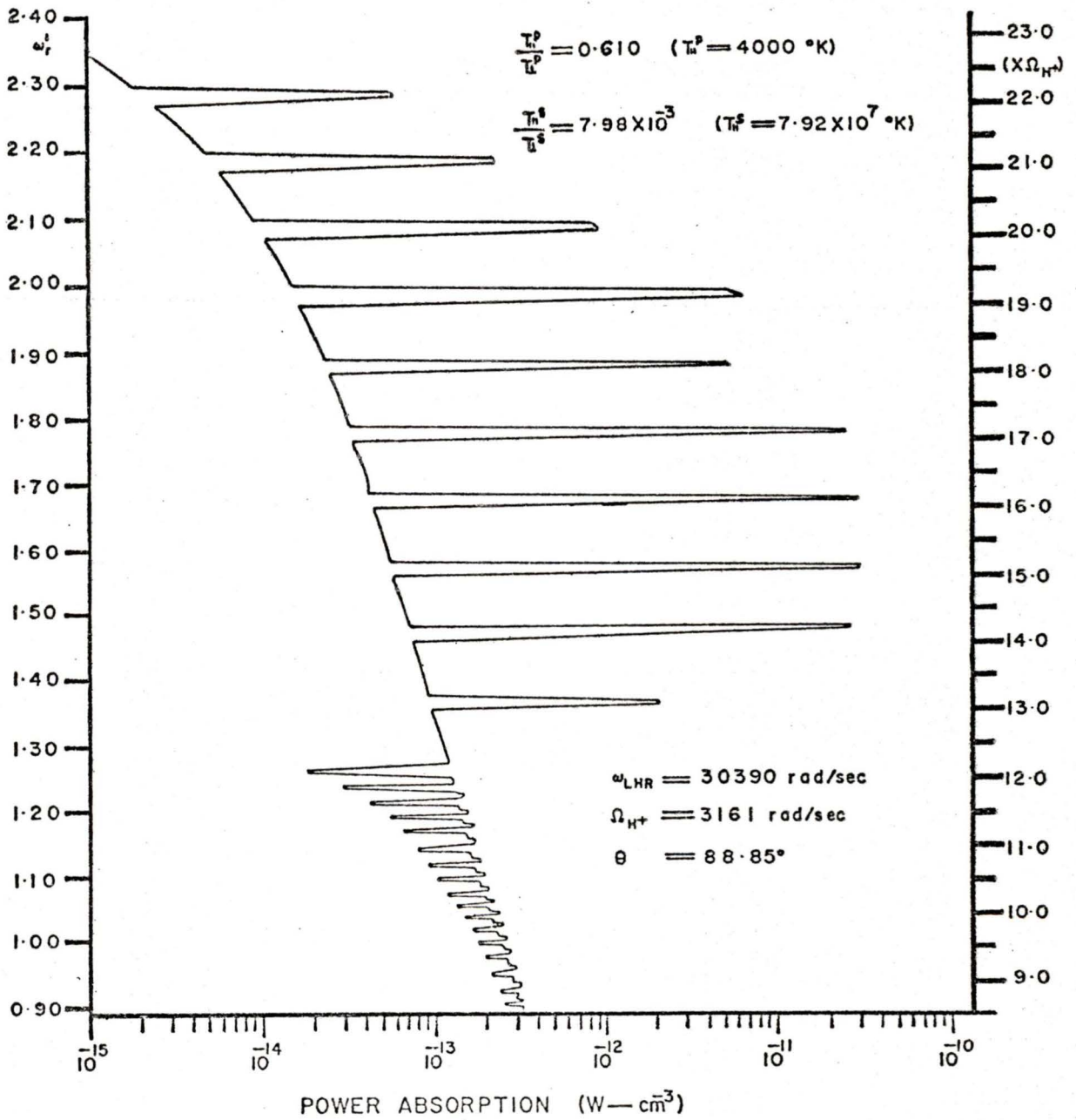


Figure 3.9 Normalized wave frequency versus power absorption per unit volume by charged particles for $\theta = 88.85^\circ$. Absorption bands appear near harmonics of the proton gyrofrequency.

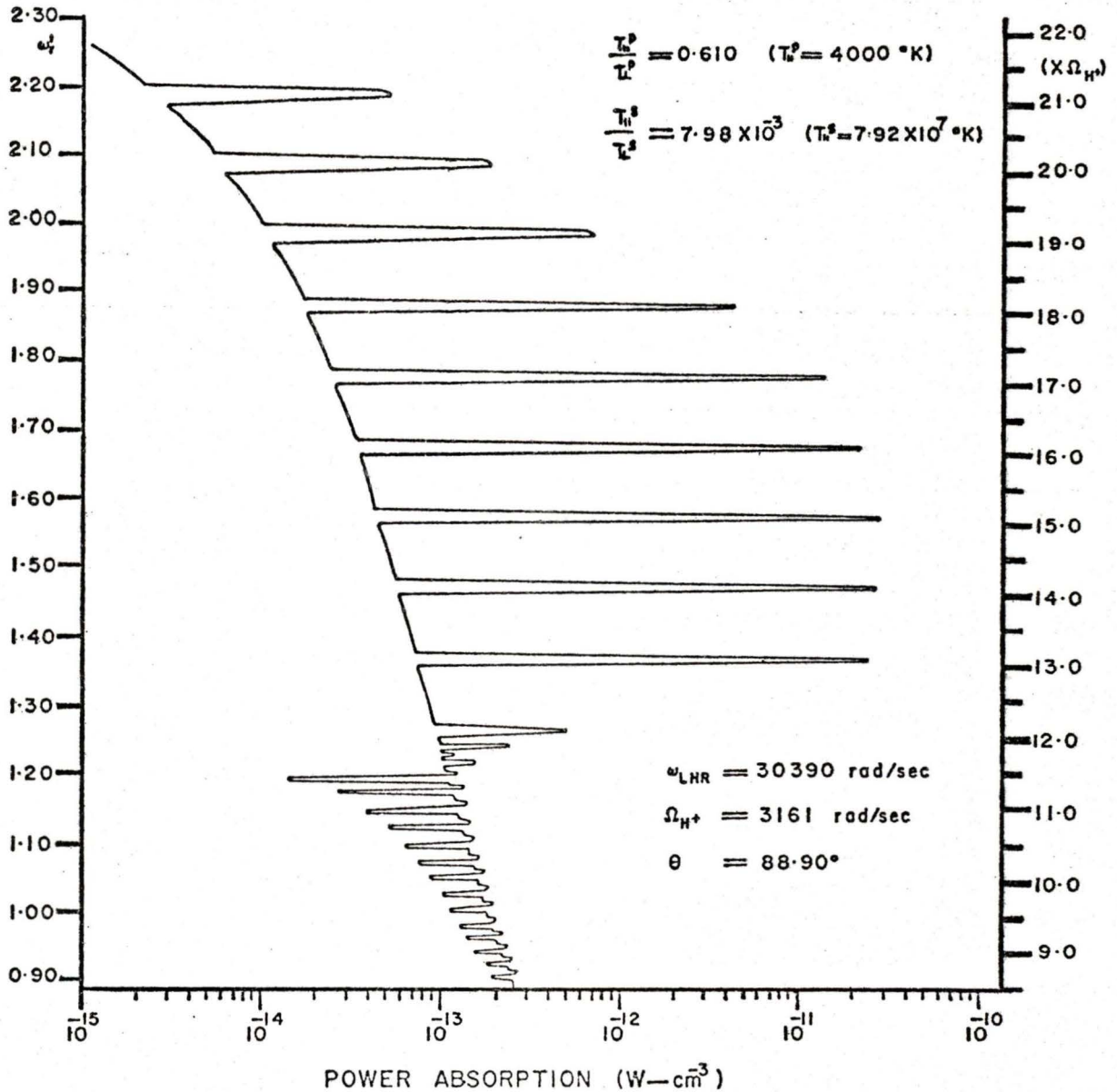


Figure 3.10 Normalized wave frequency versus power absorption per unit volume by charged particles for $\theta = 88.90^\circ$. Absorption bands near harmonics of the helium gyrofrequency have appeared.

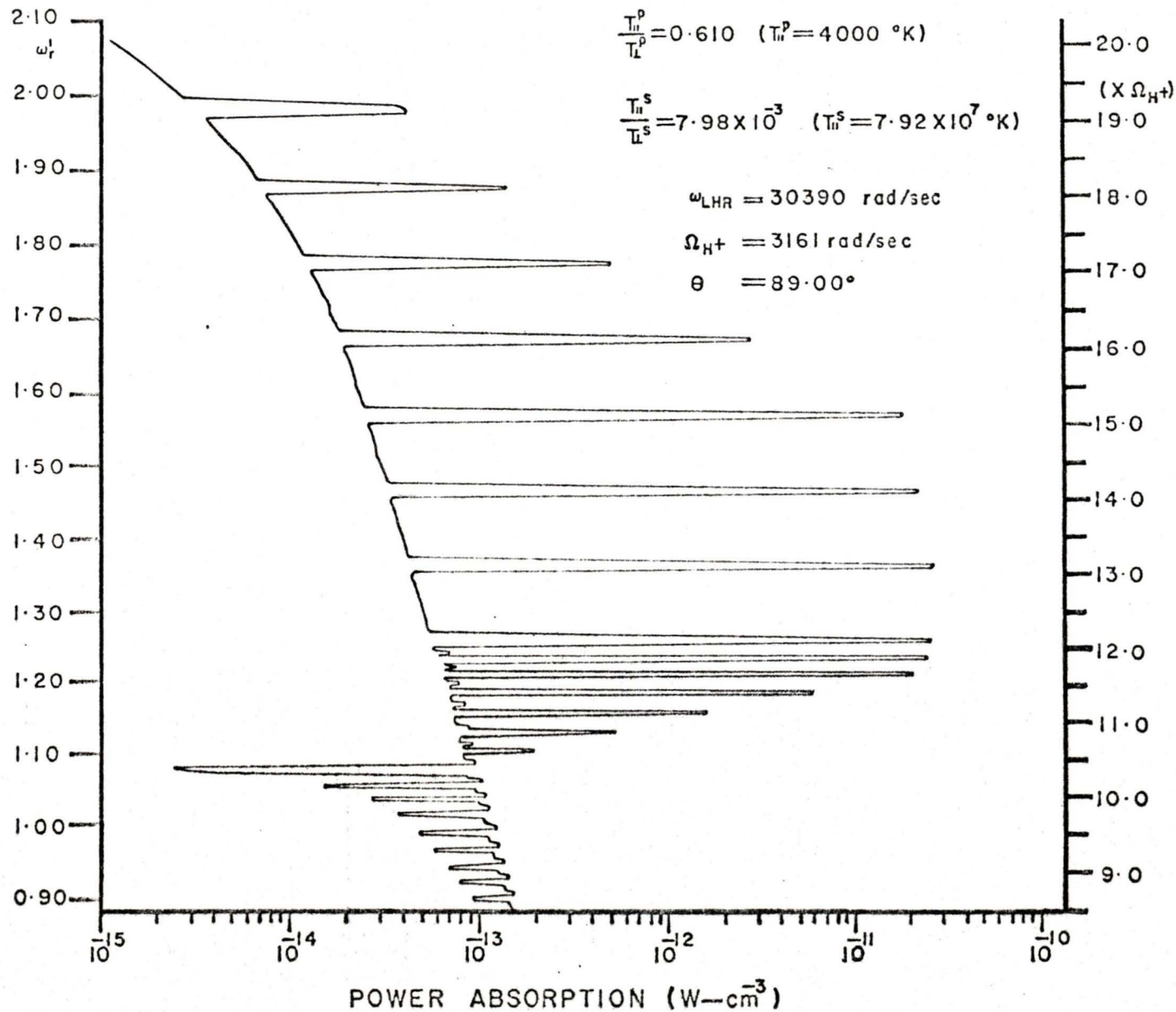


Figure 3.11 Normalized wave frequency versus power absorption per unit volume by charged particles for $\theta = 89.00^\circ$. Absorption bands near harmonics of the helium gyrofrequency are observed.

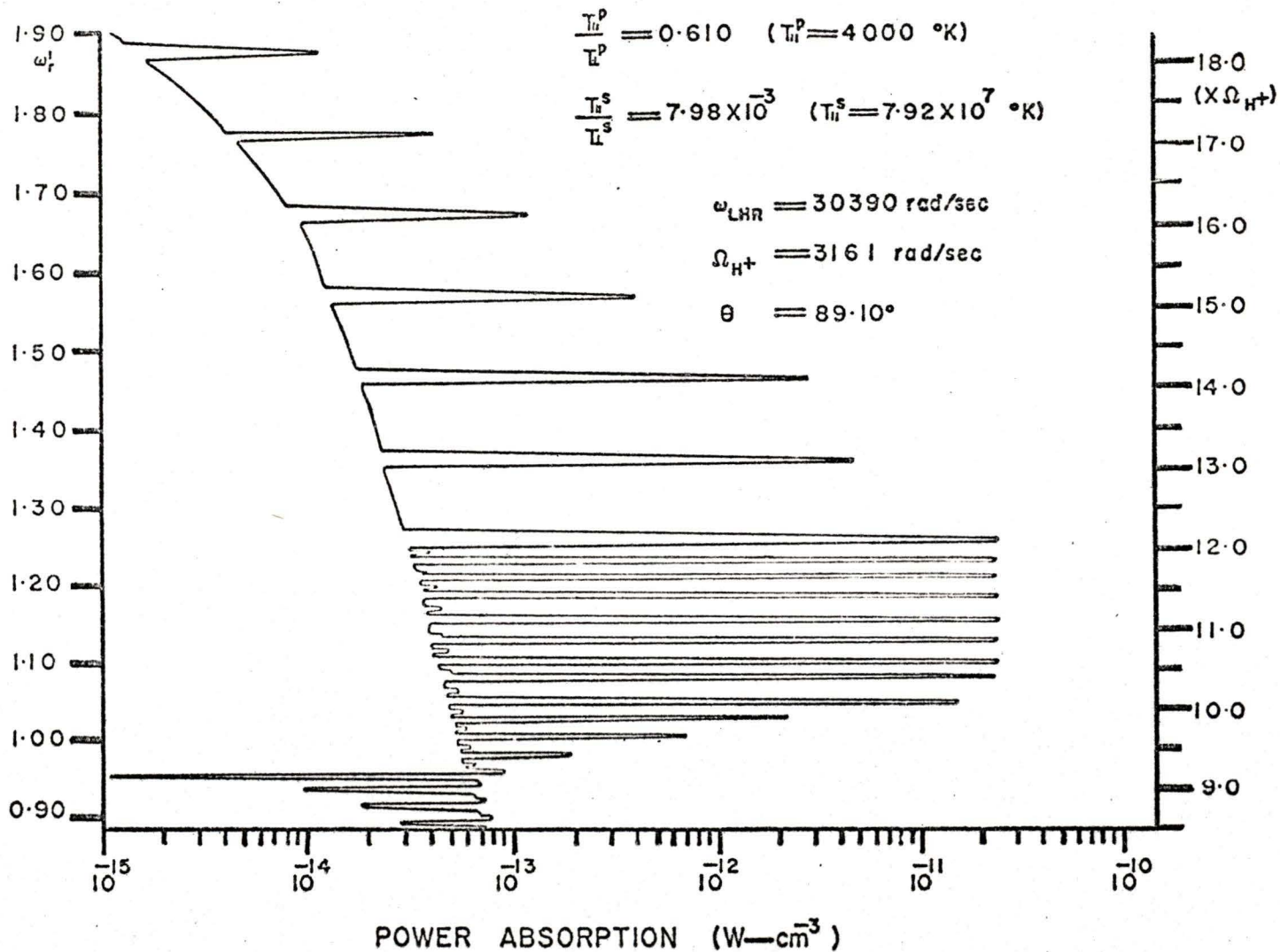


Figure 3.12 Normalized wave frequency versus power absorption per unit volume by charged particles for $\theta = 89.10^\circ$. Absorption bands near harmonics of the helium gyrofrequency are observed.

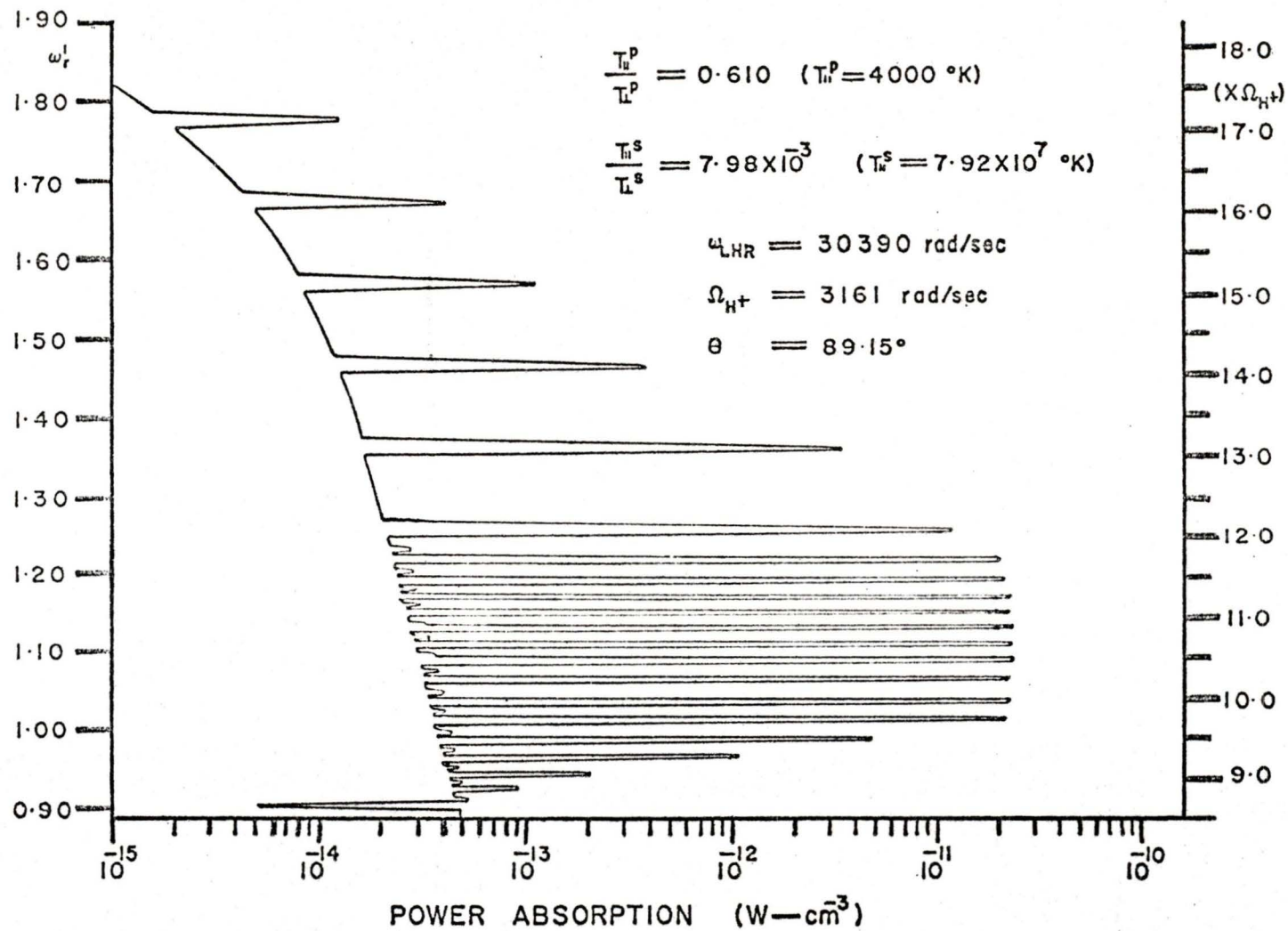


Figure 3.13 Normalized wave frequency versus power absorption per unit volume by charged particles for $\theta = 89.15^\circ$. Absorption bands near harmonics of the helium gyrofrequency are observed.

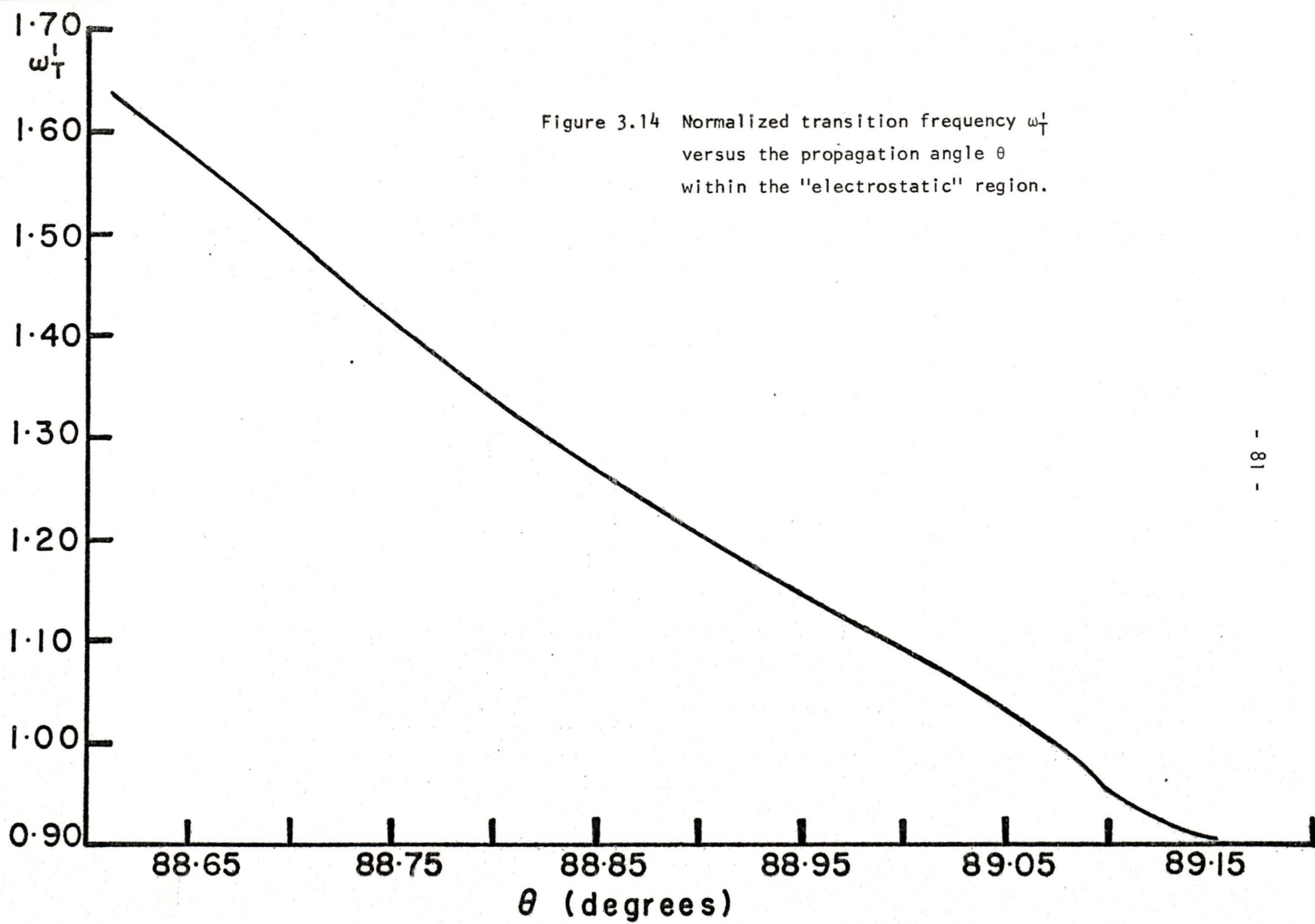


Figure 3.14 Normalized transition frequency ω_T^1 versus the propagation angle θ within the "electrostatic" region.

3.3.2 Absorption bands near harmonics of the helium gyrofrequency

As mentioned in chapter 1 phenomena at harmonics of the helium gyrofrequency were also reported (i.e. Horita and Friesen, 1975; Horita *et al.*, 1976), so an attempt was made to find the absorption bands at harmonics of the helium gyrofrequency. The appearance of the absorption bands at harmonics of the helium gyrofrequency below $12 \Omega_{H^+}$ in the previous section gives rise to the possibility of the occurrence of the absorption bands at helium frequencies. Thus a search was made to find the conditions for which such absorption bands may appear. The number densities for the ions and streaming electrons as listed in Table 3.3 were used. The velocity of the streaming electrons and B_0 were taken to be the same as stated in the previous section. Anisotropic temperatures for the ions and streaming electrons were considered. It has been found that when $\tau_{ii}^P/\tau_e^P = 0.476$ and $\tau_{ii}^S/\tau_e^S = 7.98 \times 10^{-3}$ the absorption bands near harmonics of helium gyrofrequency appear.

Figure 3.5 shows ω_p' versus power absorption with $\theta = 89.17^\circ$. The scale on the left-hand side is the normalized wave frequency ω_p' . There are two scales on the right-hand side. The one on the outside is for the multiples of the proton gyrofrequency. The one on the inside is for the multiples of the helium gyrofrequency. Again P_a is plotted on a log scale. The first few absorption bands occur at $35.25 \Omega_{H^+}$, $36.25 \Omega_{He^+}$ and $37.25 \Omega_{He^+}$. Then there is another group of absorption bands spaced at the helium gyrofrequency which occurs

at $39.76 \Omega_{\text{He}^+}$, $40.80 \Omega_{\text{He}^+}$, $41.80 \Omega_{\text{He}^+}$, $42.80 \Omega_{\text{He}^+}$, $43.80 \Omega_{\text{He}^+}$ and $44.80 \Omega_{\text{He}^+}$. It is interesting to note that there is another group of absorption bands exactly at harmonics of the helium gyrofrequency (i.e. $46 \Omega_{\text{He}^+}$, $47 \Omega_{\text{He}^+}$ and $48 \Omega_{\text{He}^+}$). Then the rest of the absorption bands occur near harmonics of the helium gyrofrequency in different groups. In general, the absorption bands near harmonics of the helium gyrofrequency occur in a group. These phenomena have been reported by Horita and Friesen (1975). Attention should be made to the absorption band which has a maximum value of P_a at $49.15 \Omega_{\text{He}^+}$. After this group of absorption bands the value of P_a starts to decrease. Below the first absorption band, the power absorption goes to the left. Again the power absorption becomes negative at some values of wave frequencies.

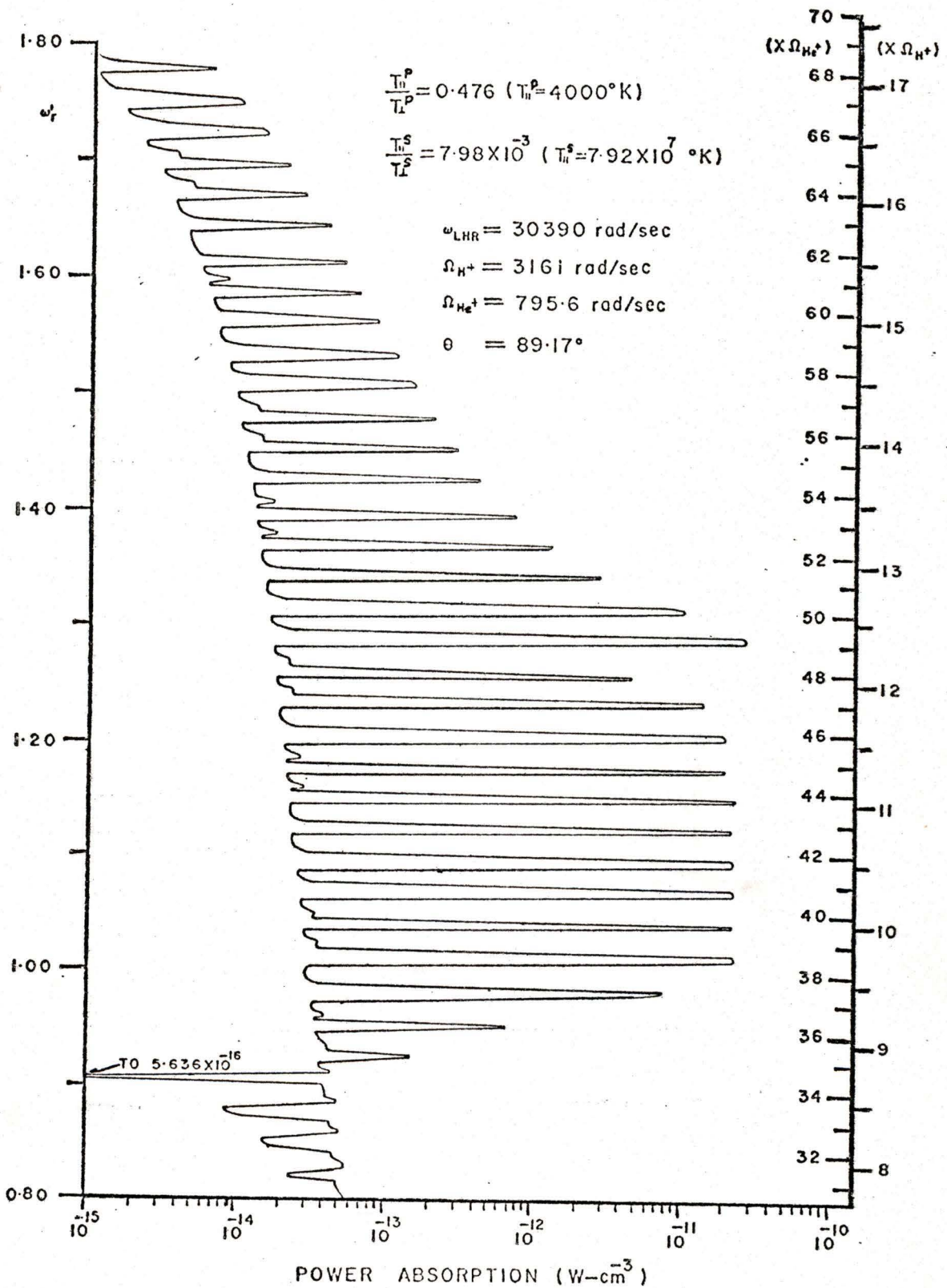


Figure 3.15 Normalized wave frequency versus power absorption per unit volume by charged particles. Absorption bands near harmonics of the helium gyrofrequency are shown.

3.3.3 Absorption bands near harmonics of the oxygen gyrofrequency

Stéfant (1970) reported that phenomena associated with harmonics of a positive ion (particularly O^+) gyrofrequency has been observed. This observation suggests the possibility of the occurrence of absorption bands at the harmonics of the oxygen gyrofrequency. A search was first made by using the number densities listed in Table 3.3, but no absorption bands were found. Thus the ionospheric parameters listed in Table 3.1 were used. The calculated value of the LHR frequency is 30580 rad/sec (about 4.87 kHz). The corresponding gyrofrequencies of the ions and electrons are listed in Table 3.2. When $T_{ii}^P/T_{ie}^P = 0.733$ and $T_{ii}^S/T_{ie}^S = 7.98 \times 10^{-3}$, absorption bands near harmonics of the oxygen gyrofrequency occur. The propagation angle for this case is 89.04° . Figures 3.16 to 3.18 are graphs of $\omega_r^!$ versus the power absorption by charged particles. The scale on the left hand side is $\omega_r^!$. There are two scales on the right; the one on the outside is for the proton gyrofrequency, while the one on the inside is for the oxygen gyrofrequency.

Figure 3.16 shows $\omega_r^!$ versus P_a from $\omega_r^! = 0.97$ to $\omega_r^! = 1.23$. At about $\omega_r^! = 1.1$ P_a goes to 7.300×10^{-16} W-cm $^{-3}$. Below $\omega_r^! = 1.01$ there are no absorption bands, while above this value absorption bands appear. The first absorption band is at $157.7 \Omega_{O^+}$, then the others are spaced at integer multiples of the oxygen gyrofrequency up to $169.7 \Omega_{O^+}$. Starting at $170.5 \Omega_{O^+}$, there is another group of absorption bands.

Figures 3.17 and 3.18 are the plots for $\omega_r' = 1.24$ to $\omega_r' = 1.50$ and $\omega_r' = 1.51$ to $\omega_r' = 1.73$. Note that with increasing ω_r' the magnitude of P_a increases from its first harmonics to have a maximum, then decreases at about $218 \Omega_0+$. The magnitude of P_a increases again until it reaches $222 \Omega_0+$. At $223 \Omega_0+$ P_a has a minimum after which it increases to have a maximum and then decreases again. It has been observed that starting at $223 \Omega_0+$, the absorption bands occur exactly at harmonics of the oxygen gyrofrequency (i.e. $223 \Omega_0+$, $224 \Omega_0+$, $225 \Omega_0+$ etc.). This feature occurs up to $244 \Omega_0+$. Then the rest of the absorption bands occur near harmonics of the oxygen gyrofrequency in different P groups. With ion temperatures other than $T_i^P/T_e^P = 0.733$, no absorption bands at harmonics of oxygen gyrofrequency were found. Thus the absorption bands are highly dependent on the ion temperatures.

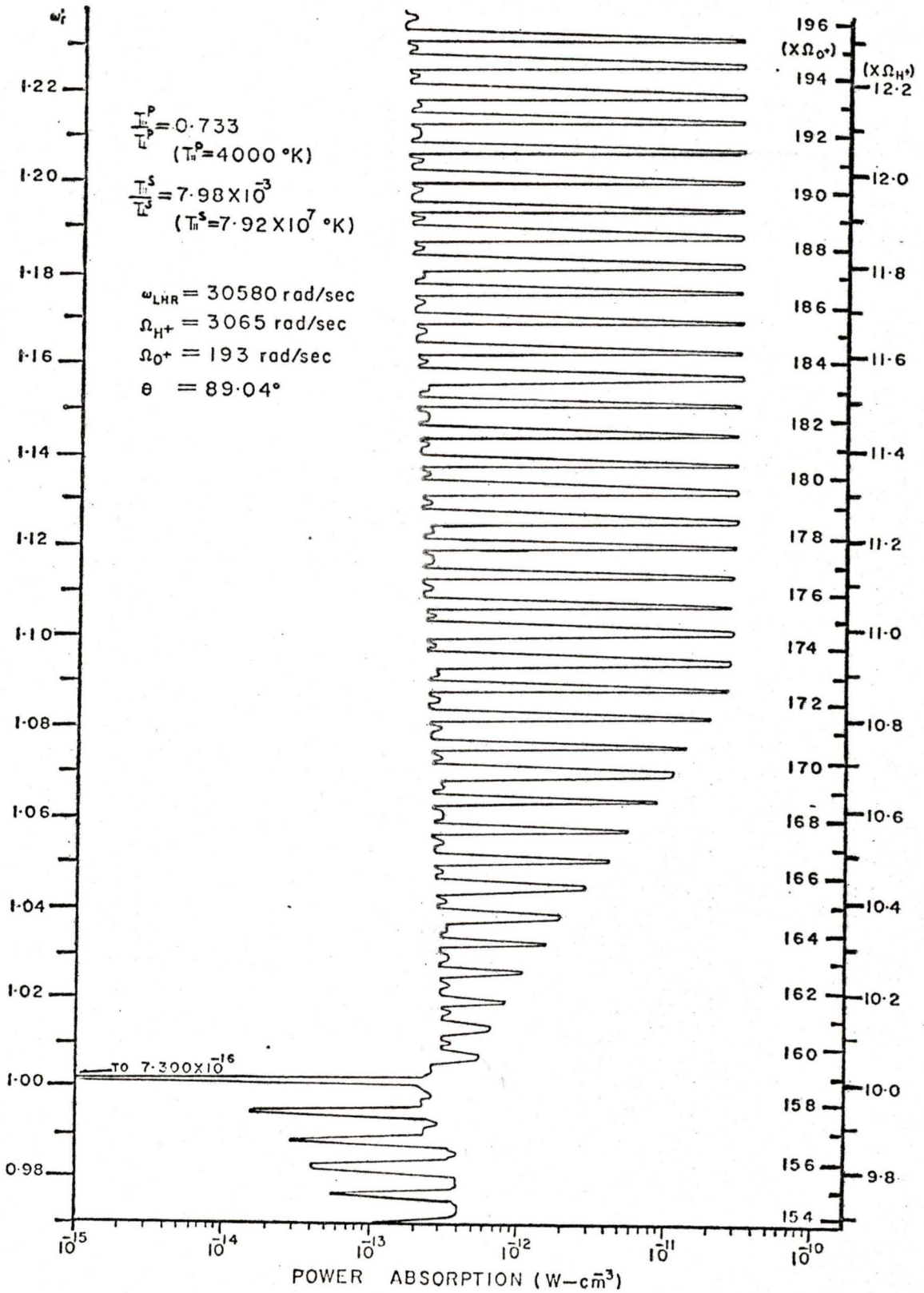


Figure 3.16 Normalized wave frequency versus power absorption per unit volume by charged particles for $\omega_r' = 0.97$ to $\omega_r' = 1.23$. Absorption bands near harmonics of the oxygen gyrofrequency are shown.

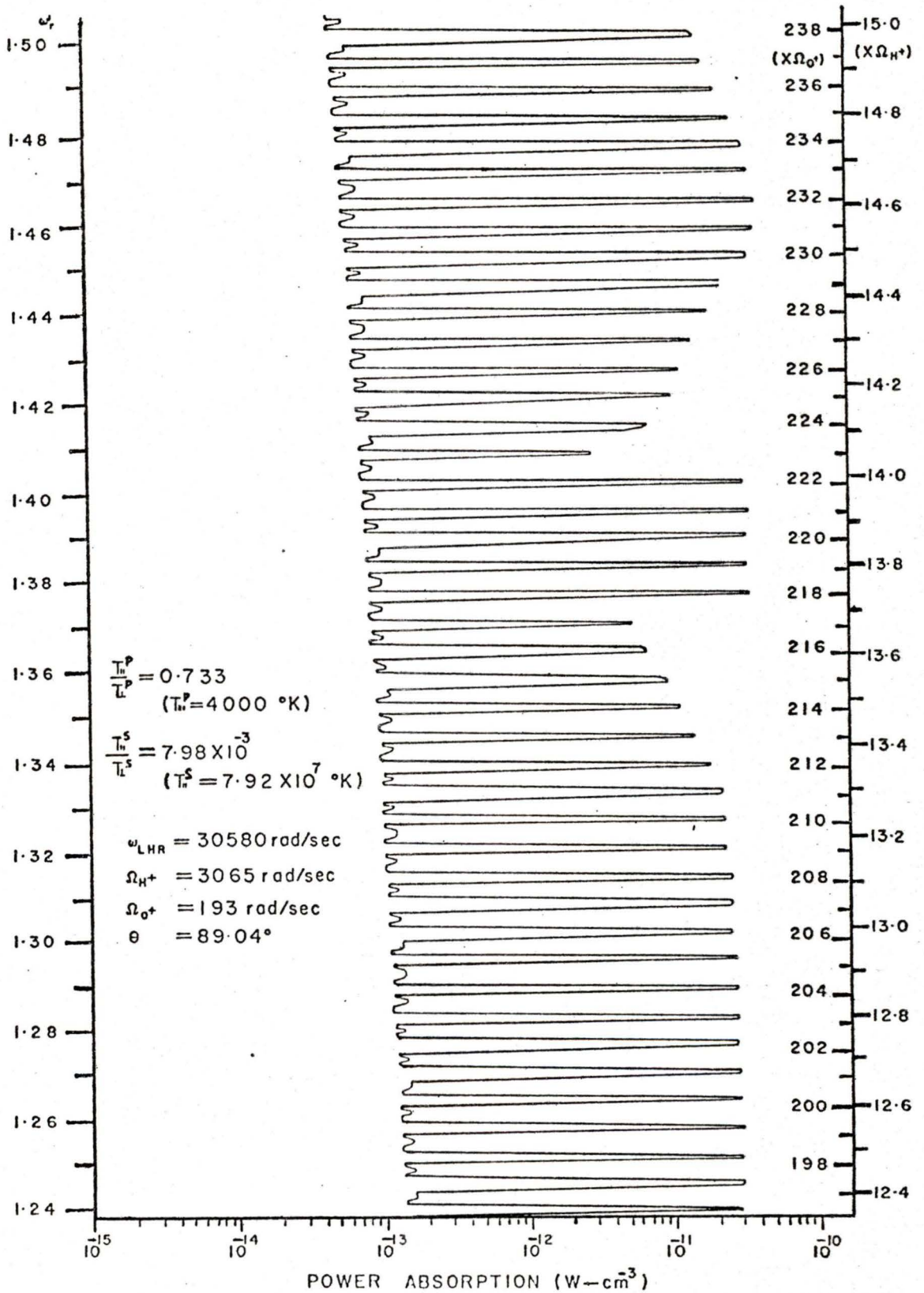


Figure 3.17 Normalized wave frequency versus power absorption per unit volume by charged particles for $\omega_r^i = 1.24$ to $\omega_r^i = 1.50$. Absorption bands near harmonics of the oxygen gyrofrequency are shown.

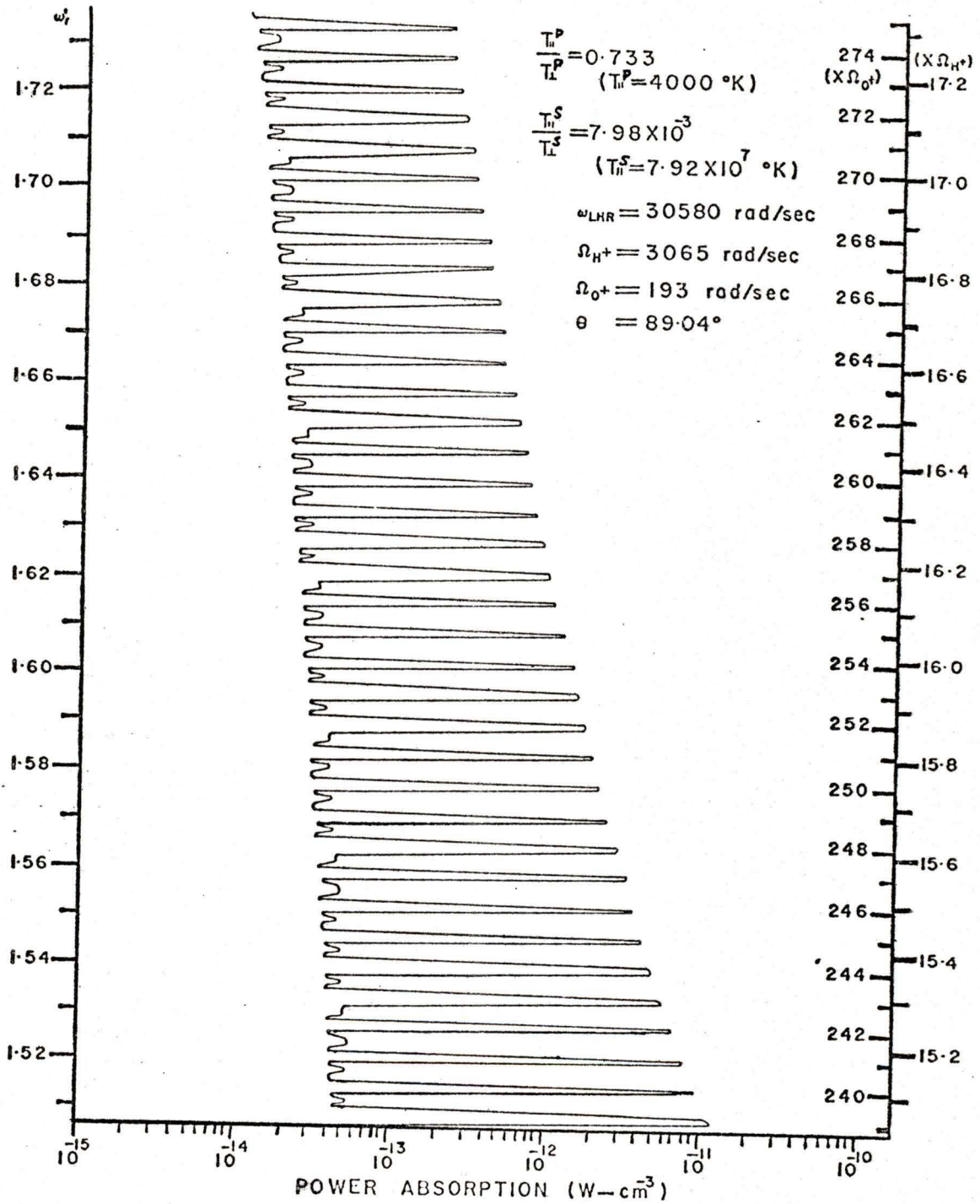


Figure 3.18 Normalized wave frequency versus power absorption per unit volume by charged particles for $\omega_r^i = 1.51$ to $\omega_r^i = 1.73$. Absorption bands near harmonics of oxygen gyrofrequency are shown.

CHAPTER 4

DISCUSSION OF RESULTS

4.1 Comparison of theory with satellite observations

As mentioned in chapter 1, section 1.3, observations of phenomena related to the proton, helium or oxygen gyrofrequency from satellites and rockets were reported by several investigators. Mosier and Gurnett (1969) and Gurnett and Mosier (1969) reported that the proton gyrofrequency harmonics were generally within the attenuation bands in the electrostatic noise bands on the Javelin 8.64 sounding rocket. The Landau instability mechanism as developed in this thesis is relevant to these electrostatic noise bands since it leads to the gyrofrequency harmonics within the attenuation band. This theory allows an investigation in both the electromagnetic and electrostatic waves. Thus this theory can provide an explanation for the V-shaped VLF hiss events from the Injun 5 satellite which are observed in both the electric and magnetic field spectrograms. Absorption bands within saucers, as reported by Klumpar (1975), may also be explained in terms of the Landau instability theory. He suggested that the absorption bands were evidence for energy transfer from the waves to the particles. This transfer is exactly what occurs in the Landau instability mechanism as stated in this thesis.

Shaw and Gurnett (1971) reported that harmonic bands observed on a whistler were not related to an ion gyrofrequency at the position of the satellite but were produced by multiple lightning discharges. Paymar (1972) observed phenomena called banded whistlers on OGO 4 satellite spectrograms. He explained the phenomena in terms of a field-aligned slab of enhanced ionization. But a paper by Horita and Friesen (1975) reported whistlers which were enhanced or attenuated at harmonics of the proton or helium gyrofrequency. They showed that the proton gyrofrequency was usually at some value other than the local value in the immediate vicinity of the satellite. They reported that some observed values were greater than the local values while others were smaller than the local values. This suggested that the mechanism yielding the enhancement or attenuation took place at locations beneath or above the satellite. Thus if the Landau instability mechanism is relevant, enhancement and attenuation of the whistler correspond to energy transfer to the wave and to the particles.

Auroral hiss as downgoing waves are observed by Gurnett and Frank (1972). If we consider the generation mechanism for auroral hiss to be the Landau instability process, then any proton gyrofrequency attenuation bands observed should yield calculated values for the proton gyrofrequency lower than the local values. Such attenuation bands have been found and discussed in chapter 1, section 1.3 with examples (Figure 1.2 and Figure 1.3).

Absorption bands at harmonics of the helium and oxygen gyrofrequencies are also found. These results correspond to the observations by Stéfant (1970).

4.2 Discussion of the influence of temperature

Anisotropic temperatures are assumed in calculations for the growth rate and in finding the absorption bands at harmonics of the ion gyrofrequencies. The dependence of temperature on the whistler-mode waves has been examined by Willis (1975). Oya (1975) reported that more energy is absorbed by the electrons in the perpendicular than in the parallel direction. Indeed anisotropic temperatures for ions is the main factor for the occurrence of the absorption bands.

Growth rate curves are drawn separately for the "electromagnetic" and "electrostatic" regions for the effect of $T_{\perp}^P/T_{\parallel}^P$ and the effect of the Earth's magnetic field because the "electrostatic" regions in both cases show complicated results. The consideration of the growth rate versus θ for different parameters enable investigators to understand the effects of these parameters on the absorption bands.

For the absorption bands at harmonics of ion gyrofrequencies, different ratios of $T_{\perp}^P/T_{\parallel}^P$ are found for different harmonics. Since the absorption bands are a temperature effect, it is not surprising that different absorption bands have different $T_{\perp}^P/T_{\parallel}^P$. $T_{\perp}^P/T_{\parallel}^P$ were found to be the most important factor for the occurrence of the absorption bands. It is due to the power absorption by the particles in the plasma from the wave. This dependence of plasma temperature has been investigated by Akasofu and Chapman (1972).

The "electrostatic" region has been examined for the absorption bands near harmonics of the proton gyrofrequency. With increasing wave frequency, the power absorption becomes less and finally goes negative at some wave frequency. Absorption bands are at integer multiples which correspond to the observations from satellites. Absorption bands near harmonics of the helium gyrofrequency appear in some of the diagrams of the absorption bands near harmonics of the proton gyrofrequency. Choosing different values of θ and temperature ratio T_{He}^P/T_{H}^P , more absorption bands near harmonics of the helium gyrofrequency appear. The absorption band is not quite at integer multiples of the helium gyrofrequency. Usually, groups of three or four absorption bands occur at integer multiples of the helium gyrofrequency. From $46 \Omega_{He} +$ to $48 \Omega_{He} +$ the absorption bands occur exactly at harmonics of the helium gyrofrequency. The occurrence of the absorption bands at harmonics of the oxygen gyrofrequency is found with different ionospheric data. Again the absorption bands appear near harmonics of the oxygen gyrofrequency, except from $223 \Omega_0 +$ to $244 \Omega_0 +$ they appear exactly at harmonics of the oxygen gyrofrequency. The shifting of the absorption bands had been reported by Horita and Friesen (1975).

CHAPTER 5

CONCLUSION

The Landau instability mechanism which was first proposed by Horita and Watanabe (1969) and Horita (1972) was extended to allow computer calculations of warm plasma effects. An investigation was first made to consider the growth rate and the influence of some ionospheric parameters on the growth rate. Expressions for the growth rate of whistler-mode waves propagating in a plasma penetrated by a tenuous beam of nonthermal particles were obtained by using the full-wave dispersion equation for both cold and warm plasmas as given in the text by Stix (1962). All species of particles involved were assumed to have a Maxwellian velocity distribution, while the collisions between particles were ignored. In the whole analysis, we assumed that the distributions were characterized by two temperatures, parallel and perpendicular to the background magnetic field. In the numerical calculation, data from the ISIS 2 satellite for electrons, H^+ , He^+ and O^+ ions were employed.

There were two instability regions in which positive growth rate occurred. The one called the "electromagnetic" region was in the "low- θ " region above $\theta = 0$, while the other one near the resonance angle θ_{res} was designated as the "electrostatic" region. These regions were separated by a damping region. Throughout the whole analysis, anisotropic temperatures were assumed. It has been found,

in general, that the growth rate in the "electrostatic" region is larger than in the "electromagnetic" region. It is also observed that with increasing T_w^S/T_i^S , the growth rate decreases in both regions, while the growth rate increases with increasing T_w^P/T_i^P . In the "low- θ " region, the growth rate decreases with increasing B_0 . But in the "electrostatic" region, the growth rate varies with B_0 . It had been found that when O^+ is the dominant species, the growth rate has the greatest value in both regions. When H^+ is the dominant species, the growth rate has the smallest value in both regions.

The theory was then applied to search for the absorption bands at harmonics of the ion gyrofrequency. Absorption bands occurred when $T_w^P/T_i^P < 1$ and $T_w^S/T_i^S < 1$ were considered. It has been found that for certain values of $T_w^P/T_i^P < 1$, absorption bands at harmonics of the ion gyrofrequency appear. At $T_w^P/T_i^P = 0.610$, the absorption bands near harmonics of the proton gyrofrequency were found in the "electrostatic" region. The absorption bands appeared near integer multiples of the proton gyrofrequency. Inside the "electrostatic" region, the wave frequency near which the absorption bands started to appear (designated at ω_T) decreased with increasing θ . Absorption bands near harmonics of the helium gyrofrequency were also found for $T_w^P/T_i^P = 0.476$ and $\theta = 89.17^\circ$. It is also found that between $46 \Omega_{He^+}$ to $48 \Omega_{He^+}$, absorption bands occur exactly at harmonics of the helium gyrofrequency. Using different satellite data, absorption bands near harmonics of the oxygen gyrofrequency were also found. It has been observed that from $223 \Omega_{O^+}$

to $244 \Omega_0+$, absorption bands occur exactly at harmonics of the oxygen gyrofrequency. Clearly, the temperatures of the plasma ions were the main parameters which affected the occurrence of the absorption bands within the VLF spectrograms. It also has been found that with decreasing V_s , the magnitude of the absorption bands decrease.

The absorption bands have been seen experimentally on satellite data at harmonics of proton, helium and oxygen gyrofrequencies.

Future work based on the theory given here could investigate the absorption bands at harmonics of an ion gyrofrequency with different ionospheric parameters, such as B_0 , N_k and the kinetic energy of the streaming electrons. One can also apply the theory to find the absorption bands at harmonics of the ion gyrofrequency in the ELF hiss spectrograms. Thus it may provide an explanation for the origin of the VLF and ELF noise. The Landau instability process appears to be a possible general mechanism for auroral hiss, electrostatic noise seen on the Javelin 8.46 rocket, V-shaped VLF noise, saucers and ELF hiss.

APPENDIX A

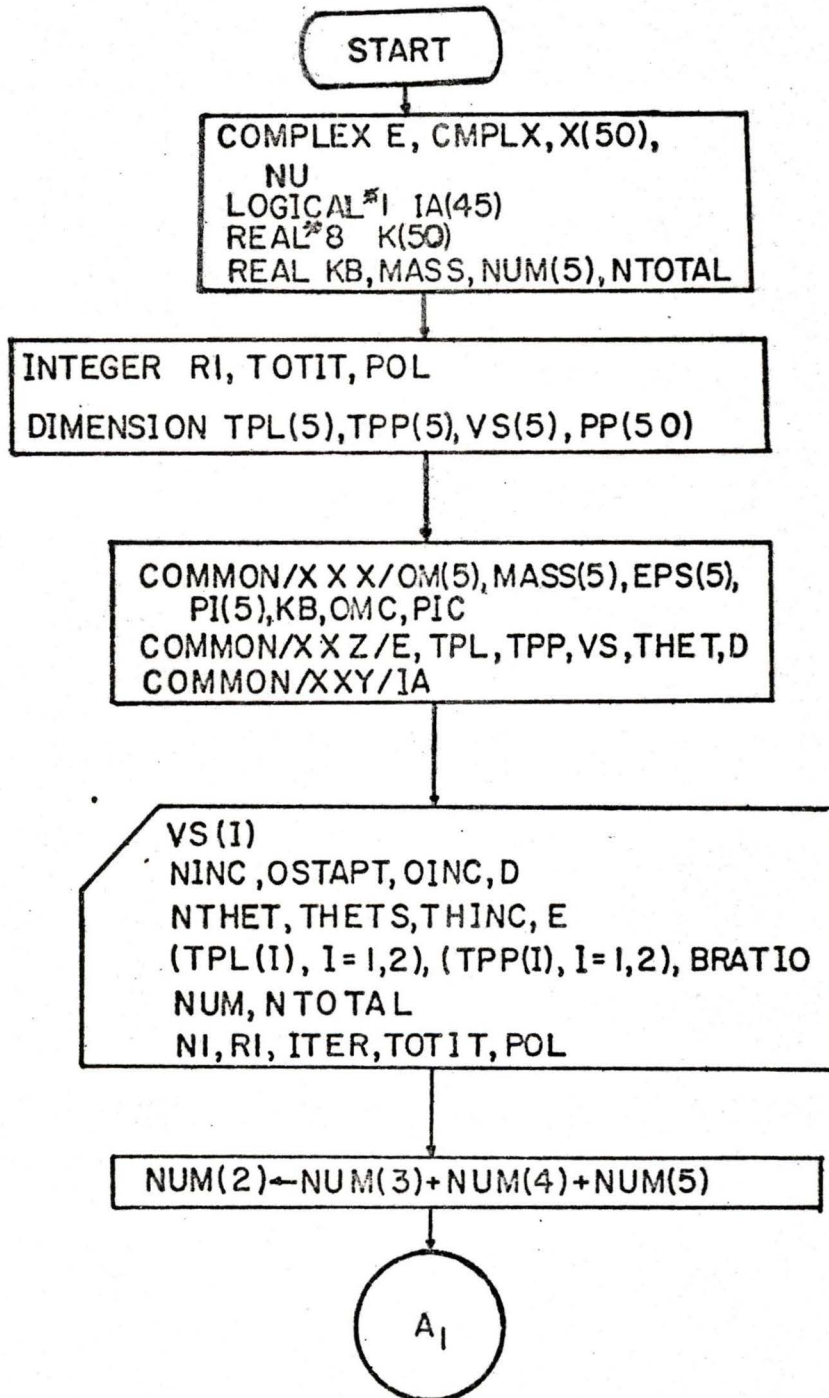
FLOWCHART AND COMPUTER PROGRAM FOR THE POWER ABSORPTION

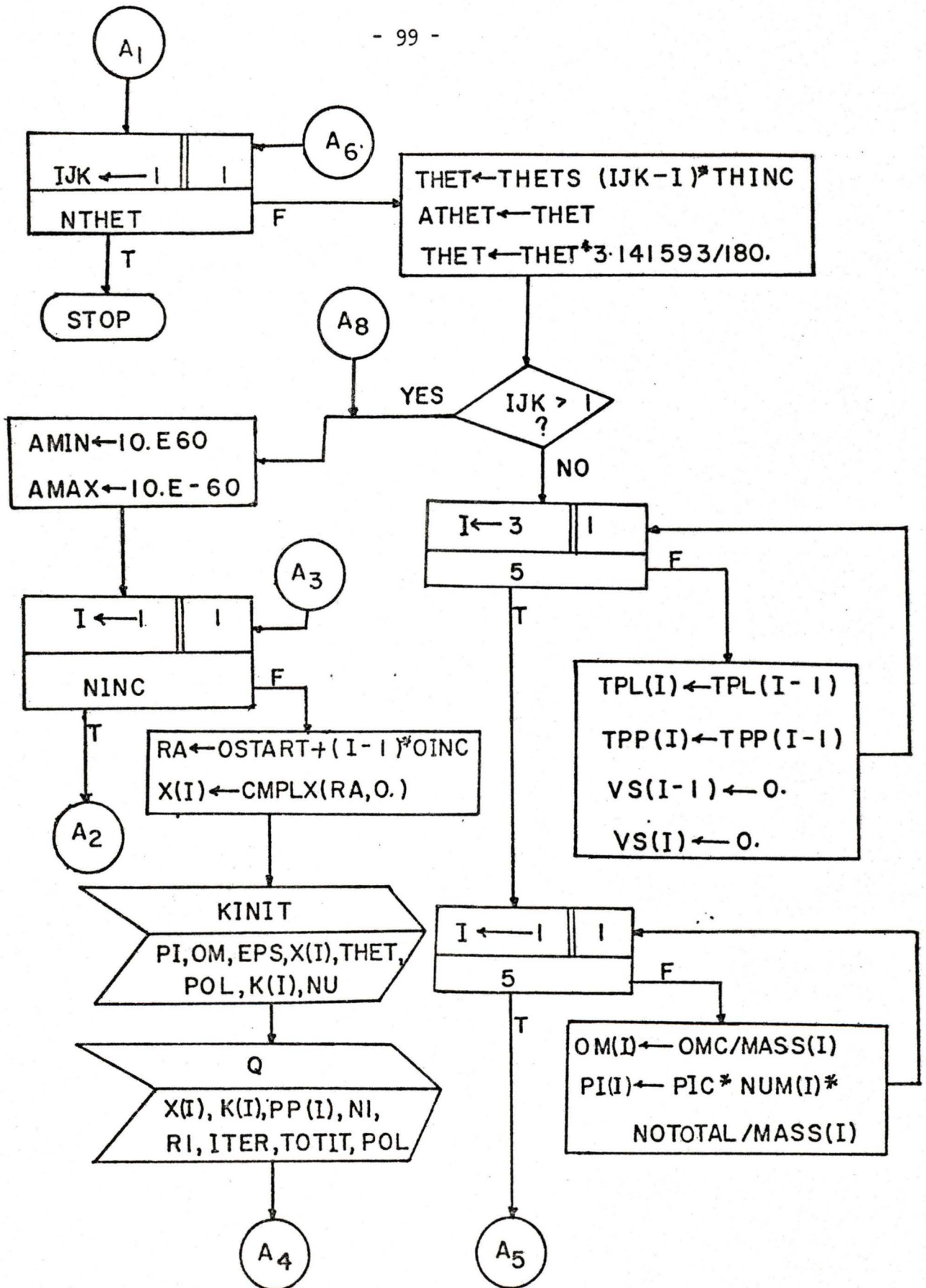
BY CHARGED PARTICLES

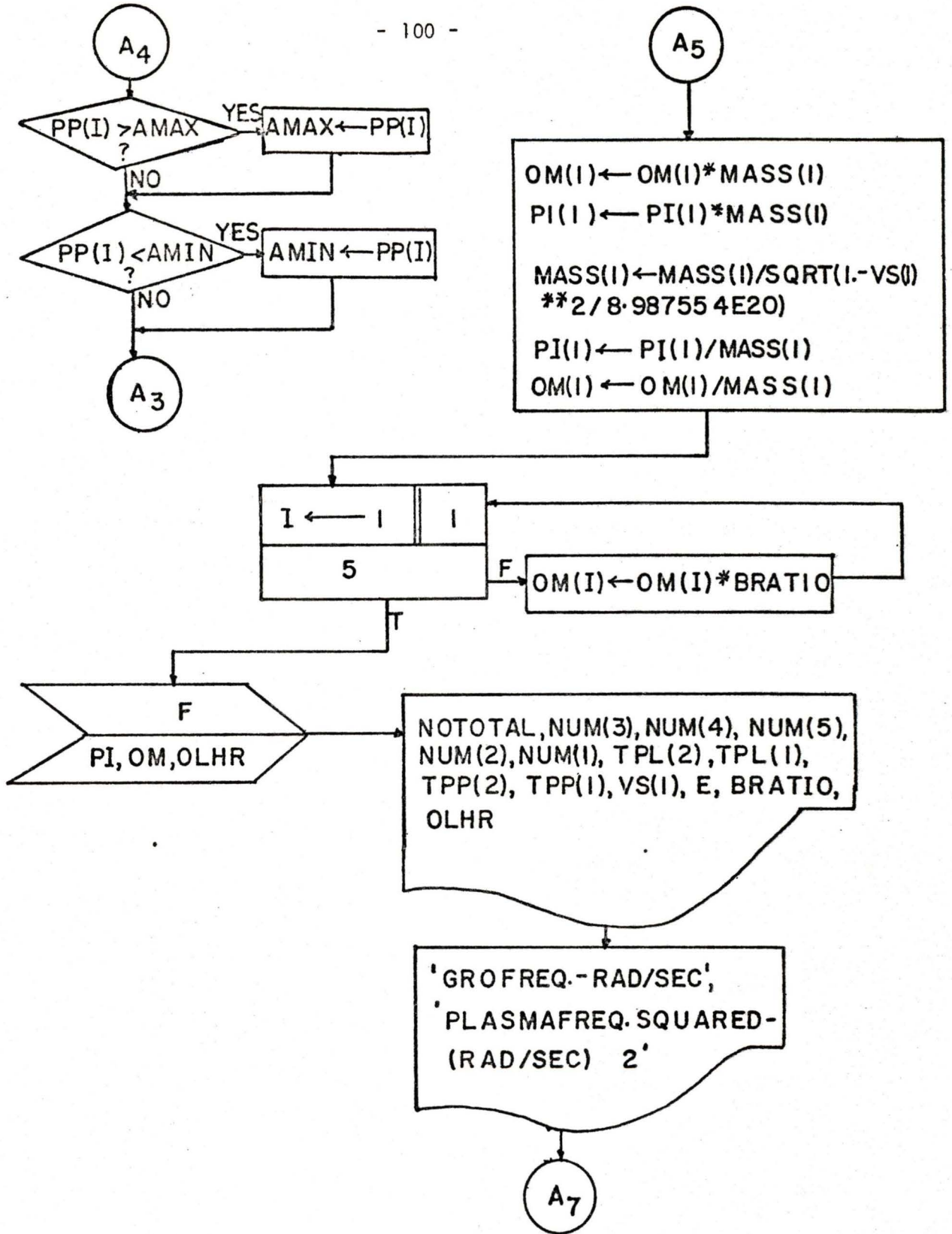
This appendix is divided into two parts. The first part shows the flowchart for the computer program for the power absorption by charged particles. Standard flowchart symbols such as those used by Gear (1973) are adopted. The second part shows the computer program listing.

This computer program is a modification of an existing program developed by Dr. R.E. Horita and Mr. L. Friesen.

Figure A.1 Flowchart for the main program which is used to calculate the gyrofrequencies and plasma frequencies for thermal electrons, nonthermal electrons and ions. The main program also serves as the control of the program to print out the required information.







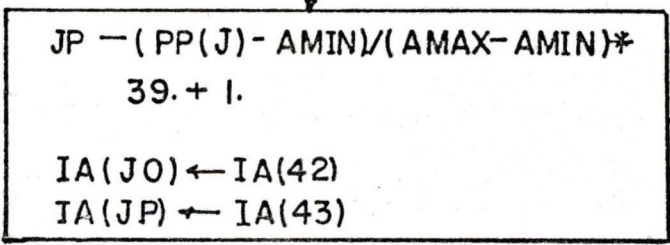
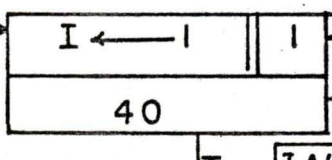
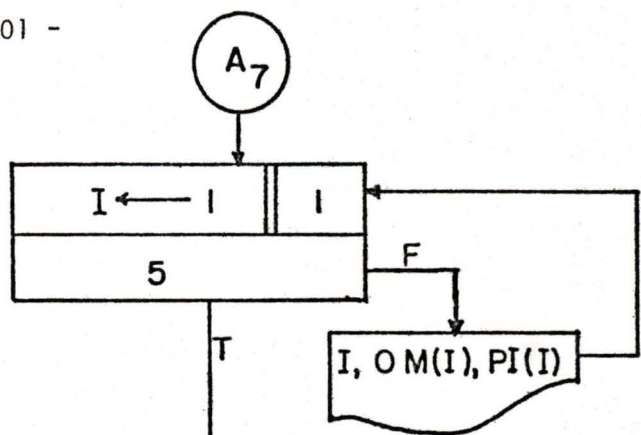
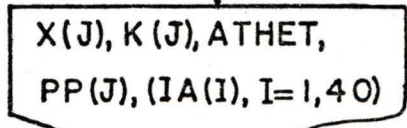
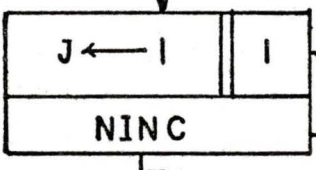
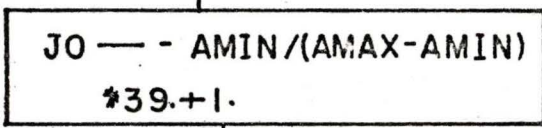
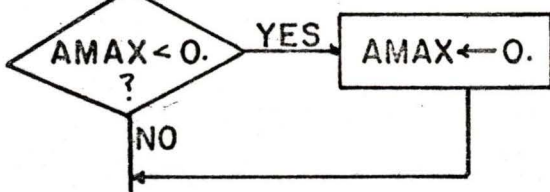
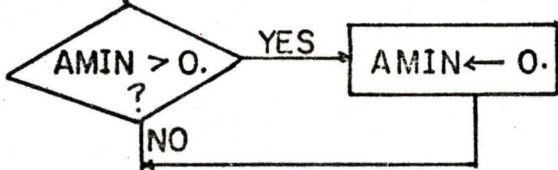
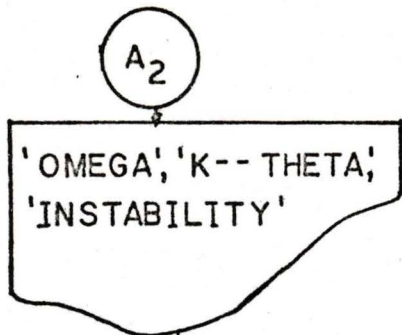


Figure A.2 Flowchart for the subprogram BLOCK DATA which contains the built-in data for the program.

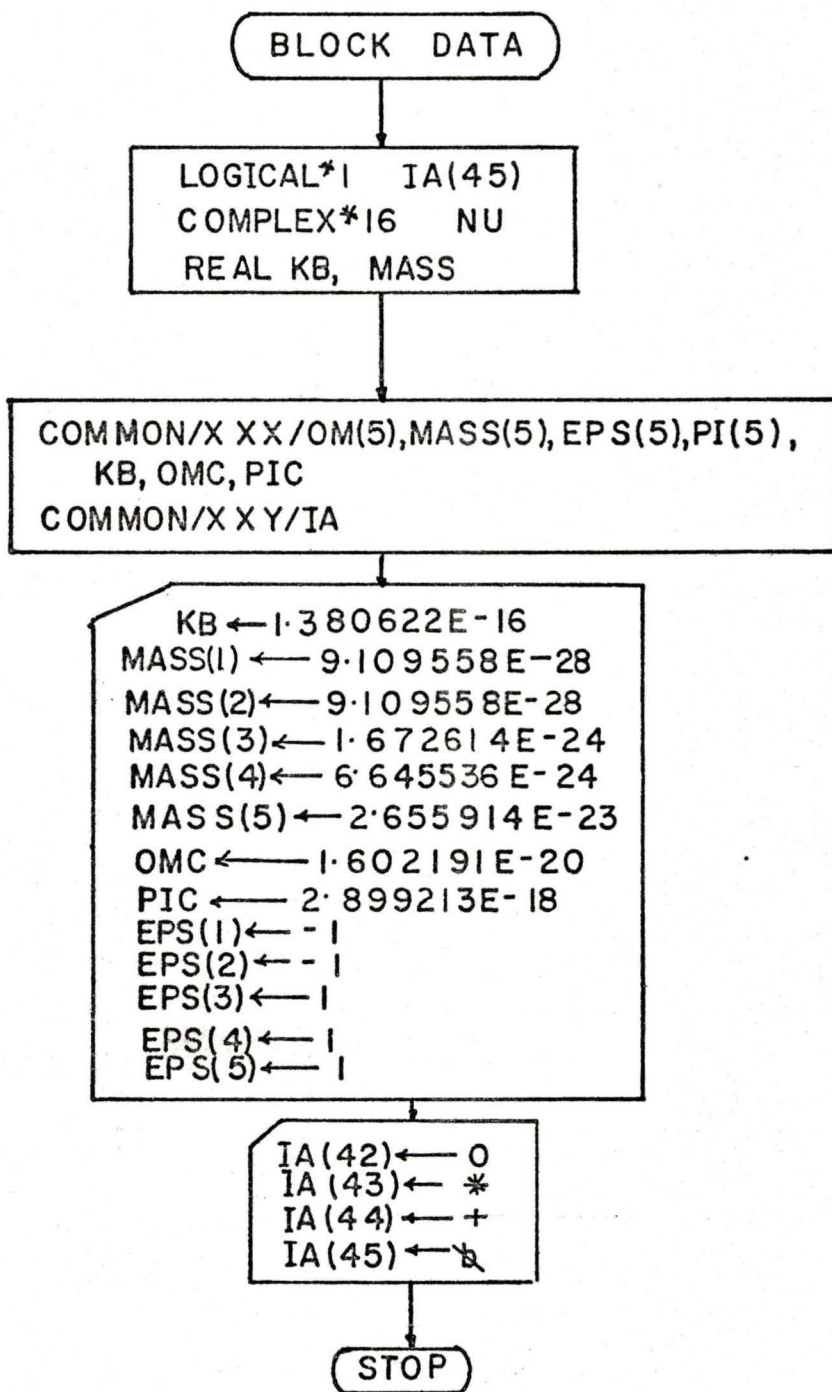
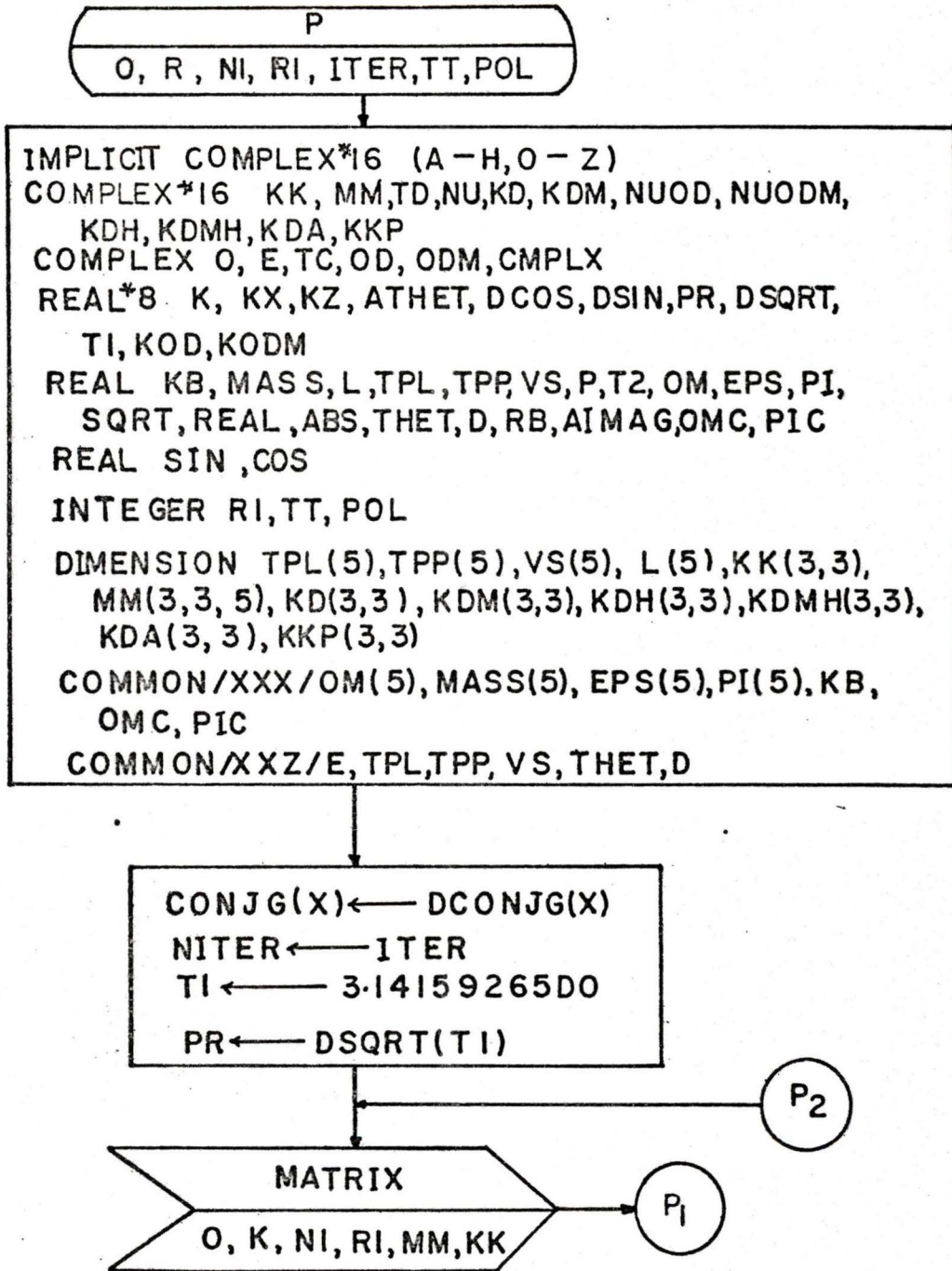
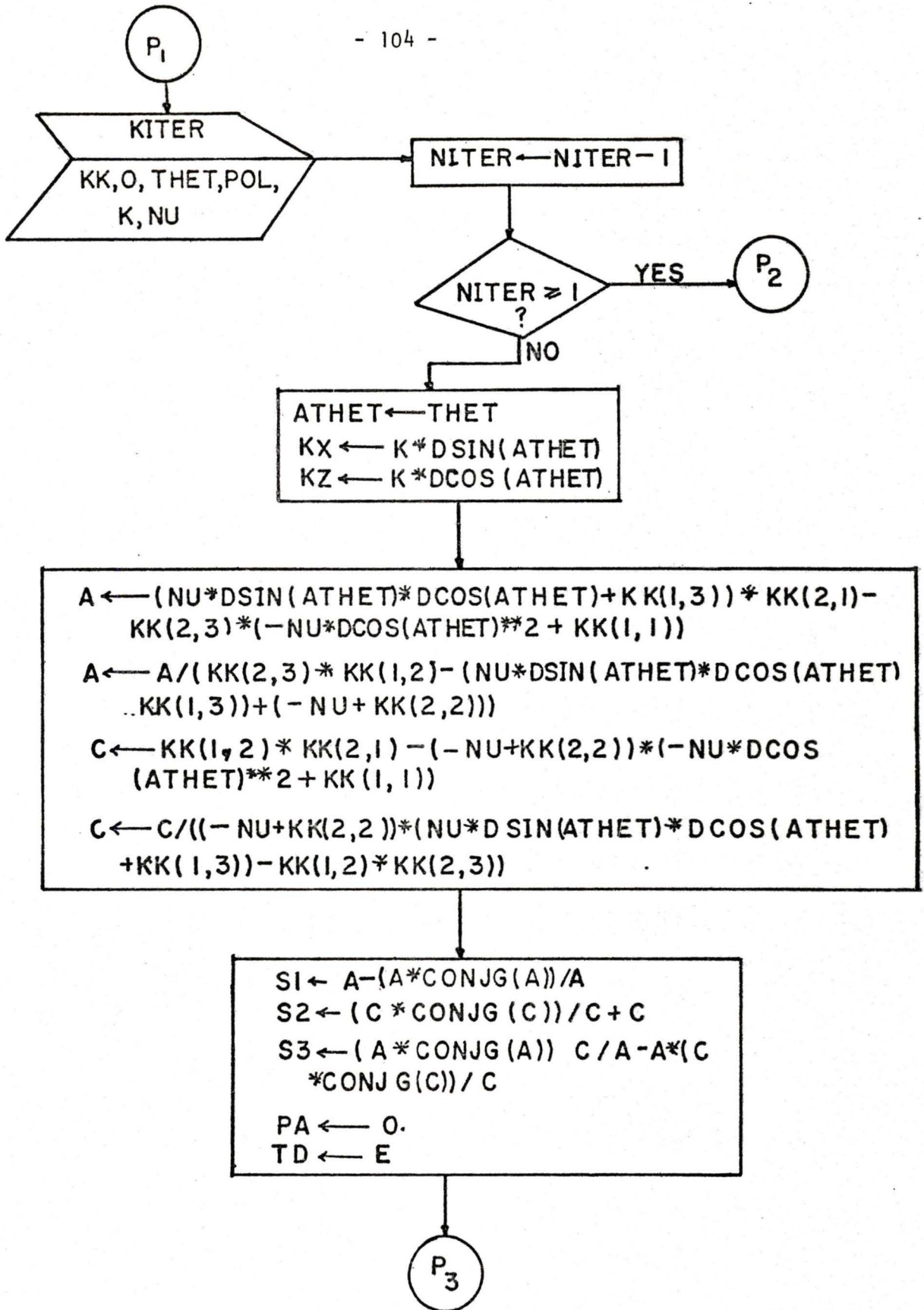


Figure A.3 Flowchart for subprogram P which is used to calculate the power absorption by the charged particles and also to calculate the wave energy.





P₃

PCA ← A * CONJG(A)
PCC ← C * CONJG(C)

I ← I | I
5

PA ← PA + PI(I) * EPS(I) / (16. DO * TI * OM(I)) * TD *
CONJG(TD) * ((MM(1,1,I) + CONJG(MM(1,1,I)))
+ PCA * (MM(2,2,I) + CONJG(MM(2,2,I))) + PCC
* (MM(3,3,I) + CONJG(MM(3,3,I)))) + S1 * (MM(1,2,I)
- CONJG(MM(1,2,I))) + S2 * (MM(1,3,I)
CONJG(MM(1,3,I))) + S3 * (MM(2,3,I) -
CONJG(MM(2,3,I)))

TC ← PA
P ← REAL(TC)
OD ← REAL(O) + D
ODM ← REAL(O) - D

KITER
KK, OD, THET, POL
KOD, NUOD

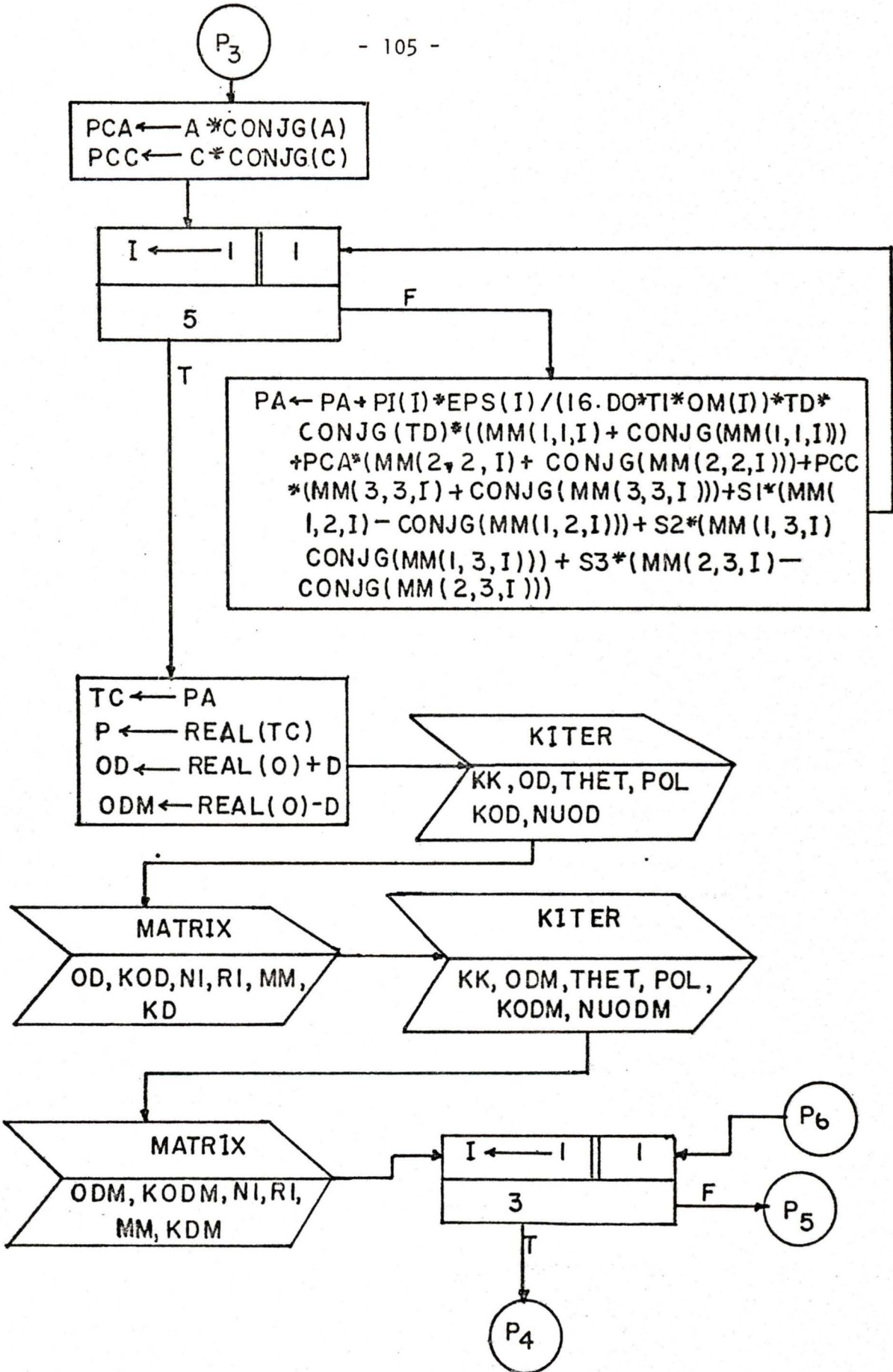
MATRIX
OD, KOD, NI, RI, MM,
KD

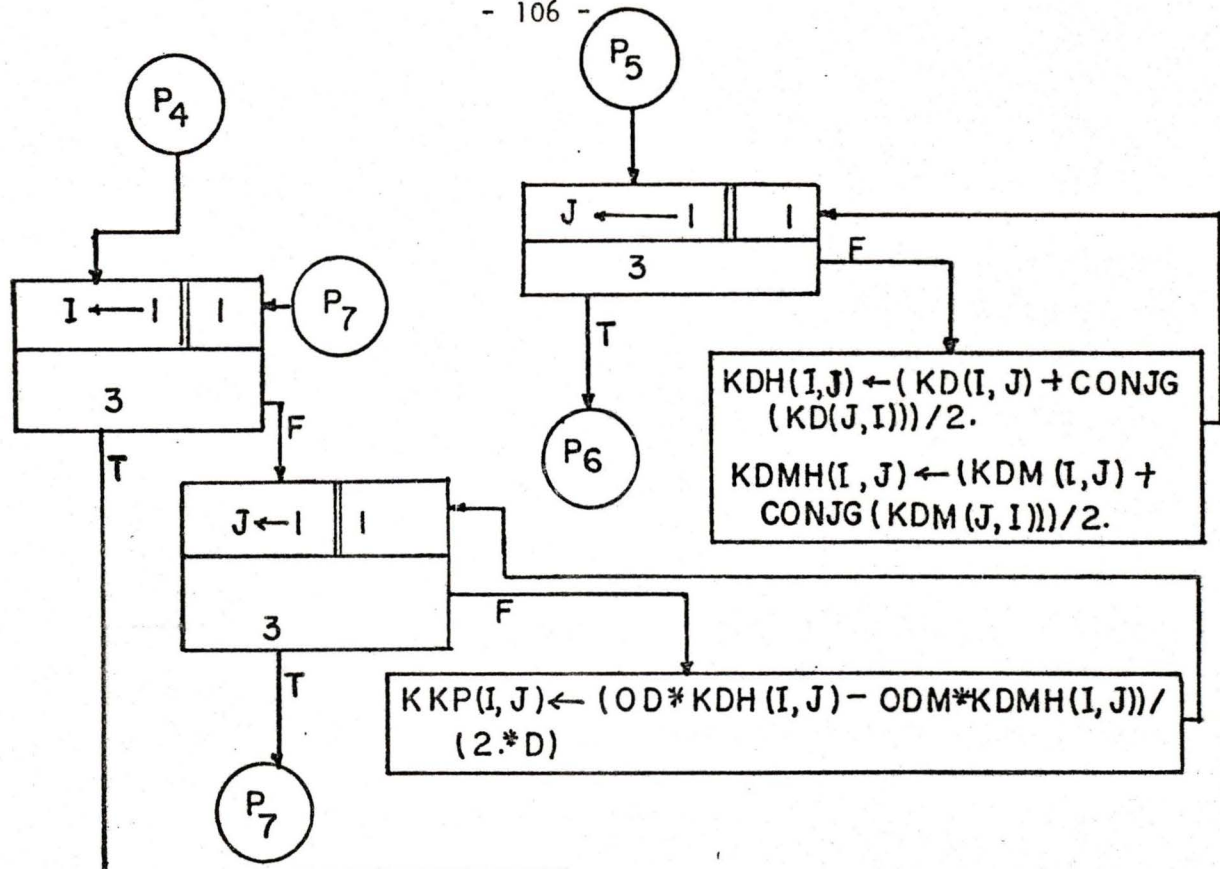
KITER
KK, ODM, THET, POL,
KODM, NUODM

MATRIX
ODM, KODM, NI, RI,
MM, KDM

I ← I | I
3

P₆
P₅
P₄



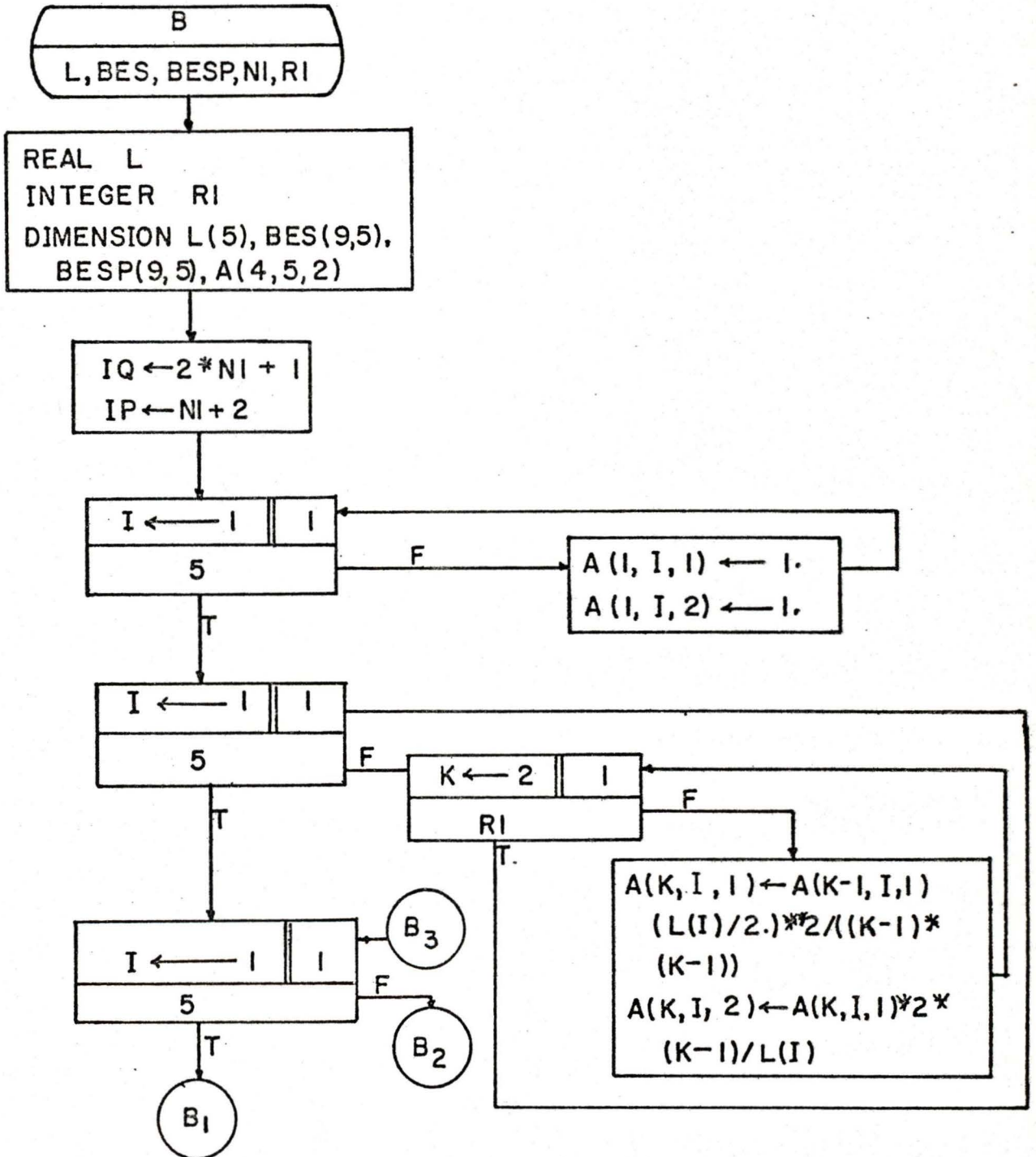


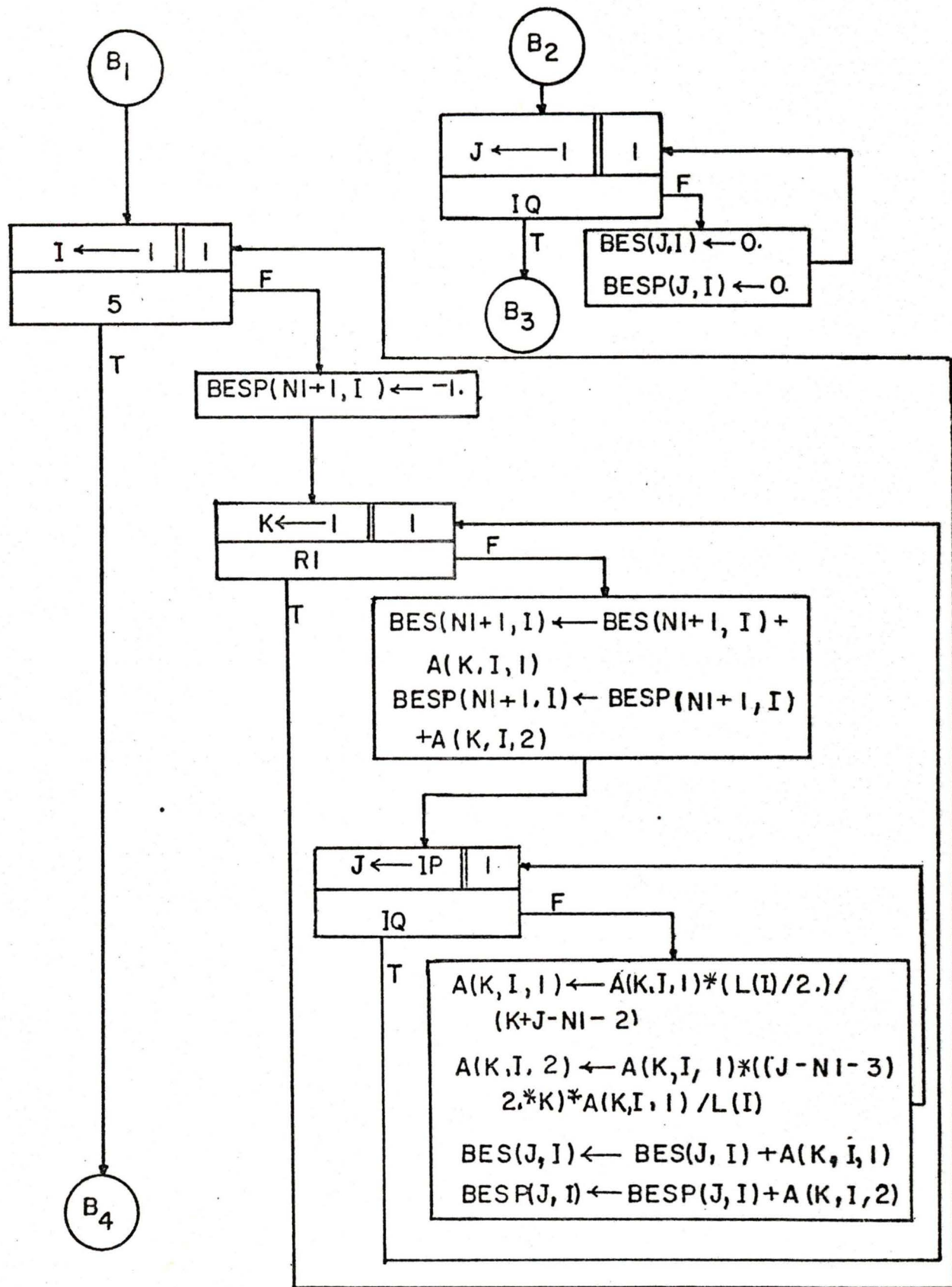
```

Y ← 8.987554E20/O**2
W ← TD*CONJG(TD)/(16.DO*T I)*((Y*KZ**2+KKP(1,1))+
PCA*(Y*(KX**2+KZ**2)+KKP(2,2))+PCC*(Y*KX**2+
KKP(3,3))+A*KKP(1,2)+CONJG(A)*KKP(2,1)+CONJG(A)*
C*KKP(2,3)+A*CONJG(C)*KKP(3,2)+C*KKP(1,3)-
Y*KX*KZ)+CONJG(C)*(KKP(3,1)-Y*KX*KZ))
RB ← -PA/(2.*W)
O ← REAL(O)+CMPLX(O.,RB)
    
```

RETURN

Figure A.4 Flowchart for subprogram B which is used to calculate the modified Bessel function of the first kind and its derivative.





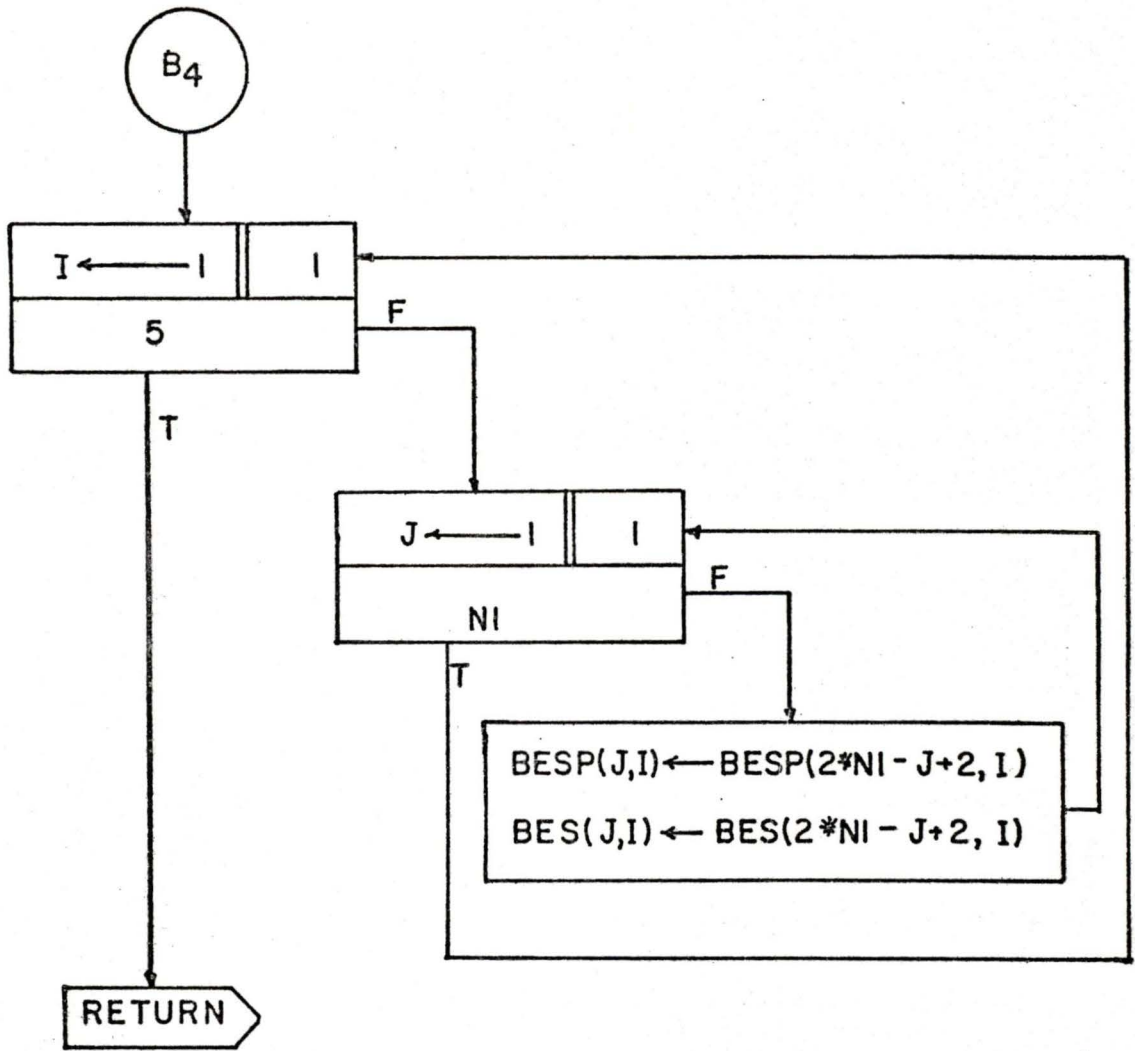


Figure A.5 Flowchart for subprogram KITER which is used to compute the value of the wave vector k for a warm plasma.

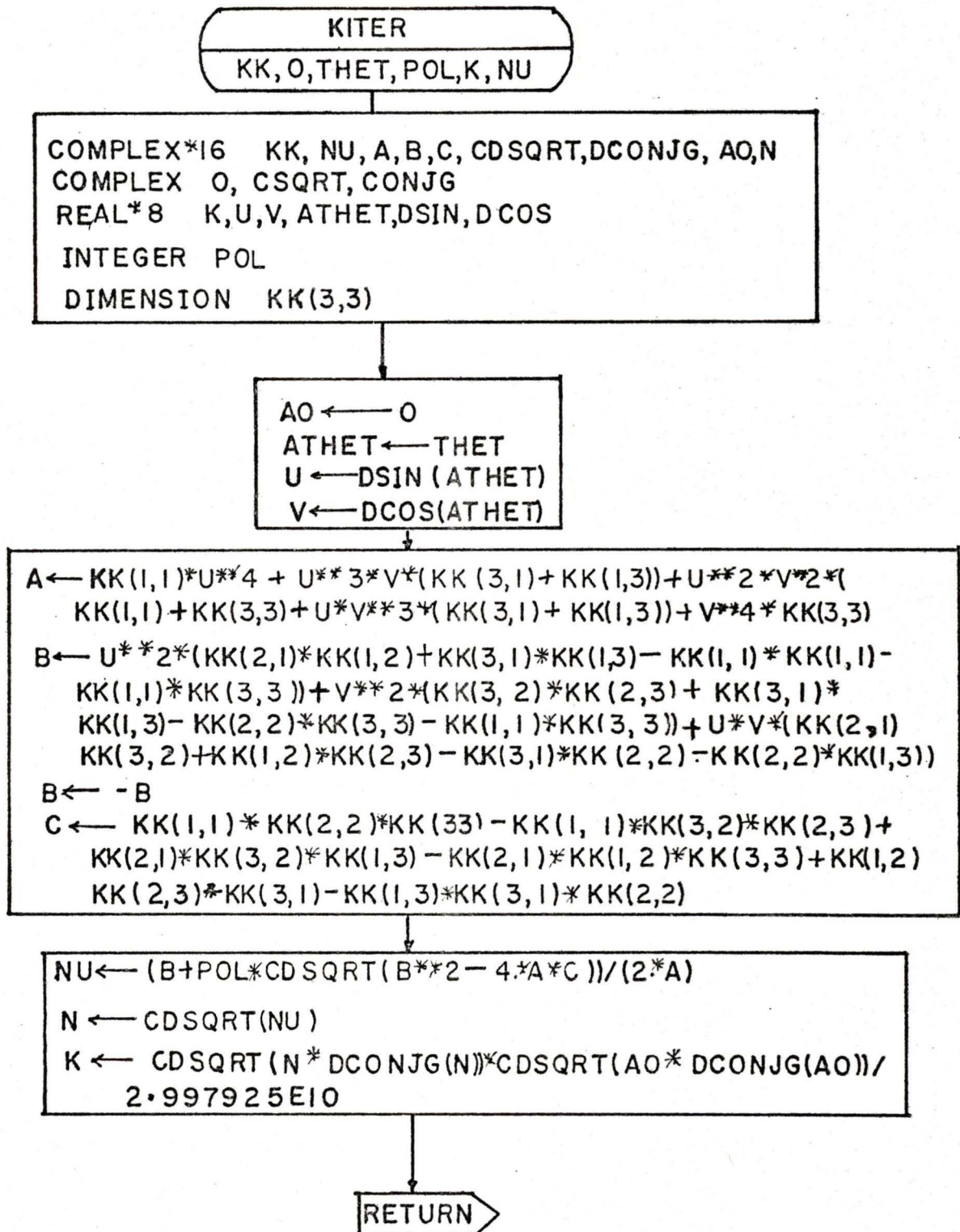
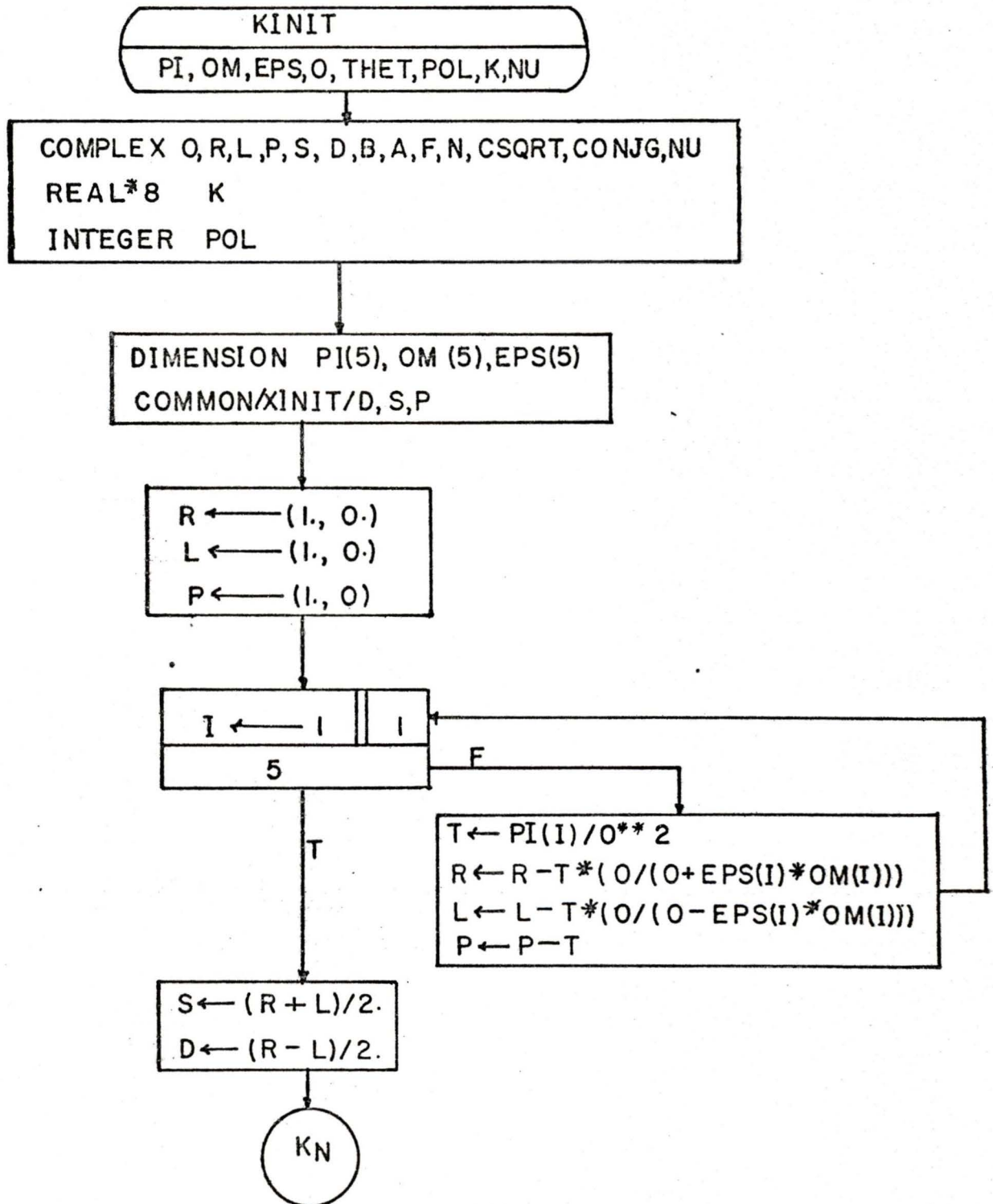


Figure A.6 Flowchart for subprogram KINIT which is used to compute the value of the wave vector k for a cold plasma.



KN

$B \leftarrow R * L * \sin(\text{THET})^{**2} + P * S * (1. + \cos(\text{THET})^{**2})$
 $A \leftarrow S * \sin(\text{THET})^{**2} + P * \cos(\text{THET})^{**2}$
 $F \leftarrow 4. * (P * D * \cos(\text{THET})^{**2})$

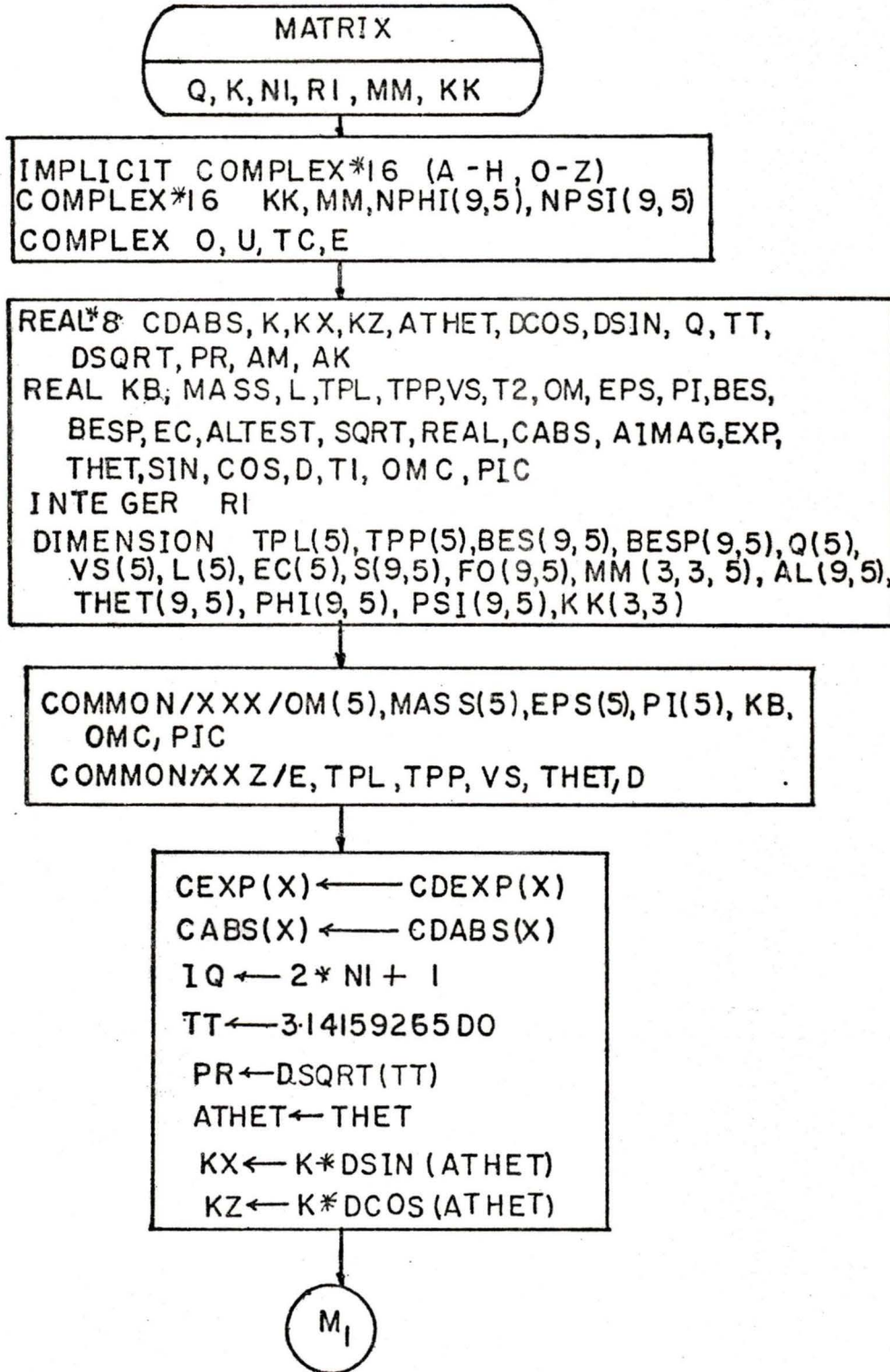
$N \leftarrow P * S$
 $F \leftarrow ((R * L - N) * \sin(\text{THET})^{**2})^{**2} + F$
 $F \leftarrow \text{CSQRT}(F)$

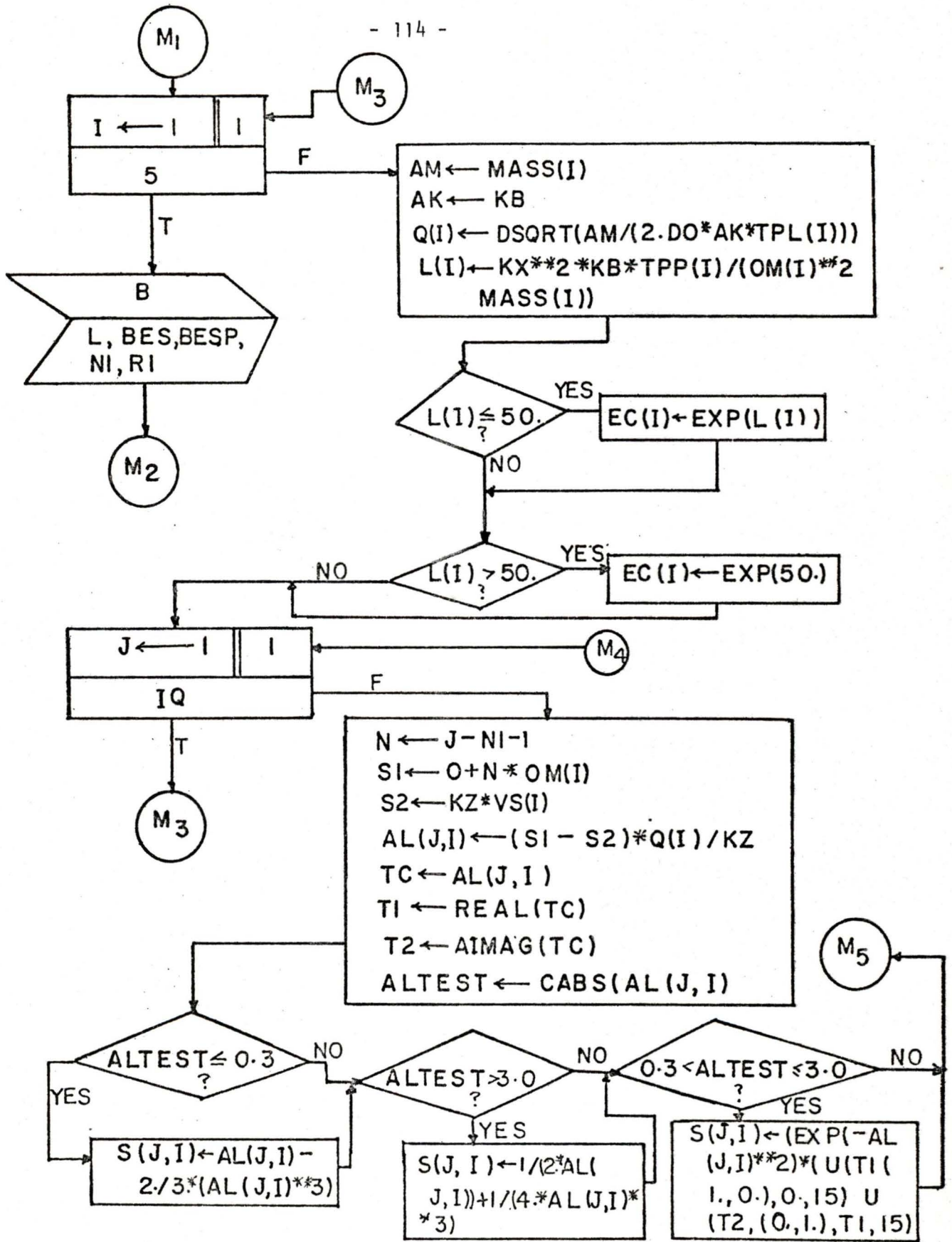
$N \leftarrow (B + \text{POL} * F) / (2. * A)$
 $\text{NU} \leftarrow N$
 $N \leftarrow \text{CSQRT}(N)$

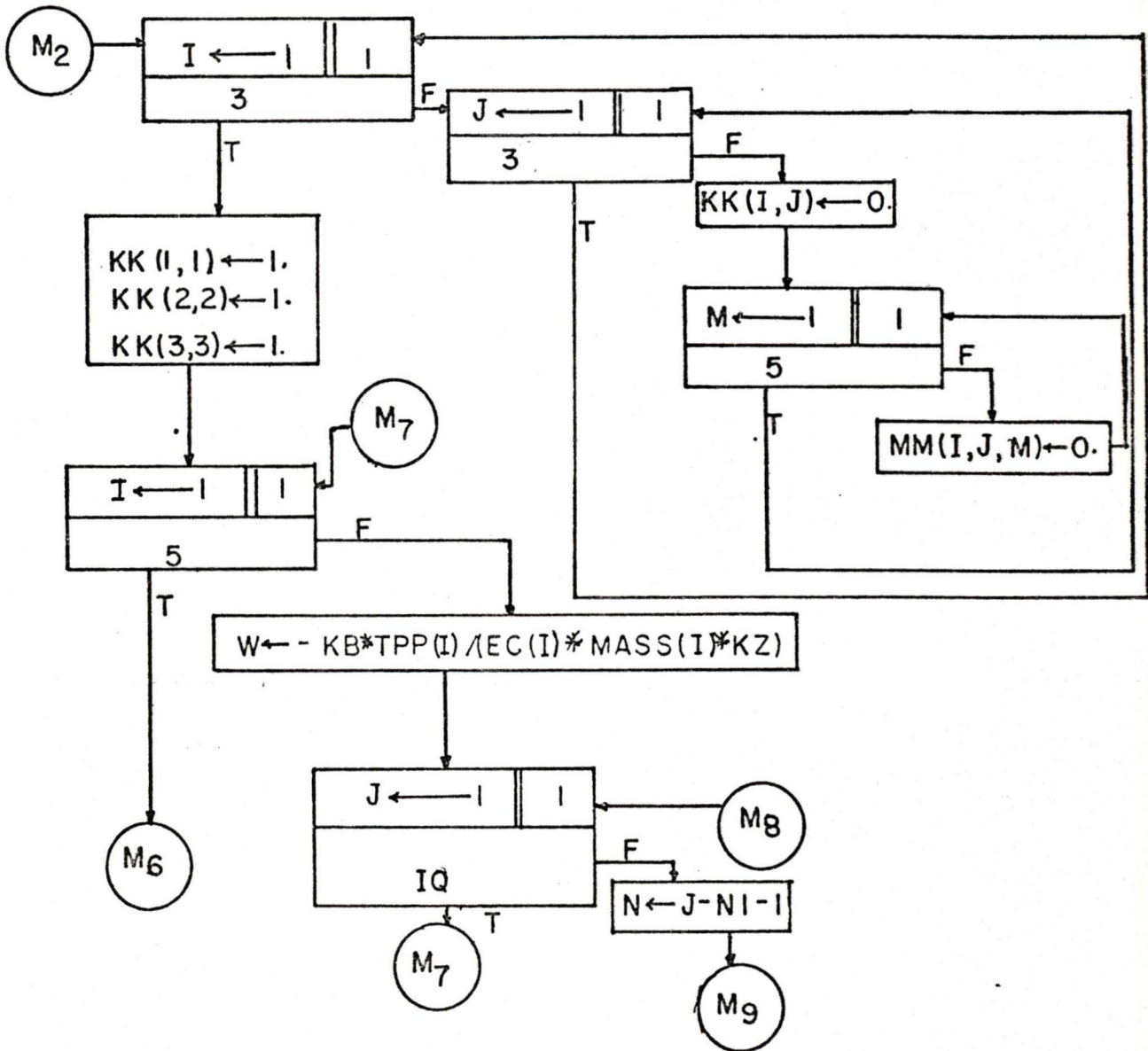
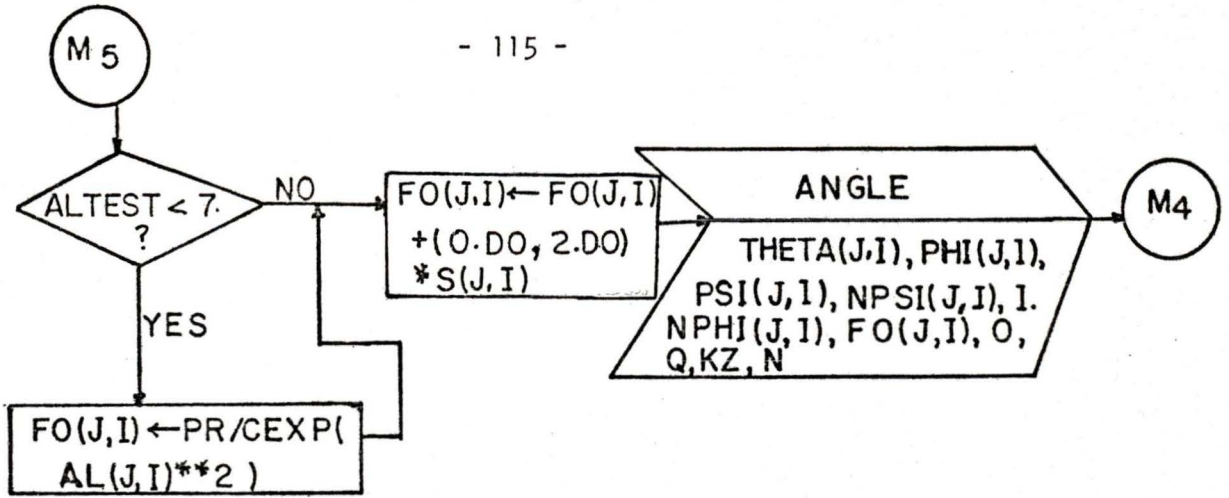
$K \leftarrow \text{CSQRT}(N * \text{CONJG}(N)) * \text{CSQRT}(O + \text{CONJG}(O)) /$
2.997925E10
 $N \leftarrow N * N$

RETURN

Figure A.7 Flowchart for subprogram MATRIX which is used to compute the components of the mobility tensor M and the components of the dielectric tensor KK.







M9

```

MM(1,1,I) ← MM(1,1,I) + W*OM(I)*EPS(I)*N*N*BES(J,I)*THETA(J,I)/
L(I)
MM(2,2,I) ← MM(2,2,I) + W*OM(I)*EPS(I)*THETA(J,I)*(N*N*BES
(J,I)/L(I) + 2.DO*L(I)*BES(J,I) - 2.DO*L(I)*BESP(J,I))
MM(1,2,I) ← MM(1,2,I) + W*OM(I)*(O.DO, I.DO)*N*THETA(J,I)*
(BES(J,I) - BESP(J,I))
MM(1,3,I) ← MM(1,3,I) + W*EPS(I)*N*KX*BES(J,I)/L(I)*(N*
PHI(J,I) - PSI(J,I))
MM(2,3,I) ← MM(2,3,I) - W*(O.DO, I.DO)*KX*(BES(J,I) -
BESP(J,I))*(N*PHI(J,I) - PSI(J,I))
MM(3,3,I) ← MM(3,3,I) + OM(I)*EPS(I)/(EC(I)*KZ)*BES(J,I)
(N*NPHI(J,I) - NPSI(J,I))

```

```

MM(3,1,I) ← MM(1,3,I)
MM(3,2,I) ← -MM(2,3,I)
MM(2,1,I) ← -MM(1,2,I)

```

M8

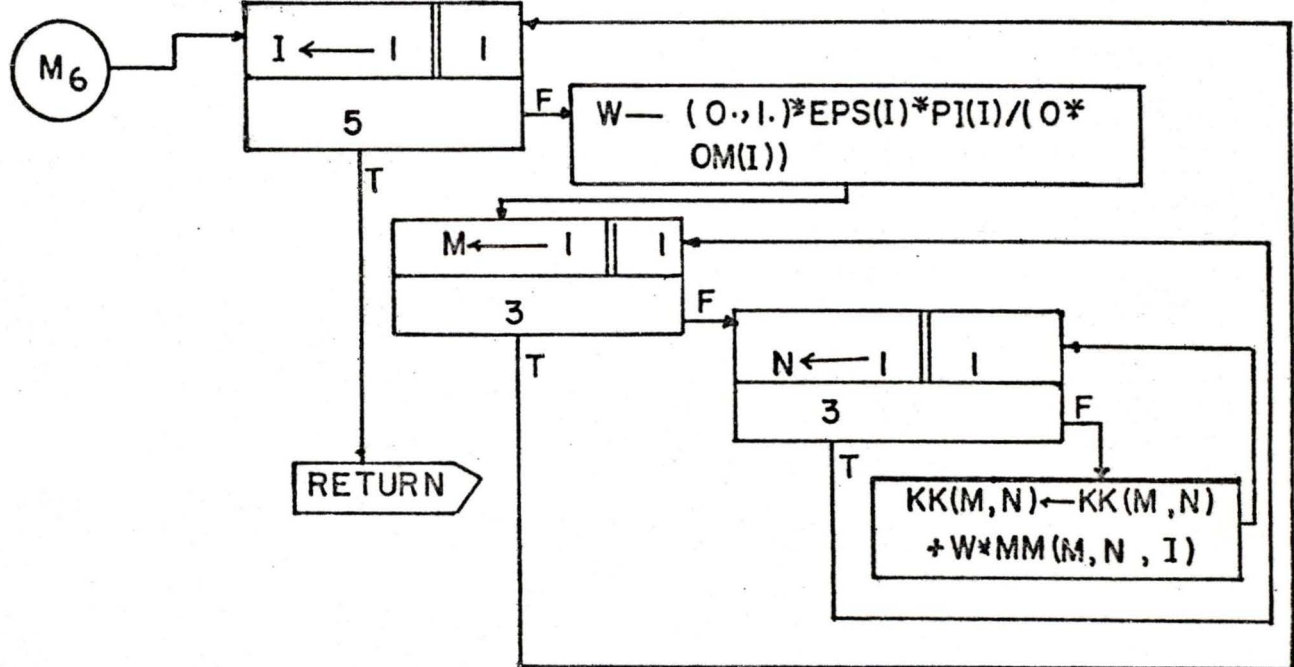


Figure A.8 Flowchart for subprogram Q which is used to check the real and imaginary parts of the wave frequency.

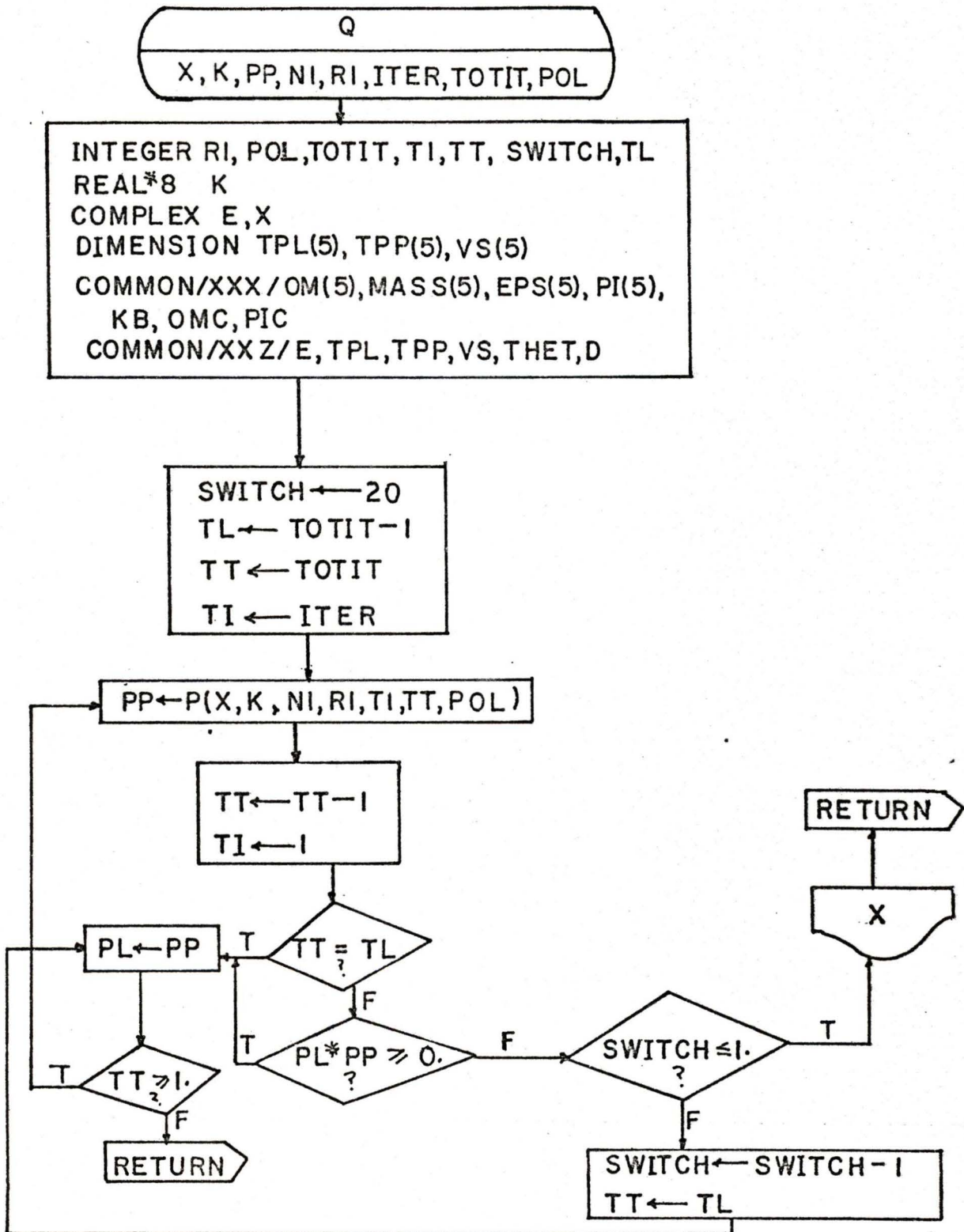


Figure A.9 Flowchart for subprogram ANGLE which is used to compute $\langle \bar{H} \rangle_n$, $\langle \bar{\phi} \rangle_n$, $\langle \bar{\psi} \rangle_n$, $\langle V_{z\bar{\phi}} \rangle_n$ and $\langle V_{z\bar{\psi}} \rangle_n$. Those quantities are the arguments of the mobility tensor.

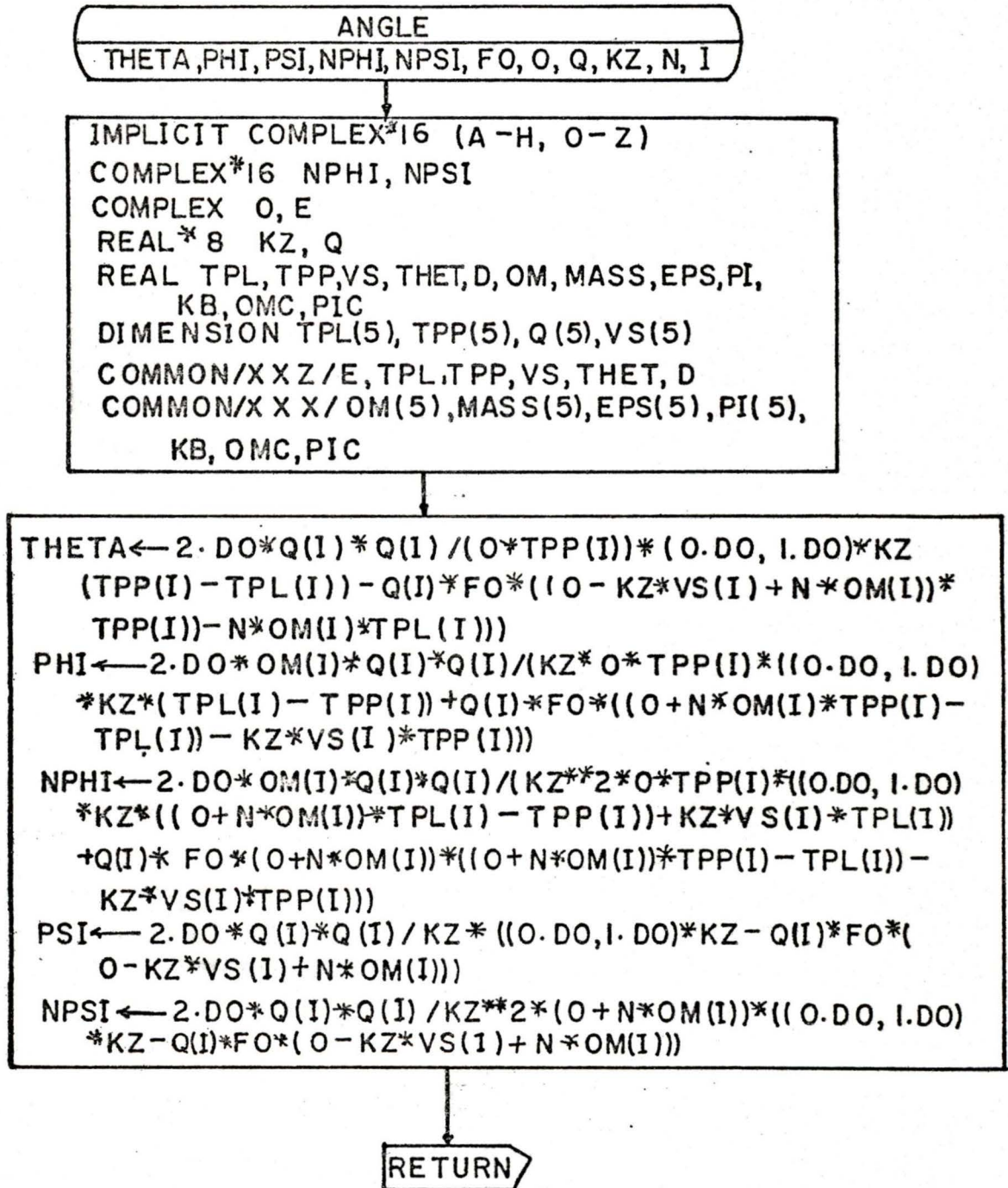


Figure A.10 Flowchart for subprogram U which is used to evaluate the imaginary part of the constant F_0 .

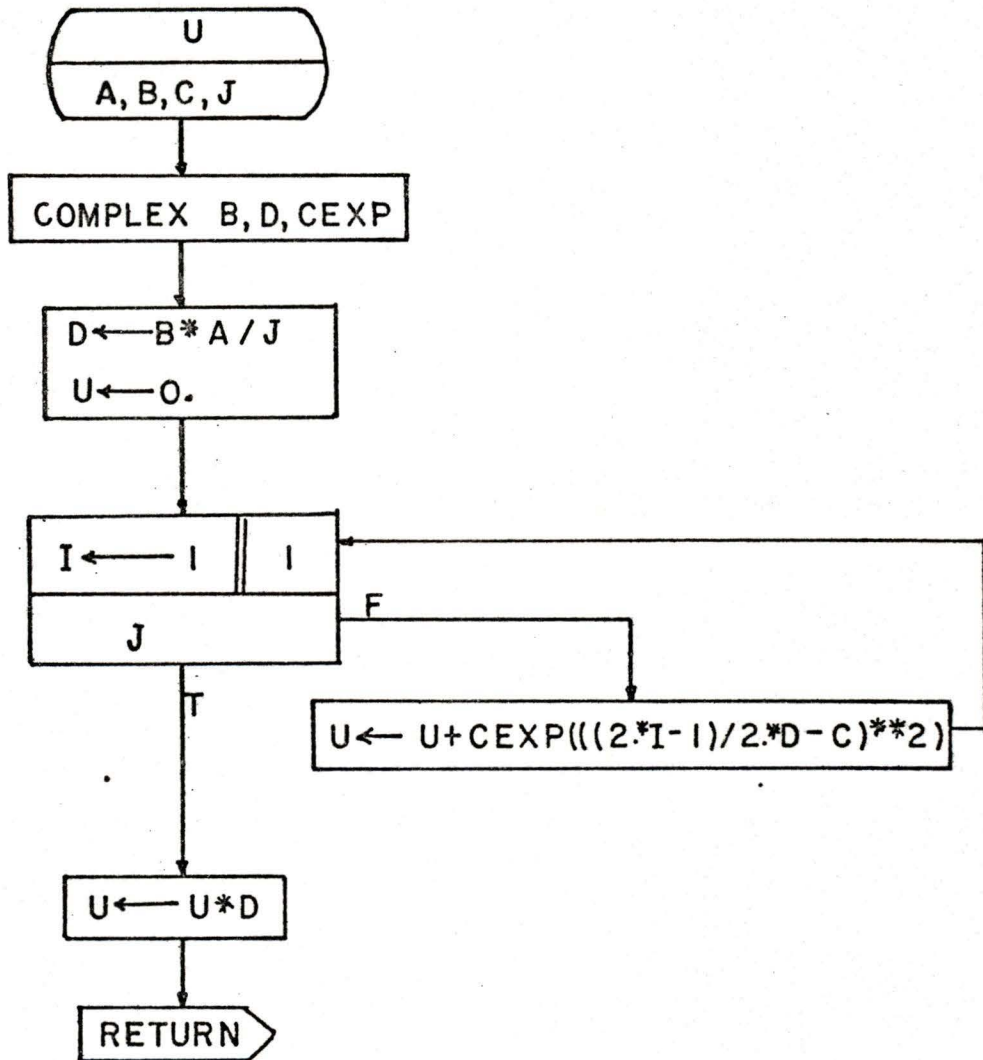
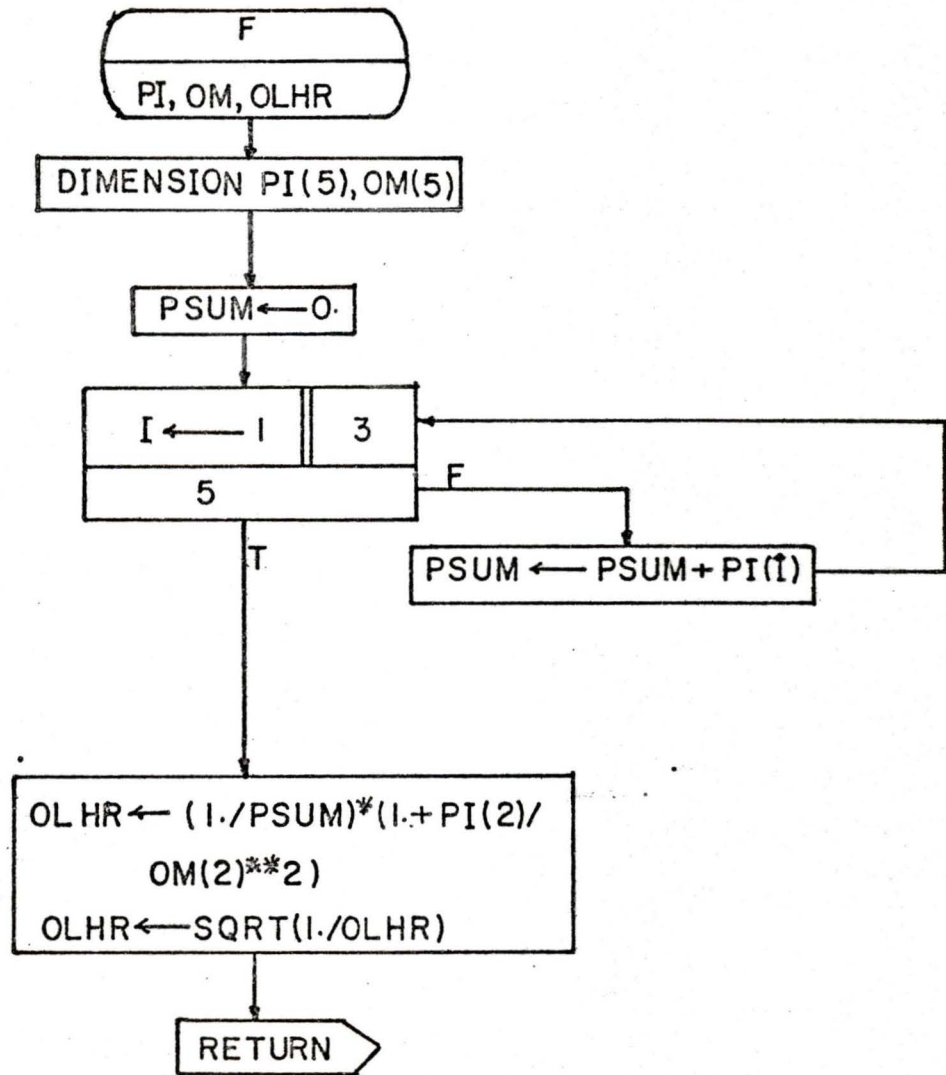


Figure A.11 Flowchart for subprogram F which is used to compute the LHR frequency ($S = 0$).



COMPUTER PROGRAM FOR THE POWER ABSORPTION BY CHARGED PARTICLES

FORTRAN SOURCE LIST

```
C   MAIN PROGRAM WHICH IS USED TO CALCULATE THE GYROFREQUENCIES
C   AND PLASMA FREQUENCIES FOR THERMAL ELECTRONS, NONTHERMAL
C   ELECTRONS AND IONS. IT ALSO SERVES AS THE CONTROL OF THE
C   PROGRAM TO PRINT OUT THE REQUIRED INFORMATION
      COMPLEX E, CMPLX, X(50), NU
      LOGICAL*1 IA(45)
      REAL*8 K(50)
      REAL KB, MASS, NUM(5), NTOTAL
      INTEGER R1, TOTIT, POL
      DIMENSION TPL(5), TPP(5), VS(5), PP(50)
      COMMON/XXX/OM(5), MASS(5), EPS(5), PI(5), KB, OMC, PIC
      COMMON/XXZ/E, TPL, TPP, VS, THET, D
      COMMON/XXY/IA
C   INPUT DATA FOR THE VELOCITY OF THE THERMAL ELECTRONS, THE
C   WAVE FREQUENCY IN RAD/SEC, INCREMENTS OF THE WAVE FREQUENCY,
C   THE PARALLEL AND PERPENDICULAR TEMPERATURES OF THE ELECTRONS
C   AND IONS, THE BACKGROUND MAGNETIC FIELD STRENGTH, THE NUMBER
C   DENSITIES OF ELECTRONS AND IONS, THE NUMBER OF TIMES FOR
C   ITERATION, AND THE SIGN FOR POLARIZATION. ALL VALUES ARE IN
C   C.G.S. UNIT
      READ(5,20) VS(1)
      READ(5,30) NINC, OSTART, OINC, D
      READ(5,45) NTHET, THETS, THINC, E
      READ(5,20) (TPL(I), I=1,2), (TPP(I), I=1,2), BRATIO
      READ(5,20) NUM, NTOTAL
      READ(5,40) N1, R1, ITER, TOTIT, POL
      NUM(2)=NUM(3)+NUM(4)+NUM(5)
      DO 120 IJK=1, NTHET
      THET=THETS+(IJK-1)*THINC
      ATHET=THET
      THET=THET*3.141593/180.
      IF(IJK.GT.1) GO TO 65
      DO 10 I=3,5
      TPL(I)=TPL(I-1)
      TPP(I)=TPP(I-1)
      VS(I-1)=0
10   VS(I)=0
20   FORMAT(8F10.5)
30   FORMAT(12,8X,4F10.5)
40   FORMAT(5I2)
45   FORMAT(12,8X,4F10.5)
C   CALCULATION OF GYROFREQUENCIES AND PLASMA FREQUENCIES
C   FOR THE ELECTRONS (BOTH THERMAL AND NONTHERMAL) AND IONS
```

```
DO 50 I=1,5
OM(I)=OMC/MASS(I)
50 PI(I)=PIC*NUM(I)*NTOTAL/MASS(I)
OM(I)=OM(I)*MASS(I)
PI(I)=PI(I)*MASS(I)
MASS(I)=MASS(I)/SQRT(1.-VS(I)**2/8.987554E20)
PI(I)=PI(I)/MASS(I)
OM(I)=OM(I)/MASS(I)
DO 60 I=1,5
60 OM(I)=OM(I)*BRATIO
CALL F(PI,OM,OLHR)
C PRINTOUT THE REQUIRED INFORMATION AND THE GRAPH OF THE
C GROWTH RATE AS A FUNCTION OF THE POWER ABSORPTION
WRITE(6,80) NTOTAL,NUM(3),NUM(4),NUM(5),NUM(2),NUM(1),
/TPL(2),TPL(1),TPP(2),TPP(1),VS(1),E,BRATIO,OLHR
WRITE(6,95)
95 FORMAT(////30X,'GYROFREQ.-RAD/SEC',4X,'PLASMAFREQ. SQUARED-
/(RAD/SEC.)**2'//)
DO 130 I=1,5
130 WRITE(6,140) I,OM(I),PI(I)
140 FORMAT(28X,11,6X,E11.4,16X,E11.4/)
65 CONTINUE
AMIN=10.E60
AMAX=10.E-60
DO 70 I=1,NINC
RA=OSTRAT+(I-1)*OINC
X(I)=CMPLX(RA,0.)
CALL KINIT(PI,OM,EPS,X(I),THET,POL,K(I),NU)
CALL Q(I),K(I),PP(I),NI,R1,ITER,TOTIT,POL)
IF(PP(I).GT.AMAX) AMAX=PP(I)
70 IF(PP(I).LT.AMIN) AMIN=PP(I)
WRITE(6,85)
85 FORMAT('1'//14X,'OMEGA',16X,'K -- THETA',5X,'INSTABILITY'//)
IF(AMIN.GT.0.) AMIN=0
IF(AMAX.LT.0.) AMAX=0
JO=-AMIN/(AMAX-AMIN)*39.+1.
DO 100 J=1,NINC
DO 90 I=1,40
90 IA(I)=IA(45)
IA(I)=IA(44)
IA(40)=IA(44)
JP=(PP(J)-AMIN)/(AMAX-AMIN)*39.+1.
IA(JO)=IA(42)
IA(JP)=IA(43)
100 WRITE(6,110) X(J),K(J),ATHET,PP(J),(IA(I),I=1,40)
120 CONTINUE
STOP
```

```
80  FORMAT('1'////////40X,'RELATIVE INSTABILITY WITH FREQUENCY'  
      //////////25X,'DENSITY OF PARTICLES ',E10.4,'/CM**3'///27X,F7.5,'  
      /H, ',F7.5,' HE, ',F7.5,' O ',F7.5,' E, ',F9.7,' STREAMING  
      /E.'///25X,'PARALLEL TEMP.OF IONS = ',E11.4,'DEG.K.,OF  
      /STREAMING E = ',E11.4,' DEG. K.'///25X,'PERP.TEMP.OF IONS =  
      /',E11.4,' DEG. K., OF STREAMING E = ',E11.4,'///25X,'  
      /VELOCITY OF STREAM = ',E10.4,'CM/SEC.'///25X,'ELECTRIC  
      /FIELD = (' ,E10.4,' , ',E10.4,' )'///25X,'MAGNETIC FIELD (GAUSS)  
      /= ',F8.4///25X,'LOWER HYBRID RESONANCE OMEGA-(RAD/SEC.) =  
      /',F10.3)  
110  FORMAT(' (',F8.1,' , ',E11.4,' )',3X,E11.4,3X,F6.2,6X,  
      /E11.4,4X,/40A1)  
      END  
  
C      NUMERICAL VALUE OF BOLTZMAN'S CONSTANT (KB)  
C      MASSES OF THERMAL ELECTRONS (MASS 1) AND NONTHERMAL  
C      ELECTRONS (MASS 2)  
C      MASSES OF IONS (MASS 3 TO MASS 5, FOR PROTON, HELIUM ION  
C      AND OXYGEN ION)  
C      NUMERICAL VALUE OF THE RATIO OF ELECTRON CHARGE TO  
C      VELOCITY OF LIGHT (E/C)  
C      NUMERICAL VALUE OF THE CONSTANT 4 PIC**2  
C      ALL VALUES ARE IN C.G.S. UNITS  
C      SIGNS OF CHARGES FOR ELECTRONS AND IONS (EPS)  
      BLOCK DATA  
      LOGICAL*1 IA(45)  
      COMPLEX*16 NU  
      REAL KB, MASS  
      COMMON/XXX/OM(5), MASS(5), EPS(5), PI(5), KB, OMC, PIC  
      COMMON/XXY/IA  
      DATA KB/1.380622E-16/, MASS(1)/9.109558E-28/, MASS(2)/9.109558  
      /E-28/, MASS(3)/1.672614E-24/, MASS(4)/6.645535E-24/, MASS(5)/  
      /2.655914E-23/, OMC/1.602191E-20/, PIC/2.899213E-18/, EPS(1)/  
      /-1./, EPS(2)/-1./, EPS(3)/1./, EPS(4)/1./, EPS(5)/1./  
      DATA IA(42)/'0', IA(43)/'*'/, IA(44)/'+'/, IA(45)/' '/  
      END  
  
C      FUNCTIONAL SUBPROGRAM FOR THE CALCULATION OF THE POWER  
C      ABSORPTION (PA) AND THE WAVE ENERGY (W)  
C      GROWTH RATE (WI) WAS OBTAINED BY COMPUTING THE ENERGY BALANCE  
      FUNCTION P(O,K,N1,R1,ITER,TT,POL)  
      IMPLICIT COMPLEX*16(A-H,O-Z)  
      COMPLEX*16 KK,MM,TD,NU,KD,KDM,NUOD,NUODM,KDH,KDMH,KDA,KKP  
      COMPLEX O,E,TC,OD,ODM,CMLPX  
      REAL*8 K,KX,KZ,ATHET,DCOS,DSIN,PR,DSQRT,T1,KOD,KODM  
      REAL KB,MASS,L,TPL,TPP,VS,P,T2,OM,EPS,PI,SQRT,REAL,ABS,THET,  
      /D,RB,AIMAG,OMC,PIC  
      REAL SIN,COS  
      INTEGER R1,TT,POL  
      DIMENSION TPL(5),TPP(5),VS(5),L(5),KK(3,3),MM(3,3,5),KD(3,3),  
      /KDM(3,3),KDH(3,3),KDMH(3,3),KDA(3,3),KKP(3,3)
```

```
COMMON/XXX/OM(5),MASS(5),EPS(5),PI(5),KB,OMC,PI C
COMMON/XXZ/E,TPL,TPP,VS,THET,D
CONJG(X)=DCONJG(X)
NITER=ITER
T1=3.14159265D0
PR=DSQRT(T1)
5 CALL MATRIX(0,K,N1,R1,MM,KK)
CALL KITER(KK,0,THET,POL,K,NU)
NITER=NITER-1
IF(NITER.GE.1) GO TO 5
ATHET=THET
KX=K*DSIN(ATHET)
KZ=K*DCOS(ATHET)
C CALCULATION OF THE RATIOS EY/EX AND EZ/EX IN TERMS OF
C THE COMPONENTS OF THE REFRACTIVE INDEX AND DIELECTRIC
C TENSOR
A=(NU*DSIN(ATHET)*DCOS(ATHET)+KK(1,3))*KK(2,1)-KK(2,3)*
/(-NU*DCOS(ATHET)**2+KK(1,1))
A=A/(KK(2,3)*KK(1,2)-(NU*DSIN(ATHET)*DCOS(ATHET)+KK(1,3))*
/(-NU+KK(2,2)))
C=KK(1,2)*KK(2,1)-(-NU+KK(2,2))*(-NU*DCOS(ATHET)**2+KK(1,1))
C=C/((-NU+KK(2,2))*(NU*DSIN(ATHET)*DCOS(ATHET)+KK(1,3))-
/KK(1,2)*KK(2,3))
S1=A-(A*CONJG(A))/A
S2=(C*CONJG(C))/C+C
S3=(A*CONJG(A))*C/A-A*(C*CONJG(C))/C
C CALCULATION OF THE POWER ABSORPTION (PA) BY CHARGED PARTICLES
PA=0.
TD=E
PCA=A*CONJG(A)
PCC=C*CONJG(C)
DO 50 I=1,5
50 PA=PA+PI(1)*EPS(1)/(16.DO*T1*OM(1))*TD*CONJG(TD)*((MM(1,1,1)
/+CONJG(MM(1,1,1)))+PCA*(MM(2,2,1)+CONJG(MM(2,2,1)))+PCC*
/(MM(3,3,1)+CONJG(MM(3,3,1)))+S1*(MM(1,2,1)-CONJG(MM(1,2,1)))
/+S2*(MM(1,3,1)+CONJG(MM(1,3,1)))+S3*(MM(2,3,1)-CONJG(
/MM(2,3,1))))
TC=PA
P=REAL(TC)
OD=REAL(O)+D
ODM=REAL(O)-D
CALL KITER(KK,OD,THET,POL,KOD,NUOD)
CALL MATRIX(OD,KOD,N1,R1,MM,KD)
CALL KITER(KK,ODM,THET,POL,KODM,NUODM)
CALL MATRIX(ODM,KODM,N1,R1,MM,KDM)
C CALCULATION OF THE DERIVATIVE IN THE EQUATION OF WAVE
C ENERGY BY USING NUMERICAL ANALYSIS METHOD
DO 55 I=1,3
DO 55 J=1,3
```

```

KDH(1,J)=(KD(1,J)+CONJG(KD(J,1)))/2.
55  KDMH(1,J)=(KDM(1,J)+CONJG(KDM(J,1)))/2.
    DO 60 I=1,3
    DO 60 J=1,3
60  KKP(1,J)=(OD*KDH(1,J)-ODM*KDMH(1,J))/(2.*D)
C   CALCULATION OF THE WAVE ENERGY (W) AND THE GROWTH RATE
    Y=8.987554E20/0**2
    W=TD*CONJG(TD)/(16.DO*T1)*((Y*KZ**2+KKP(1,1))+PCA*(Y*(KX**
/2+KZ**2)+KKP(2,2))+PCC*(Y*KX**2 KKP(3,3))+A*KKP(1,2)
/CONJG(A)*KKP(2,1)+C*CONJG(A)*KKP(2,3)+A*CONJG(C)*KKP(3,2)
/+C*(KKP(1,3)-Y*KX*KZ)+CONJG(C)*(KKP(3,1)-Y*KX*KZ))
    RB=-PA/(2.*W)
    O=REAL(O)+CMPLX(O.,RB)
    RETURN
    END
```

```

C   SUBPROGRAM TO COMPUTE THE MODIFIED BESSEL FUNCTION OF THE
C   FIRST KIND (BES) AND ITS DERIVATIVE (BESP).
SUBROUTINE B(L,BES,BESP,N1,R1)
REAL L
INTEGER R1
DIMENSION L(5),BES(9,5),BESP(9,5),A(4,5,2)
IQ=2*N1+1
IP=N1+2
DO 5 I=1,5
A(1,1,1)=1
5  A(1,1,2)=1
DO 10 I=1,5
DO 10 K=2,R1
A(K,1,1)=A(K-1,1,1)*(L(I)/2.)**2.*((K-1*(K-1)))
10 A(K,1,2)=A(K,1,1)*2*(K-1)/L(I)
DO 20 I=1,5
DO 20 J=1,IQ
BES(J,1)=0.
20 BESP(J,1)=0
DO 30 I=1,5
BESP(N1+1,1)=-1.
DO 30 K=1,R1
BES(N1+1,1)=BES(N1+1,1)+A(K,1,1)
BESP(N1+1,1)=BESP(N1+1,1)+A(K,1,2)
DO 30 J=IP,IQ
A(K,1,1)=A(K,1,1)*(L(I)/2.)/(K+J-N1-2)
A(K,1,2)=((J-N1-3)+2.*K)*A(K,1,1)/L(I)
BES(J,1)=BES(J,1)+A(K,1,1)
30 BESP(J,1)=BESP(J,1)+A(K,1,2)
DO 40 I=1,5
DO 40 J=1,N1
BESP(J,1)=BESP(2*N1-J+2,1)
40 BES(J,1)=BES(2*N1-J+2,1)
RETURN
END
```

```
C SUBPROGRAM TO COMPUTE THE VALUE OF THE WAVE VECTOR K BY
C USING THE DISPERSION RELATION FROM THE WARM PLASMA
SUBROUTINE KITER(KK,O,THET,POL,K,NU)
COMPLEX*16 KK,NU,A,B,C,CDSQRT,DCONJG,AO,N
COMPLEX O,CSQRT,CONJG
REAL*8 K,U,V,ATHET,DSIN,DCOS
INTEGER POL
DIMENSION KK(3,3)
C THE VALUE OF THE REFRACTIVE INDEX (N) IS OBTAINED BY
C SOLVING THE DISPERSION RELATION (WARM PLASMA)
C  $A*N^{**4}-B*N^{**2}+C=0$ 
A0=0
ATHET=THET
U=DSIN(ATHET)
V=DCOS(ATHET)
A=KK(1,1)*U**4+U**3*V*(KK(3,1)+KK(1,3))+U**2*V**2*(KK(1,1)
/+KK(3,3))+U*V**3*(KK(3,1)+KK(1,3))+V**4*KK(3,3)
B=U**2*(KK(2,1)*KK(1,2)+KK(3,1)*KK(1,3)-KK(1,1)*KK(2,2)-
/KK(1,1)*KK(3,3))+V**2*(KK(3,2)*KK(2,3)+KK(3,1)+KK(1,3)-
/KK(2,2)*KK(3,3)-KK(1,1)*KK(3,3))+U*V*(KK(2,1)*KK(3,2)
/+KK(1,2)*KK(2,3)-KK(3,1)*KK(2,2)-KK(2,2)*KK(1,3))
B=-B
C=KK(1,1)*KK(2,2)*KK(3,3)-KK(1,1)*KK(3,2)*KK(2,3)+KK(2,1)
/*KK(3,2)*KK(1,3)-KK(2,1)*KK(1,2)*KK(3,3)+KK(3,1)*KK(1,2)
/*KK(2,3)-KK(1,3)*KK(3,1)*KK(2,2)
NU=(B+POL*CDSQRT(B**2-4.*A*C))/(2.*A)
N=CDSQRT(NU)
C THE WAVE VECTOR K IS COMPUTED BY USING THE RELATION
C  $N=(C/W)*K$ 
K=CDSQRT(N*DCONJG(N))*CDSQRT(AO*DCONJG(AO))/2.997925E10
RETURN
END

C SUBPROGRAM TO COMPUTE THE VALUE OF THE WAVE VECTOR K BY
C USING THE DISPERSION RELATION FROM THE COLD PLASMA
SUBROUTINE KINIT(PI,OM,EPS,O,THET,POL,K,NU)
COMPLEX O,R,L,P,S,D,B,A,F,N,DSQRT,CONJG,NU
REAL*8 K
INTEGER POL
DIMENSION PI(5),OM(5),EPS(5)
COMMON/XINIT/D,S,P
C THE VALUE OF THE REFRACTIVE INDEX (N) IS OBTAINED BY
C SOLVING THE DISPERSION RELATION (COLD PLASMA APPROXIMATION)
C  $A*N^{**4}-B*N^{**2}+C=0$ 
R=(1.,0.)
L=(1.,0.)
P=(1.,0.)
```

```
DO 10 I=1,5
T=PI(1)/O**2
R=R-T*(O/O+EPS(1)*OM(1))
L=L-T*(O/O-EPS(1)*OM(1))
10 P=P-T
S=(R+L)/2.
D=(R-L)/2.
B=R*L*SIN(THET)**2+P*S*(1.+COS(THET)**2)
A=S*SIN(THET)**2+P*COS(THET)**2
F=4.*(P*D*COS(THET))**2
N=P*S
F=((R*L-N)+SIN(THET)**2)**2+F
F=CSQRT(F)
N=(B+POL*F)/(2.*A)
NU=N
N=CSQRT(N)
C THE WAVE VECTOR K IS COMPUTED BY USING THE RELATION
C N=(C/W)*K
K=CSQRT(N*CONJG(N))*CSQRT(O*CONJG(O))/2.997925E10
N=N*N
RETURN
END

C SUBPROGRAM TO COMPUTE THE COMPONENTS OF THE MOBILITY
C TENSOR M AND THE COMPONENTS OF THE DIELECTRIC TENSOR
SUBROUTINE MATRIX(O,K,N1,R1,MM,KK)
IMPLICIT COMPLEX*16(A-H,O-Z)
COMPLEX*16 KK,MM,NPHI(9,5),NPSI(9,5)
COMPLEX O,U,TC,E
REAL*8 CDABS,K,KX,KZ,ATHET,DCOS,DSIN,Q,TT,SDQRT,PR,AM,AK
REAL KB,MASS,L,TPL,TPP,VS,T2,OM,EPS,PI,BES,BESP,EC,ALTEST,
/SQRT,REAL,CABS,AIMAG,EXP,THET,SIN,COS,D,T1,OMC,PIC
INTEGER R1
DIMENSION TPL(5),TPP(5),BES(9,5),BESP(9,5),Q(5),VS(5),L(5),
/EC(5),S(9,5),FO(9,5),MM(3,3,5),AL(9,5),THETA(9,5),PHI(9,5),
/PSI(9,5),KK(3,3)
COMMON/XXX/OM(5),MASS(5),EPS(5),PI(5),KB,OMC,PIC
COMMON/XXZ/E,TPL,TPP,VS,THET,D
CEXP(X)=CDEXP(X)
CABS(X)=CDABS(X)
IQ=2*N+1
TT=3.14159265D0
PR=DSQRT(TT)
ATHET=THET
C CALCULATION OF THE CONSTANT Q AND LANDA AS USED IN CHAPTER 2
KX=K*DSIN(ATHET)
KZ=K*DCOS(ATHET)
DO 10 I=1,5
AM=MASS(1)
AK=KB
Q(1)=DSQRT(AM/(2.DO*AK*TPL(1)))
L(1)=KX**2*KB*TPP(1)/(OM(1)**2*MASS(1))
```

```
IF(L(1).LE.50.) EC(1)=EXP(L(1))
IF(L(1).GT.50.) EC(1)=EXP(50.)
C CALCULATION OF THE CONSTANT FO
DO 10 J=1,IQ
N=J-N1-1
S1=0+N*OM(1)
S2=KZ*VS(1)
AL(J,1)=(S1-S2)*Q(1)/KZ
TC=AL(J,1)
T1=REAL(TC)
T2=AIMAG(TC)
ALTEST=CABS(AL(J,1))
IF(ALTEST.LE.0.3) S(J,1)=AL(J,1)-2./3.*(AL(J,1)**3)
IF(ALTEST.GT.3.0) S(J,1)=1./(2.*AL(J,1))+1./(4.*AL(J,1)**3)
IF(ALTEST.GT.0.3.AND.ALTEST.LE.3.0) S(J,1)=CEXP(-AL(J,1)**2
/)*(U(T1,(1.,0.),),15)+U(T2,(0.,1.),T1,15))
FO(J,1)=0.
IF(ALTEST.LT.7.) FO(J,1)=PR/CEXP(AL(J,1)**2)
FO(J,1)=FO(J,1)+(0.DO,2.DO)*S(J,1)
CALL ANGLE(THETA(J,1),PHI(J,1),PSI(J,1),NPHI(J,1),NPSI(J,1),
/FO(J,1),0,Q,KZ,N,1)
10 CONTINUE
CALL B(L,BES,BESP,N1,R1)
C CALCULATION OF THE COMPONENTS OF THE MOBILITY TENSOR
DO 20 I=1,3
DO 20 J=1,3
KK(I,J)=0
DO 20 M=1,5
20 MM(I,J,M)=0
KK(1,1)=1
KK(2,2)=1
KK(3,3)=1
DO 30 I=1,5
W=-KB*TPP(I)/(EC(1)*MASS(I)*KZ)
DO 30 J=1,IQ
N=J-N1-1
MM(1,1,1)=MM(1,1,1)+W*OM(1)*EPS(1)*N*N*BES(J,1)*THETA(J,1)/L(1)
MM(2,2,1)=MM(2,2,1)+W*OM(1)*EPS(1)*THETA(J,1)*(N*N*BES(J,1)/
/L(1)+2.DO*L(1)*BES(J,1)-2.DO*L(1)*BESP(J,1))
MM(1,2,1)=MM(1,2,1)+W*OM(1)*(0.DO,1.DO)*N*THETA(J,1))*
/BES(J,1)-BESP(J,1))
MM(1,3,1)=MM(1,3,1)+W*EPS(1)*N*KX*BES(J,1)/L(1)*(N*PHI(J,
/I)-PSI(J,1))
MM(2,3,1)=MM(2,3,1)-W*(0.DO,1.DO)*KX*(BES(J,1)-BESP(J,1))*
/(N*PHI(J,1)-PSI(J,1))
MM(3,3,1)=MM(3,3,1)+OM(1)*EPS(1)/(EC(1)*KZ)*BES(J,1)*(N*
/NPHI(J,1)-NPSI(J,1))
MM(3,1,1)=MM(1,3,1)
MM(3,2,1)=-MM(2,3,1)
30 MM(2,1,1)=-MM(1,2,1)
```

```
C      CALCULATION OF THE COMPONENTS OF THE DIELECTRIC TENSOR
DO 40 I=1,5
W=(0.,1.)*EPS(I)*PI(I)/(0*OM(I))
DO 40 M=1,3
DO 40 N=1,3
40    KK(M,N)=KK(M,N)+W*MM(M,N,I)
      RETURN
      END

C      SUBPROGRAM TO CHECK THE IMAGINARY PART OF THE WAVE FREQUENCY
SUBROUTINE Q(X,K,PP,N1,R1,ITER,TOTIT,POL)
INTEGER R1,POL,TOTIT,TI,TT,SWITCH,TL
REAL*8 K
COMPLEX E,X
DIMENSION TPL(5),TPP(5),VS(5)
COMMON/XXX/OM(5),MASS(5),EPS(5),PI(5),KB,OMC,PIC
COMMON/XXZ/E,TPL,TPP,VS,THET,D
SWITCH=20
TL=TOTIT-1
TT=TOTIT
TI=ITER
10    PP=P(X,K,N1,R1,TI,TT,POL)
      TT=TT-1
      TI=1
      IF(TT.EQ.TL) GO TO 30
      IF(PL*PP.GE.0.) GO TO 30
      IF(SWITCH.LE.1) GO TO 40
      SWITCH=SWITCH-1
30    TT=TL
      PL=PP
      IF(TT.GE.1) GO TO 10
      RETURN
40    WRITE(6,50) X
50    FORMAT(15X,'AT OMEGA= ',E11.4,2X,E11.4)
      RETURN
      END

C      SUBPROGRAM TO COMPUTE FUNCTIONS THETA,PHI,PSI,NPHI,NPSI
C      WHICH ARE THE ARGUMENTS OF THE MOBILITY
SUBROUTINE ANGLE(THETA,PHI,PSI,NPHI,NPSI,FO,O,Q,KZ,N,I)
IMPLICIT COMPLEX*16(A-H,O-Z)
COMPLEX*16 NPHI,NPSI
COMPLEX O,E
REAL*8 KZ,Q
REAL TPL,TPP,VS,THET,D,OM,MASS,EPS,PI,KB,OMC,PIC
DIMENSION TPL(5),TPP(5),Q(5),VS(5)
COMMON/XXZ/E,TPL,TPP,VS,THET,D
COMMON/XXX/OM(5),MASS(5),EPS(5),PI(5),KB,OMC,PIC
```

```
C      CALCULATION OF THE FUNCTIONS THETA, PHI, PSI, NPFI AND NPSI
      THETA=2.DO*Q(I)*Q(I)/(O*TPP(I))*((O.DO,1.DO)*KZ*(TPP(I)-
      /TPL(I))-Q(I)*FO*(O-KZ*VS(I)+N*OM(I))*TPP(I)-N*OM(I)*
      /TPL(I)))
      PHI=2.DO*OM(I)*Q(I)*Q(I)/(KZ*O*TPP(I))*((O.DO,1.DO)*KZ*
      /TPL(I)-TPP(I))+Q(I)*FO*(O+N*OM(I))*(TPP(I)-TPL(I))-KZ*
      /VS(I)*TPP(I)))
      NPFI=2.DO*OM(I)*Q(I)*Q(I)/(KZ**2*O*TPP(I))*((O.DO,1.DO)*
      /KZ*((O+N*OM(I))*TPL(I)-TPP(I))+KZ*VS(I)*TPL(I))+Q(I)*FO*
      /(O+N*OM(I))*((O+N*OM(I))*(TPP(I)-TPL(I))-KZ*VS(I)*TPP(I)))
      PSI=2.DO*Q(I)*Q(I)/KZ*((O.DO,1.DO)*KZ-Q(I)*FO*(O-KZ*VS(I)
      /+N*OM(I)))
      NPSI=2.DO*Q(I)/KZ**2*(O+N*OM(I))*((O.DO,1.DO)*KZ-
      /Q(I)*FO*(O-KZ*VS(I)+N*OM(I)))
      RETURN
      END

C      FUNCTIONAL SUBPROGRAM TO COMPUTE THE INTEGRAL WHICH IS USED
C      TO EVALUATE THE IMAGINARY PART OF THE CONSTANT FO
      COMPLEX FUNCTION U(A,B,C,J)
      COMPLEX B,D,CEXP
      D=B*A/J
      U=0.
      DO 10 I=1,J
10     U=U+CEXP(((2.*I-1)/2.*D-C)**2)
      U=U*D
      RETURN
      END

C      SUBPROGRAM TO COMPUTE THE LHR FREQUENCY UNDER THE CASE
C      THAT S=0
      SUBROUTINE F(PI,OM,OLHR)
      DIMENSION PI(5),OM(5)
C      CALCULATION OF THE LOWER HYBRID RESONANCE FREQUENCY IN
C      RAD/SEC.
      PSUM=0.
      DO 10 I=3,5
10     PSUM=PSUM+PI(I)
      OLHR=(1./PSUM)*(1.+PI(2)/OM(2)**2)
      OLHR=SQRT(1./OLHR)
      RETURN
      END
```

REFERENCES

- Akasofu, S. and Chapman, S. 1972. *Solar-Terrestrial Physics*. Oxford University Press, London.
- Albert, R.D. 1967A. Nearly Monoenergetic Electron Fluxes Detected during a Visible Aurora. *Phys. Rev. Letters*, 18, 369.
- Albert, R.D. 1967B. Energy and Flux Variations of nearly Monoenergetic Auroral Electrons. *J. Geophys. Res.*, 72, 5811.
- Barkhausen, H. 1919. Zwei mit Hilfe der neuen Verstärker eneddeckte Erscheinungen. *Physik. Z.*, 20, 401.
- Barkhausen, H. 1930. Whistling tones from the earth. *Proc. IRE*, 18, 1155.
- Barrington, R.E. and Belrose, J.S. 1963. Preliminary results from the very low frequency receiver aboard Canada's Alouette satellite. *Nature*, 198, 651.
- Barrington, R.E., Hartz, T.R. and Harvey, R.W. 1971. Diurnal distribution of ELF, VLF and LF noise at high latitude as observed by Alouette 2. *J. Geophys. Res.*, 76, 5278.
- Breig, E.L. and Hoffman, J.H. 1975. Variations in Ion Composition at Middle and Low Latitudes from ISIS 2 Satellite. *J. Geophys. Res.*, 80, 2207.
- Brice, N.M. and Smith, R.L. 1964. A Very Low Frequency Plasma Resonance. *Nature*, 203, 926.
- Brice, N.M. and Smith, R.L. 1965. Lower Hybrid Resonance Emissions. *J. Geophys. Res.*, 70, 71.
- Budko, N.I. 1969. Excitation by Whistlers of Lower Hybrid Resonance in the Vicinity of a Body Moving in a Plasma. *Geomag. and Aeronomy*, 9, 350.
- Burtis, W.J. 1973. Electron concentrations calculated from the LHR noise band observed by OGO 3. *J. Geophys. Res.*, 78, 5515.
- Cloutier, P.A., Anderson, H.R., Park, R.J., Vondark, R.R., Spiger, R.J. and Sandel, B.R. 1970. Detection of geomagnetically aligned currents associated with an auroral arc. *J. Geophys. Res.*, 75, 2595.
- Dowden, R.L. 1962. Theory of generation of exospheric very low frequency noise (hiss). *J. Geophys. Res.*, 67, 2223.

- Eckersley, T.L. 1925. Note on musical atmospheric disturbances. Phil. Mag., 49, 1250.
- Eckersley, T.L. 1926. Electrical constitution of the upper atmosphere. Nature, 117, 821.
- Eckersley, T.L. 1928. Radio Echoes and Magnetic Storms. Nature, 122, 768.
- Ellis, G.R.A. 1959. Low frequency electromagnetic radiation associated with magnetic disturbances. Planet. Space Sci., 1, 253.
- Gallet, R.M. and Helliwell, R.A. 1959. Origin of very low frequency emissions. J. Res. Nat. Bur. Stand., 63D, 21.
- Gear, C.W. 1973. Introduction to Computer Science. Science Research Associates Inc., Chicago.
- Gendrin, R. 1975. Waves and wave-particle interactions in the magnetosphere: A Review. Space Sci. Review, 18, 145.
- Gross, S.H. 1970. VLF Duct Associated with the Lower Hybrid Resonance Frequency in a Multi-ion Upper Ionosphere. J. Geophys. Res., 75, 4235.
- Gross, S.H. and Larocca, N. 1972. Phenomenological Study of LHR Hiss. J. Geophys. Res., 77, 1146.
- Gross, S.H. 1972. Collisional Losses in a Very-Low-Frequency Duct Associated with the Lower Hybrid Resonance Frequency. J. Geophys. Res., 77, 3589.
- Gurnett, D.A. 1966. A satellite study of VLF hiss. J. Geophys. Res., 71, 5599.
- Gurnett, D.A. 1968. Observations of VLF hiss at very low L values. J. Geophys. Res., 73, 1096.
- Gurnett, D.A. and Mosier, S.R. 1969. VLF electric and magnetic fields observed in the auroral zone with the Javelin 8.46 sounding rocket. J. Geophys. Res., 74, 3979.
- Gurnett, D.A., Pfeiffer, G.W., Anderson, R.R., Mosier, S.R. and Cauffman, D.P. 1969. Initial observations of VLF electric and magnetic fields with Injun 5 satellite. J. Geophys. Res., 74, 4631.
- Gurnett, D.A. and Frank, L.A. 1972. VLF hiss and related plasma observations in the polar magnetosphere. J. Geophys. Res., 77, 172.

- Guthart, H., Crystal, T.L., Ficklin, B.P., Blair, W.E. and Yung, T.J. 1968. Proton gyrofrequency band emissions observed aboard OGO 2. *J. Geophys. Res.*, 73, 3592.
- Harris, E.G. 1961. Plasma Instabilities Associated with Anisotropic Velocity Distributions. *J. Nucl. Energy* C2, 138.
- Helliwell, R.A. 1956. Low frequency propagation studies: Part I. Whistlers and related phenomena Final Rept. Stanford Electronics Labs., Stanford Univ., Stanford, Calif., 19.
- Helliwell, R.A. 1965. *Whistlers and Related Ionospheric Phenomena*. Stanford University Press, Stanford, California.
- Hoffman, J.H., Dodson, W.H., Lippincott, C.R. and Hammack, H.D. 1974. Initial ion composition results from the ISIS 2 satellite. *J. Geophys. Res.*, 79, 4246.
- Horita, R.E. and Watanabe, T. 1969. Electrostatic waves in the ionosphere excited around the lower hybrid resonance frequency. *Planet. Space Sci.*, 17, 61.
- Horita, R.E. 1972. Wave-particle interaction around the lower hybrid resonance. *Planet. Space Sci.*, 20, 409.
- Horita, R.E. 1974. Proton cyclotron frequency phenomena in the topside ionosphere. *Planet. Space Sci.*, 22, 793.
- Horita, R.E. and Friesen, L. 1975. Proton and helium gyrofrequency phenomena observed on ISIS 2 VLF spectrograms. *J. Atmos. Terr. Phys.*, 37, 1497.
- Horita, R.E., Friesen, L. and Chan, A.W.Y. 1976. Ion Gyrofrequency Phenomena observed on Whistlers, Auroral Hiss and ELF Hiss. *J. Atmos. Terr. Phys.* In press.
- James, H.G. 1973. Whistler-mode hiss at low and medium frequencies in the dayside-cusp ionosphere. *J. Geophys. Res.*, 78, 4578.
- James, H.G. 1976. VLF Saucers. *J. Geophys. Res.*, 81, 501.
- Jørgensen, T.S. 1968. Interpretation of auroral hiss measured on OGO 2 and at Byrd station in terms of Incoherent Cerenkov Radiation. *J. Geophys. Res.*, 73, 1055.
- Kimura, I. 1967. On Observations and Theories of the VLF Emissions. *Planet. Space Sci.* 15, 1427.
- Klumper, D.M. 1975. Evidence for Ion Acceleration by VLF Waves above the Auroral Ionosphere. *Abstract. Physics in Canada* 31(3), 53.

- Laaspere, T., Morgan, M.G. and Johnson, W.C. 1969. Observations of Lower Hybrid Resonance phenomena on OGO 2 spacecraft. *J. Geophys. Res.*, 74, 141.
- Laaspere, T. and Taylor Jr., H.A. 1970. Comparison of certain VLF noise phenomenon with the Lower Hybrid Resonance Frequency calculated from simultaneous ion composition measurements. *J. Geophys. Res.*, 75, 97.
- Laaspere, T., Johnson, W.C. and Semperebon, L.C. 1971. Observations of auroral hiss, LHR hiss, and other phenomena in the frequency range 20 Hz to 540 kHz on OGO 6. *J. Geophys. Res.*, 76, 4477.
- ✓ Liemohn, H.B. 1965. Radiation from electrons in magneto-plasma. *Radio Sci.*, 69D, 741.
- Lim, T.L. and Laaspere, T. 1972. An evaluation of Cerenkov radiation from auroral electrons with energies down to 100 eV. *J. Geophys. Res.*, 77, 4145.
- MacArthur, J.W. 1959. Theory of the very low frequency radio emissions from the Earth's exosphere. *Phys. Rev. Lett.*, 2, 491.
- Mansfield, V.N. 1967. Radiation from a charged particle spiraling in a cold magnetoplasma. *Astrophys. J.*, 147, 672.
- McEwen, D.J. and Barrington, R.E. 1967. Some characteristics of the lower hybrid resonance noise bands observed by Alouette 1 satellite. *Can. J. Phys.*, 45, 13.
- McKenzie, J.F. 1963. Cerenkov Radiation in a magneto-ionic medium (with application to the generation of low frequency electromagnetic radiation in the Exosphere by the passage of charged Corpuscular streams). *Phi. Trans. Roy. Soc., London*, A255, 585.
- McKenzie, J.F. 1967. Radiation losses from a test particle in a plasma. *Phys. Fluids*, 10, 2680.
- Michkofsky, R.N. 1974. Whistler-triggered lower hybrid resonance noise in irregularities of the ionosphere. Ph.D. Thesis. University of British Columbia.
- Mosier, S.R. and Gurnett, D.A. 1969. Ionospheric observation of VLF electrostatic noise related to harmonics of the proton gyro-frequency. *Nature*, 223, 605.
- Muldrew, D.B. 1970. Preliminary results of ISIS 1 concerning electron density variations, ionospheric resonances, and Cerenkov radiation. *Space Res.*, 10, 786.
- Murcay, W.B. and Pope, J.H. 1960. Doppler-shifted cyclotron frequency radiation from protons in the exosphere. *Phys. Rev. Lett.*, 4, 5.

- Oya, H. 1971. Verification of Theory on Weak Turbulence Relating to the Sequence of Diffuse Plasma Resonance in Space. *Phys. Fluids*, 14, 2487.
- Palmer, F.H. and Barrington, R.E. 1973. Excitation of ion Resonances by the ISIS 2 HF Transmitter. *J. Geophys. Res.*, 78, 8167.
- Paymar, E.M. 1972. Banded Whistlers Observed on OGO 4. Stanford University Tech. Rept. No. 3439-1.
- Preece, W.H. 1894. Earth Currents. *Nature*, 49, 554.
- Rao, M., Lalmani, Somayajulu, V.V. and Tantry, B.A.P. 1973. Incoherent Cerenkov radiation and its amplification via the Landau Instability. *Planet. Space Sci.*, 21, 1076.
- Rycroft, M.J. 1972. VLF emissions in the magnetosphere. *Radio Sci.*, 7, 811.
- Scarf, F.L., Fredricks, R.W., Smith, E.J. and Frandsen, A.M.A. 1972A. OGO 5 observations of LHR noise, emissions, and whistlers near the plasmopause at several earth radii during a large magnetic storm. *J. Geophys. Res.*, 77, 1776.
- Scarf, F.L., Fredricks, R.W. and Green, I.M. 1972B. Plasma waves in the Dayside Polar Cusp 1 Magnetospheric Observation. *J. Geophys. Res.*, 77, 2274.
- Shaw, R.R. and Gurnett, D.A. 1971. Whistlers with harmonic bands caused by multiple stroke lightning. *J. Geophys. Res.*, 76, 1851.
- Smith, R.L., Kimura, I., Vigneron, J. and Katsufrahis, J. 1966. Lower Hybrid Resonance Noise and a New Ionospheric Duct. *J. Geophys. Res.*, 71, 1925.
- Stéfant, R.J. 1970. Nonpotential ion harmonic waves. *J. Geophys. Res.*, 75, 7182.
- Stix, T.H. 1962. *The Theory of Plasma Waves*. McGraw-Hill, New York.
- Storey, L.R.O. 1957B. A method for interpreting the dispersion curves of whistlers. *Can. J. Phys.* 35, 1107.
- Størmer, C. 1928. Short wave echoes and the aurora borealis. *Nature*, 122, 681.
- Swift, D.W. and Kan, J.R. 1975. A Theory of Auroral Hiss and Implications on Origin of Auroral Electrons. *J. Geophys. Res.*, 80, 985.

- Taylor, W.W.L. and Shawhan, S.D. 1974. A Test of Incoherent Cerenkov Radiation for VLF Hiss and Other Magnetospheric Emissions. J. Geophys. Res., 79, 105.
- Trulsen, J. and Fejer, J.A. 1970. Radiation from a charged particle in a magnetoplasma. J. Plasma Phys., 4, 825.
- Ungstrup, E. 1975. Narrow band VLF electrostatic signals generated in the auroral ionosphere by the high-frequency two-stream instability. J. Geophys. Res., 80, 4272.
- Willis, J.W. 1975. Temperature effects on Whistler Modes near Gyroresonance. J. Geophys. Res., 80, 1354.

VITA

Surname: CHAN

Given name: ARTHUR WING YEE

Place of Birth: CANTON, CHINA

Date of Birth: AUGUST 8, 1950

Educational Institutions Attended, with Dates of Entering and Leaving:

UNIVERSITY OF VICTORIA

1970 to 1974

Degrees, Diplomas, Etc., Awarded, with Dates and Names of Institutions:

B.Sc. (Honors)

1970-1974

UNIVERSITY OF VICTORIA

M.Sc.

1974-1976

UNIVERSITY OF VICTORIA

Honors and Awards:

UNIVERSITY OF VICTORIA GRADUATE SCHOLARSHIP

1975/76

Publications:

Horita, R.E., Friesen, L. and Chan, A.W.Y. 1976. Ion Gyrofrequency

Phenomena observed on Whistlers, Auroral Hiss and ELF Hiss.

J. Atmos. Terr. Phys. In press.


PARTIAL COPYRIGHT LICENSE

I hereby grant the right to lend my thesis (the title of which is shown below) to users of the University of Victoria Library, and to make single copies only for such users or in response to a request from the library of any other university, or similar institution, on its behalf or for one of its users. I further agree that permission for extensive copying of this thesis for scholarly purpose may be granted by me or a member of the University designated by me. It is understood that copying or publication of this thesis for financial gain shall not be allowed without my written permission.

Title of Thesis:

A Theory for Ion Gyrofrequency Phenomena Observed on VLF Hiss.

Author


Signature

Arthur Wing Yee Chan

June 10, 1976